

ATOMIC-SCALE DYNAMIC PROCESSES
IN THE BRITTLE FRACTURE OF SILICA

By

THOMAS P. SWILER

A DISSERTATION PRESENTED TO THE GRADUATE SCHOOL
OF THE UNIVERSITY OF FLORIDA IN PARTIAL FULFILLMENT
OF THE REQUIREMENTS FOR THE DEGREE OF
DOCTOR OF PHILOSOPHY

UNIVERSITY OF FLORIDA

1994

LD
1780
1994
.S977

UNIVERSITY OF FLORIDA

3 1262 08552 4477

Copyright 1994

by

Thomas P. Swiler

This dissertation is dedicated to my parents, Thomas Russell Swiler and Elaine Palda Swiler, who were always forgiving of my early "fracture experiments." Until we can fulfill our destructive tendencies through simulation, we must rely on forgiveness.

ACKNOWLEDGEMENTS

I would like to acknowledge the support of my advisor, Joseph H. Simmons, throughout this work. He has continually supported a molecular dynamics effort even though it has not been supported by external sources. The opportunity to explore the implications of this simulation work without having to provide specific answers to questions posed by sponsors has made work in this area interesting and instructive.

I would like to thank John J. Mecholsky, Jr. for enlightening me to current research in brittle fracture. His observations and interpretations of fractal fracture surfaces have provided me with the background to make the link between computer simulated fracture and experimentally observed fracture.

I would like to thank Adrian C. Wright for performing comparisons of our pair correlation function data derived from molecular dynamic simulations to his radial distribution data derived from neutron diffraction experiments.

Finally, I would like to thank my family and friends who have provided support for me during the up and downs of writing this dissertation.

TABLE OF CONTENTS

| | |
|---------------------------------------|-------|
| ACKNOWLEDGEMENTS | iv |
| LIST OF TABLES | ix |
| LIST OF FIGURES | x |
| KEY TO SYMBOLS | xv |
| Abstract | xxiii |
| CHAPTERS | |
| 1 INTRODUCTION | 1 |
| What is Fracture | 1 |
| Fracture as a Transformation | 2 |
| Molecular Dynamics | 4 |
| Statement of Problem | 7 |
| 2 BACKGROUND | 8 |
| Brittle Fracture | 9 |
| Characteristics of Brittle Fracture | 9 |
| The Ultimate Strength of Materials | 9 |
| The Effect of Flaws | 11 |
| Regimes of Brittle Fracture | 12 |
| Environmental Effects | 12 |
| Crack Propagation Velocities | 14 |
| Reading the Fracture Surface | 14 |
| Silica | 16 |
| Bonding in Silica | 16 |
| Structure of Silica | 16 |
| Phases of Silica | 18 |
| The Crystal Structure of Cristobalite | 19 |
| The Ring Structure of Silica | 20 |

| | |
|---|----|
| Elastic Properties of Vitreous Silica | 23 |
| The Fracture Strength of Silica | 24 |
| Stress Corrosion of Silica | 25 |
| Molecular Dynamics | 28 |
| Survey of Applications | 28 |
| Survey of Potential Functions | 31 |
| Potentials for Silica | 34 |
| Applications of MD in Models of Silica | 37 |
| Comparisons of Simulated Structure to Experiment | 39 |
| MD Simulations of Fracture | 40 |
| Chaos in Fracture: Determinism and Fractal Surfaces | 43 |
| Investigations of Chaotic Processes | 44 |
| Predictability of Brittle Fracture | 46 |
| Fractal Geometry | 47 |
| Applications of Fractal Geometry to Fracture | 49 |
| The Fractal-like Nature of Fracture Surfaces | 51 |
| Applicability of Fractal Analyses to MD Simulated Systems | 52 |
| | |
| 3 PROCEDURE | 56 |
| | |
| Using Molecular Dynamics to Model Fracture | 56 |
| Potential Functions | 58 |
| The Born-Mayer-Huggins Potential | 60 |
| Truncation or Screening Functions | 61 |
| The Soules Potential Function | 63 |
| The Feuston-Garofalini Potential Function | 65 |
| Simulation Techniques | 68 |
| Integration Algorithms | 68 |
| Verlet algorithm | 68 |
| Fifth-order Gear predictor-corrector algorithm | 69 |
| The Time Step | 69 |
| Limiting Particle Interactions | 70 |
| Application of Periodic Boundary Conditions | 72 |
| Handling Particle Interactions | 74 |
| Observing the System | 76 |
| System thermodynamics | 76 |
| System structure | 77 |
| Force Distributions | 79 |
| Damped Motion Molecular Dynamics | 80 |
| Assigning Initial Velocities | 80 |
| Analytical Techniques | 81 |
| Graphic Representations | 82 |
| Free Volume Sphere Analysis | 82 |
| Ring Statistics | 84 |

| | |
|--|-----|
| Structural Defects | 86 |
| Composition Profiles | 86 |
| Mechanical Properties | 87 |
| Program Details | 87 |
| Overview | 87 |
| The Structure of Computer Code | 88 |
| The Choice of a Programming Language | 92 |
| The Simulation Program | 95 |
| The Graphic Analysis Program | 96 |
| Other Analysis Programs | 97 |
| Experimental Techniques | 97 |
| Initial Conditions | 97 |
| Application of Uniaxial Strain | 99 |
| Application of Shear Strain | 101 |
| Experiments and Analyses | 103 |
| Phases Simulated | 103 |
| Strain Rates Simulated | 103 |
| Comparison of Potential Functions | 103 |
| Thermal Effects | 104 |
| Studies of Determinism | 104 |
| Studies of Nonlinear Viscosity | 105 |
| | |
| 4 RESULTS AND DISCUSSION | 106 |
| | |
| The Models | 106 |
| Static (Structural) Characteristics | 107 |
| Densities and pressure tensors | 107 |
| Low-order pair-correlation functions | 108 |
| High-order pair correlation functions | 112 |
| Discussion of higher order peaks | 113 |
| Bond angle distributions | 116 |
| Comparison of structural distributions to experiment | 117 |
| Ring statistics | 121 |
| Volume distributions | 124 |
| Defects | 125 |
| Dynamic Properties | 126 |
| Melting temperature | 126 |
| Mechanical properties | 129 |
| Review of Models | 131 |
| Fracture by Application of Uniaxial Strain | 132 |
| Overview | 132 |
| Low Cristobalite | 133 |
| Stress-strain curves | 134 |
| Energetics of fracture | 142 |

| | |
|--|-----|
| Fracture surfaces | 149 |
| Vitreous Silica | 154 |
| Stress-strain curves | 154 |
| Energetics of fracture | 160 |
| Structural changes during strain-to-fracture | 164 |
| Viscous Flow | 174 |
| Determinism in Fracture | 179 |
| Reproducibility and Accuracy of Computer Simulations | 179 |
| Variation in Anneal Times | 180 |
| Round-off Errors | 182 |
| "Butterfly Effect" | 183 |
| Sensitivity on Simulation Artifacts | 185 |
| | |
| 5 ANALYSIS | 187 |
| | |
| Models of Silica | 187 |
| Stress and Strain | 190 |
| Structural Changes During Strain-to-Failure | 190 |
| Shear Flow | 193 |
| Initiation of Fracture | 194 |
| Crack Propagation | 198 |
| Simulation of Stochastic Crack Growth | 199 |
| The Completion of Fracture | 202 |
| The Structure of the Fracture Surface | 203 |
| When is a Bond Broken | 203 |
| Surface Reconstruction | 204 |
| Determinism in Fracture | 207 |
| | |
| 6 CONCLUSIONS AND FUTURE WORK | 209 |
| | |
| REFERENCE LIST | 211 |
| | |
| BIOGRAPHICAL SKETCH | 219 |

LIST OF TABLES

Table

| | | |
|-----|---|-----|
| 2-1 | Characteristics of the Phases of Silica | 19 |
| 3-1 | Parameters Used in the Soules Force and Potential Functions | 63 |
| 3-2 | Parameters used in the Feuston-Garofalini Potential Function | 67 |
| 4-1 | Coordination of species in simulations using various potentials and methods of formation as found by the ring statistics program. | 125 |
| 4-2 | Coordination of species in simulations of vitreous silica at 0.2 strain and various strain rates as found by the ring statistics program. | 173 |
| 4-3 | Viscosities of vitreous silica as modeled by the Soules potential at various temperatures and strain rates, in units of 10^{21} Pa·s. | 175 |

LIST OF FIGURES

Figure

| | | |
|------|--|-----|
| 2-1. | Schematic showing crack propagation velocities as a function of stress intensity factor.. | 13 |
| 2-2. | The silica tetrahedron is the basic structural unit of silica structures. a) One silica tetrahedron. b) Two tetrahedra linked by corner sharing. θ is the Si-O-Si bond angle.. | 17 |
| 2-3. | Chemical reaction proposed by Michalske and Freiman for environmentally enhanced Si-O-Si bond rupture. The strained crack tip bond (a) adsorbs a water molecule, (b) is cleaved by dissociative reaction, and (c) is converted to surface silanol groups.. | 26 |
| 3-1. | Plot of the Soules potential function for various interactions. | 64 |
| 3-2. | Plot of the two-body portion of the Feuston-Garofalini potential function for various interactions. | 66 |
| 3-3. | The effect of periodic boundary conditions in a simulated system. Note that the neighborhood of an atom may extend beyond the primary cell. | 71 |
| 3-4. | Schematic showing the application of periodic boundary conditions to a system under shear strain. | 74 |
| 4-1. | Comparison the first peaks of the Si-O pair correlation functions for vitreous silica as modeled by the Soules and the F-G potential functions. | 109 |
| 4-2. | Comparison the first peaks of the O-O pair correlation functions for vitreous silica as modeled by the Soules and the F-G potential functions. | 110 |

| | | |
|-------|--|-----|
| 4-3. | Comparison the first peaks of the Si-Si pair correlation functions for vitreous silica as modeled by the Soules and the F-G potential functions. | 111 |
| 4-4. | Comparison the higher order peaks of the Si-O pair correlation functions for vitreous silica as modeled by the Soules and the F-G potential functions. | 113 |
| 4-5. | Contribution of various pair interactions to the potential energy of vitreous silica as modeled by the Soules potential function. | 114 |
| 4-6. | Contribution of various pair interactions to the potential energy of vitreous silica as modeled by the F-G potential function. | 115 |
| 4-7. | Comparison of O-Si-O bond angle distributions for vitreous silica as modeled by the Soules and the F-G potential functions. | 117 |
| 4-8. | Comparison of Si-O-Si bond angle distributions for vitreous silica as modeled by the Soules and the F-G potential functions. | 118 |
| 4-9. | Comparison of radial distribution functions derived from a neutron diffraction experiment (solid line) and a molecular dynamics simulation using the Soules potential (dashed line). | 119 |
| 4-10. | Comparison of radial distribution functions derived from a neutron diffraction experiment (solid line) and a molecular dynamics simulation using the F-G potential (dashed line). | 120 |
| 4-11. | Comparison of the ring size distributions for vitreous silica as modeled by the Soules and the F-G potential functions and as formed by crystal melt and random position techniques. | 122 |
| 4-12. | Comparison of the free volume sphere size distributions for vitreous silica as modeled by the Soules and the F-G potential functions and as formed by various techniques. | 124 |
| 4-13. | Potential energy as a function of temperature for cristobalite as modeled by the Soules potential. | 127 |
| 4-14. | Potential energy as a function of temperature for cristobalite as modeled by the F-G potential. | 128 |
| 4-15. | Equilibrium elastic stress-strain curves for cristobalite and vitreous silica as modeled by the Soules and the F-G potential functions. | 129 |

| | | |
|-------|---|-----|
| 4-16. | Comparison of stress-strain curves at various strain rates for low cristobalite as modeled by the Soules potential. | 134 |
| 4-17. | Comparison of stress-strain curves at various strain rates for low cristobalite as modeled by the F-G potential. | 135 |
| 4-18. | View down the C-axis of low cristobalite under an intermediate tensile strain applied along the C-axis, as modeled by the Soules potential. In this view and in all following views, oxygen atoms are represented by the larger, lighter balls, and silicon atoms are represented by the smaller, darker balls. | 137 |
| 4-19. | View down the C-axis of low cristobalite under an intermediate tensile strain applied along the C-axis, as modeled by the F-G potential. | 138 |
| 4-20. | View down the C-axis of low cristobalite under a high tensile strain applied along the C-axis, as modeled by the F-G potential. | 139 |
| 4-21. | View down the C-axis of low cristobalite under a high tensile strain applied along the C-axis, as modeled by the Soules potential. | 140 |
| 4-22. | Potential energy as a function of strain for low cristobalite as modeled by the Soules potential function under adiabatic strain at various strain rates. | 144 |
| 4-23. | Kinetic energy as a function of strain for low cristobalite as modeled by the Soules potential function under adiabatic strain at various strain rates. | 145 |
| 4-24. | System temperature as a function of strain for low cristobalite as modeled by the Soules potential function under adiabatic strain at various strain rates. | 146 |
| 4-25. | Schematic showing the flow of energy in a brittle material system during strain-to-failure. | 147 |
| 4-26. | Potential energy as a function of strain for low cristobalite as modeled by the Soules potential function under isothermal strain at various strain rates. | 148 |
| 4-27. | Normal view of a shallow slice of a surface created during the fracture of low cristobalite as modeled by the Soules potential under isothermal conditions at 0.05 ps^{-1} strain rate. The failure of the slice to fill the entire area is a consequence of the roughness of the surface. | 149 |

| | | |
|-------|---|-----|
| 4-28. | Side view of surfaces created during the fracture of low cristobalite as modeled by the Soules potential under isothermal conditions at 0.05 ps ⁻¹ strain rate. | 151 |
| 4-29. | Side view of surfaces created during the fracture of low cristobalite as modeled by the Soules potential under isothermal conditions at 0.5 ps ⁻¹ strain rate. | 151 |
| 4-30. | Relative abundance of oxygen and silicon atoms in slices along the length of the cell perpendicular to the direction of strain. Values plotted are the predominance of oxygen over silicon. | 152 |
| 4-31. | Close-up side view of surface created during the fracture of low cristobalite as modeled by the Soules potential under isothermal conditions at 0.5 ps ⁻¹ strain rate. | 153 |
| 4-32. | Comparison of stress-strain curves at various strain rates for vitreous silica as modeled by the Soules potential. | 155 |
| 4-33. | Comparison of stress-strain curves at various strain rates for vitreous silica as modeled by the F-G potential. | 156 |
| 4-34. | Distribution of forces on the atoms comprising a vitreous silica sample under strain at 0.05 ps ⁻¹ strain rate. Various curves represent different engineering strains. | 158 |
| 4-35. | Distribution of forces on the atoms comprising a vitreous silica sample under strain at 5.0 ps ⁻¹ strain rate. Various curves represent different engineering strains. | 159 |
| 4-36. | Potential energy as a function of strain for vitreous silica as modeled by the Soules potential function under adiabatic strain at various strain rates. | 161 |
| 4-37. | System temperature as a function of strain for vitreous silica as modeled by the Soules potential function under adiabatic strain at various strain rates. | 162 |
| 4-38. | Potential energy as a function of strain for vitreous silica as modeled by the Soules potential function under isothermal strain at various strain rates. | 163 |
| 4-39. | Si-O pair correlations in vitreous silica. Comparisons between unstrained and strained to 0.2 at various strain rates are made. | 165 |

| | | |
|-------|--|-----|
| 4-40. | Si-Si pair correlations in vitreous silica. Comparisons between unstrained and strained to 0.2 at various strain rates are made. | 166 |
| 4-41. | O-Si-O bond angle distributions in vitreous silica. Comparisons between unstrained and strained to 0.2 at various strain rates are made. | 167 |
| 4-42. | Si-O-Si bond angle distributions in vitreous silica. Comparisons between unstrained and strained to 0.2 at various strain rates are made. | 168 |
| 4-43. | Comparison of ring size distributions of vitreous silica strained to 0.2 at different strain rates. | 169 |
| 4-44. | Change in the abundances of rings of various sizes during strain to 0.2 in vitreous silica at various strain rates. | 170 |
| 4-45. | Free volume sphere histogram--the integral of the free volume sphere distribution--for vitreous silica strained to 0.2 strain at various strain rates. | 171 |
| 4-46. | Shear stress as a function of time for a vitreous silica sample as modeled by the Soules potential function at various temperatures. | 176 |
| 4-47. | Shear stress as a function of time for a vitreous silica sample as modeled by the Soules potential function at various strain rates. | 177 |
| 4-48. | Stress-strain curves for nearly identical systems after various anneal times. | 180 |
| 4-49. | Stress-strain curves for nearly identical systems differing by a loss of precision resulting from truncation of system conditions at various times. | 183 |
| 4-50. | Deviations from stress-strain curves resulting from a displacement of one atom immediately before straining. | 184 |
| 4-51. | Deviations from stress-strain curves resulting from a displacement of one atom before an anneal period prior to straining. | 185 |
| 5-1. | Pseudo fracture surface created by simple stochastic crack propagation simulation. | 201 |
| 5-2. | Schematic showing the fracture of a bond in vitreous silica. Series shows unstrained bond, strained bond, and broken bond. | 205 |

KEY TO SYMBOLS

- A 1. A parameter in the Born potential. 2. The cross sectional area covered by a bond. 3. A parameter in one form of the Lennard-Jones potential. 4. A parameter in the two-body portion of the Stillinger-Weber potential.
- A_{1uv} A parameter in the two-body part of the Vessal potential for types u and v .
- A_{uv} 1. A parameter in the Born-Mayer-Huggins interaction potential between atoms of type u and v . 2. A parameter in the two-body part of the Vessal potential for types u and v .
- A_{uvw} A parameter in the three-body part of the Vessal potential corresponding to the interaction between types u , v and w .
- B 1. A parameter in the Born potential. 2. A parameter in one form of the Lennard-Jones potential. 3. A parameter in the two-body portion of the Stillinger-Weber potential. 4. A parameter in a stochastic crack simulation.
- $B(\theta_{ijk})$ An angularly dependent function used in the Vessal potential.
- B_{1uv} A parameter in the two-body part of the Vessal potential for types u and v .
- B_{uvw} The strength of the three-body interaction of types u , v and w in the Vashishta potential.
- C 1. A constant the maximum crack velocity equation. 2. A parameter in a stochastic crack simulation.
- C_{1uv} A parameter in the two-body part of the Vessal potential for types u and v .
- C_{uv} 1. A parameter in the Born-Mayer-Huggins interaction potential between atoms of type u and v . 2. A parameter in the two-body part of the Vessal potential.

| | |
|-----------|--|
| D | 1. Fractal dimension. This is an approximation of the box counting dimension when applied to real materials. 2. A parameter in a stochastic crack simulation. |
| D^* | Fractional part of a fractal dimension. |
| D_{1uv} | A parameter in the two-body part of the Vessal potential for types u and v . |
| D_{uv} | A parameter in the Born-Mayer-Huggins interaction potential between atoms of type u and v . |
| E_{1uv} | A parameter in the two-body part of the Vessal potential for types u and v . |
| E | Young's modulus or elastic modulus. |
| E_K | System kinetic energy. |
| E_p | System potential energy. |
| F | A mathematical set of points. |
| $F(r)$ | Force function of r , based on a potential function of r . |
| F_{1uv} | A parameter in the two-body part of the Vessal potential for types u and v . |
| F_{ij} | The interatomic force vector between atoms i and j . |
| F_{ijk} | The interatomic force vector resulting from the interaction between atoms i , j and k . |
| G | Shear modulus. |
| H_{uv} | The strength of the steric repulsion in the interaction of types u and v in the Vashishta potential. |
| K_{IC} | Fracture toughness, the stress intensity required to cause type I fracture. |
| L | 1. A linear dimension that is smaller than an edge dimension of the molecular dynamics cell, used in the truncation function of the Born-Mayer-Huggins potential based on the Ewald sum. The value of the force cut-off distance is often used. 2. Longitudinal modulus. |

| | |
|-----------------------|--|
| M_j | A material dependent constant in the equation relating the failure stress of a material and the radius at which a transition in the fracture surface occurs, such as mirror to mist, mist to hackle, or mist to crack branching. The subscript j corresponds to the particular transition. |
| N | The number of atoms in a simulation. |
| N_i | The number of atoms of type i . |
| $N_\delta(F)$ | A function that gives the number of boxes of side length δ that cover the set F . |
| P | System pressure. |
| P_{mn} | Pressure tensor in the mn coordinates. |
| P_{1uv} | A parameter in the two-body part of the Vessal potential for types u and v . |
| Q_{1uv} | A parameter in the two-body part of the Vessal potential for types u and v . |
| R_n | A random number evenly distributed between 0 and 1 used in assigning random velocities to atoms. |
| R_{1uv} | A parameter in the two-body part of the Vessal potential for types u and v . |
| R_x | The crystallographic R factor, a figure of merit used in the comparison of pair correlation functions where better fits are represented by lower values. |
| S_{1uv} | A parameter in the two-body part of the Vessal potential for types u and v . |
| T | Temperature of the system. |
| $T(r)$ | The truncation function applied to the force function in the Soules potential. |
| $T_{\text{exp}}(r_i)$ | The experimentally derived pair-correlation function at discrete values of r . |
| $T_{\text{sim}}(r_i)$ | The simulation derived pair-correlation function at discrete values of r . |

| | |
|------------------------------|--|
| V | Volume of the molecular dynamics cell. |
| Z_u | The effective charge of an ion of type u in the Vashishta and Born-Mayer-Huggins potentials. |
| a | 1. A parameter in the Morse potential. 2. A cut-off distance used in the Stillinger-Weber potential. |
| a_0 | 1. The dimension of a unit cell along the crystallographic a direction. 2. A parameter having dimensions of length in the relation between fracture toughness and surface fractal dimension of for a material. |
| a_{ij} | The effect of a defect at location (i,j) in a stochastic crack simulation. |
| b | A parameter in the Born-Mayer-Huggins potential. |
| c | Crack length. |
| c_0 | The dimension of a unit cell along the crystallographic c direction. |
| c_u | An integer indicating how many cell lengths a particle should be translated in the u dimension to bring it back into the primary cell. |
| d_{ij} | The deviation caused by a defect at location (i,j) in a stochastic crack simulation. |
| d_{uij} | The u coordinate difference between atoms i and j . |
| d'_{uij} | The u coordinate difference between atoms i and j after correction for periodic boundary conditions. |
| $\dim_{\mathbb{B}}F$ | The box-counting dimension of set F . |
| $f_2(r)$ | A dimensionless two-body potential, used in the Stillinger-Weber potential. |
| $f_\theta(r_1, r_2, \theta)$ | A dimensionless angularly dependent three-body potential, used in the Stillinger-Weber potential. |
| $\text{gdev}(1)$ | A function that returns a random Gaussian deviate with a variance of 1. |
| i | 1. An index indicating an atom. 2. An index representing a location on a discrete x - y plane in a stochastic crack simulation. |

| | |
|-----------|--|
| j | 1. An index indicating an atom. 2. An index representing a location on a discrete x - y plane in a stochastic crack simulation. |
| k | An index indicating an atom. |
| k_B | Boltzmann's constant. |
| k_{uvw} | A parameter in the three-body part of the Vessal potential corresponding to the three-body spring constant for the interaction between types u , v and w . |
| l | An unspecified constant in the Vashishta potential. |
| m_i | The mass of atom i . |
| m_u | The mass of an atom of type u . |
| m | An index representing a coordinate in space. |
| n | 1. A parameter in the Born potential. 2. An exponent in the truncation function used in the Soules force function. 3. An index representing a coordinate in space. |
| n_u | The number of valence electrons for atom type u , used in the Born-Mayer-Huggins potential. |
| p | A parameter in the two-body portion of the Stillinger-Weber potential. |
| q | A parameter in the two-body portion of the Stillinger-Weber potential. |
| q_u | The charge on atoms of type u . |
| r | Length or distance, often corresponding to an interatomic distance. |
| r_0 | The cutoff distance for the three-body interaction in the Vashishta potential. |
| r_{ds} | The decay length of the r^4 interaction term in the Vashishta potential. |
| r_i | The position vector for atom i . |
| $r_{i,t}$ | The position vector for atom i at time t . |
| r_{ij} | The interatomic distance between atoms i and j . |

| | |
|--------------|---|
| r_j | Radius about the initiating flaw where a transition in the fracture surface occurs, such as mirror to mist, mist to hackle, or mist to crack branching. The subscript j corresponds to the particular transition. |
| r_{\max} | The interaction cutoff distance used in the Soules force function. |
| s_u | The u dimension of the MD cell. |
| u | 1. An index indicating an atom type. 2. An index representing a coordinate in space. |
| v | 1. An index indicating an atom type. 2. An index representing a coordinate in space. |
| v_i | The velocity of atom i . |
| v_c | The maximum crack propagation velocity in a material. |
| w | 1. An index indicating an atom type. 2. An index representing a coordinate in space. |
| x | The x coordinate location on a discrete x - y plane in a stochastic crack simulation. |
| x_{ij} | The x coordinate distance between atoms i and j . |
| x_{ui} | The u Cartesian coordinate of atom i . |
| y | The y coordinate location on a discrete x - y plane in a stochastic crack simulation. |
| y_{ij} | The y coordinate distance between atoms i and j . |
| z_{xy} | The z coordinate of a stochastic crack at coordinates (x,y) . |
| z_{ij} | The z coordinate distance between atoms i and j . |
| Δt | The length of a time step. |
| α_u | The electronic polarizability of an ion of type u in the Vashishta potential. |
| β_{uv} | 1. The Pauling coefficient, used in the Born-Mayer-Huggins potential, for atom types u and v . 2. A parameter used in the screening function for the |

| | |
|---|---|
| | long range interactions in the Feuston-Garofalini potential between atom types u and v . |
| δ | A small length. |
| ϵ | 1. Strain. In this work we use engineering strain. 2. A parameter used in Lennard-Jones and Stillinger-Weber potentials to scale the potential energy. 3. A constant in the truncation term of the Born-Mayer-Huggins potential function based on the Ewald sum, typically between 0.175 and 0.35. |
| γ | 1. Surface energy. 2. A parameter in the three-body portion of the Stillinger-Weber potential. |
| λ | A parameter specifying the strength of the three-body interaction in the Stillinger-Weber potential. |
| λ_{uvw} | A parameter that gives the strength of the three-body interaction for atom types u , v and w in the Feuston-Garofalini potential. |
| η_{uv} | The exponent of the steric repulsion in the interaction of types u and v in the Vashishta potential. |
| ϕ_0 | A parameter in the Morse potential. |
| $\phi_{2uv}(r)$ | Pair interaction potential function of r for atom types u and v . The subscript 2 indicates that this is a two-body interaction potential. If only one atom type is present, the subscripts uv are not written. |
| $\phi_{3uvw}(r_i, r_j, r_k)$ | Three-body interaction potential function of positions r_i , r_j , and r_k for atom types u , v and w . The subscript 3 indicates that this is a three-body interaction potential. If only one atom type is present, the subscripts uvw are not written. |
| $\phi_{\theta uvw}(r_{ij}, r_{jk}, \theta_{ijk})$ | Angularly dependent three-body potential of r_{ij} , r_{jk} , and the included angle, θ_{ijk} for atom types u , v and w . The subscript θ indicates that this is a simple angularly dependent three-body potential. If only one atom type is present, the subscripts uvw are not written. |
| ρ | 1. Density. 2. Hardness parameter in the Born-Mayer-Huggins potential. |
| σ | 1. Stress. 2. A parameter used in Lennard-Jones and Stillinger-Weber potentials to scale the interaction distances. |

| | |
|----------------------|--|
| σ_c | Critical stress required to cause fracture in a sample with surface flaws. |
| σ_f | Failure stress. |
| σ_{th} | Theoretical cohesive strength. |
| σ_u | Radius repulsive parameter for atom type u in the Born-Mayer-Huggins potential. |
| θ_0 | The tetrahedral bond angle, $\cos^{-1}(-1/3)$, in the three-body portion of the Vessal potential. |
| θ_{ijk} | The i - j - k bond angle. |
| $\bar{\theta}_{uvw}$ | The preferred bond angle for the three-body interaction of types u , v and w in the Vashishta potential. |
| τ_{uv} | Shear in the u - v plane: displacement in u dependent on change in v . |
| ν | Poisson's ratio. |

Abstract of Dissertation Presented to the Graduate School
of the University of Florida in Partial Fulfillment of the
Requirements for the Degree of Doctor of Philosophy

ATOMIC-SCALE DYNAMIC PROCESSES
IN THE BRITTLE FRACTURE OF SILICA

By

THOMAS P. SWILER

April 1994

Chairperson: Joseph H. Simmons

Major Department: Materials Science and Engineering

The molecular dynamics (MD) simulation technique was used to study the atomic-scale dynamics processes that may take place in the fracture of brittle materials. Silica was chosen as the host material for this study because it occurs in both crystalline and vitreous phases, it is of great technical interest, and it has been widely simulated using MD.

Two models for silica based on different interatomic potential functions were used and compared. The Soules two-body potential resulted in structures having better densities and closer correspondence to neutron diffraction data than did the Feuston-Garofalini three-body potential, which resulted in fewer topological defects and a cristobalite structure that did not undergo a symmetry transformation under uniaxial strain. Both vitreous silica and cristobalite were modeled.

Fracture experiments were performed by applying uniaxial strain to the various samples at strain rates ranging from 0.05 ps^{-1} to 5.0 ps^{-1} . The fracture behaviors for all samples were dependent on the strain rate. Samples strained at higher strain rates exhibited higher fracture strengths, less localized fracture, and rougher fracture surfaces. Cristobalite samples were stronger than vitreous silica samples.

Both permanent structural variations and thermal vibrations affected the path of fracture through the samples. The fracture path was extremely sensitive to initial conditions, indicating that fracture is a truly chaotic process.

We found that the effects of the strain-rate dependence could be traced to the "flow" of strain throughout the sample during fracture. In a normal fracture process, the local strain-rate at the crack tip may increase as a crack propagates, causing fracture to appear as a high strain-rate process in real material. A fracture mechanism is proposed that may result in a fracture surface containing self-similar features like those observed in the fracture of real brittle materials. A simple stochastic crack growth simulation is performed to show the viability of the proposed mechanism.

CHAPTER 1 INTRODUCTION

What is Fracture

The word fracture originated from the latin word *frangere*, which simply means, to break. In days of antiquity, brittle objects that were whole simply broke into parts if they were not strong enough to support the applied load. Of course, objects still break if they are not strong enough to support the applied load, but we now have the tools to investigate how they break. Fracture is not considered an instantaneous event by which one piece becomes two or more pieces, but a transformation process that can be followed from start to finish. However, as much as fracture has been experienced, the process is not fully understood.

We propose that a complete understanding of fracture can be obtained only if we understand what happens in a material under strain to fracture at the atomic scale. Fracture displays a complexity that cannot be fully modeled using a continuum model for a material body. Griffith¹ and Orowan² proposed criteria for predicting the growth of cracks in brittle materials using strain-energy release and stress-intensity criteria, respectively, in a body that is assumed to be composed of a continuum of material. The formalism put forth by these models is still dominant in fracture mechanics. The stress intensity criterion has been extended to predict slow crack growth of materials in a

corrosive environment by Michalske and Freiman.³ However, although these models predict the growth of cracks in an object under an applied load and the role of cracks in reducing the strength of objects, they cannot predict the complex geometries that the fracture process creates. Thus, we must advance beyond a continuum model and view fracture as a process that occurs in a many-body system, instead of as a process that occurs in a continuum of matter, to understand all the processes that result in the details observed in fracture.

We seek to model fracture on the atomic scale and then attempt to extrapolate the behaviors that we observe to the mesoscopic scale.

Fracture as a Transformation

Fracture is a simple process in some respects, and it is nearly infinitely complex in others.

In terms of fracture, materials fall into two gross categories--brittle and ductile. Brittle materials are those materials that fracture with little deformation before the initiation of fracture. Ductile materials are those that are capable of undergoing significant deformation before fracture occurs. Certain materials may be either brittle or ductile under different conditions.

Within the field of materials science and engineering, the costs associated with both fracture and corrosion to the national economy on a yearly basis are often cited to emphasize the negative aspects of these processes. These are the processes that cause

CHAPTER 1 INTRODUCTION

What is Fracture

The word fracture originated from the latin word *frangere*, which simply means, to break. In days of antiquity, brittle objects that were whole simply broke into parts if they were not strong enough to support the applied load. Of course, objects still break if they are not strong enough to support the applied load, but we now have the tools to investigate how they break. Fracture is not considered an instantaneous event by which one piece becomes two or more pieces, but a transformation process that can be followed from start to finish. However, as much as fracture has been experienced, the process is not fully understood.

We propose that a complete understanding of fracture can be obtained only if we understand what happens in a material under strain to fracture at the atomic scale. Fracture displays a complexity that cannot be fully modeled using a continuum model for a material body. Griffith¹ and Orowan² proposed criteria for predicting the growth of cracks in brittle materials using strain-energy release and stress-intensity criteria, respectively, in a body that is assumed to be composed of a continuum of material. The formalism put forth by these models is still dominant in fracture mechanics. The stress intensity criterion has been extended to predict slow crack growth of materials in a

corrosive environment by Michalske and Freiman.³ However, although these models predict the growth of cracks in an object under an applied load and the role of cracks in reducing the strength of objects, they cannot predict the complex geometries that the fracture process creates. Thus, we must advance beyond a continuum model and view fracture as a process that occurs in a many-body system, instead of as a process that occurs in a continuum of matter, to understand all the processes that result in the details observed in fracture.

We seek to model fracture on the atomic scale and then attempt to extrapolate the behaviors that we observe to the mesoscopic scale.

Fracture as a Transformation

Fracture is a simple process in some respects, and it is nearly infinitely complex in others.

In terms of fracture, materials fall into two gross categories--brittle and ductile. Brittle materials are those materials that fracture with little deformation before the initiation of fracture. Ductile materials are those that are capable of undergoing significant deformation before fracture occurs. Certain materials may be either brittle or ductile under different conditions.

Within the field of materials science and engineering, the costs associated with both fracture and corrosion to the national economy on a yearly basis are often cited to emphasize the negative aspects of these processes. These are the processes that cause

In order to study the dynamics of fracture in brittle materials, we require high-speed investigative techniques on the atomic scale. These techniques do not currently exist. Thus, in order to study the dynamic processes occurring in brittle fracture, we perform simulations to examine the behaviors that we cannot see by normal experimental means.

Molecular Dynamics

Molecular dynamics (MD) is a numeric technique that builds on a knowledge of interatomic potential functions to investigate the behavior of a system of atoms under various conditions. It was first used by Rahman⁴ to investigate the motion of Ar atoms in a liquid, and has since been used in studies ranging from enzymatic reactions to the fracture of materials.

Molecular dynamics can be compared with another commonly used simulation technique, Monte Carlo simulations, by examining the path that the system takes while being simulated. Monte Carlo simulations make random perturbations of a system to find favorable configurations. It is not necessary that the individual perturbations be realistic because only the thermodynamics and structure of the final state are important. In contrast, molecular dynamics simulations allow movement of atoms according to Newton's equations of motion. Thus, the Monte Carlo simulation technique allows the simulation of physically realistic structures, but not physically realistic dynamics. Molecular dynamics, on the other hand, is capable of simulating dynamics, but not necessarily the most optimal structures. In MD, movement to optimal structures may be

the failure of useful objects. As a result, much of the research in the area of fracture has been involved in predicting the strength of materials.

The processes by which the usable strengths of materials in real-world applications are limited are well understood. The strengths of ductile materials are limited by the formation and movement of dislocations that cause permanent deformation at the yield stress. This may cause the parts made from these materials to fail in their purposes, whether the parts have completely fractured or not. The strengths of brittle materials are usually limited by flaws that result in regions of significantly higher than average stresses within the materials, thus causing fracture to be initiated even when the average stress on the material is less than its cohesive strength.

How do ductile materials fracture when dislocations are pinned, and how do brittle materials fracture when there are no flaws? Dislocations in engineering ductile materials are routinely pinned by work hardening and by precipitation hardening so that processes giving ductility are deactivated and failure occurs by brittle fracture. When there are no flaws present in brittle materials, the fracture of these materials becomes dependent on the dynamic aspects of materials.

The importance of the dynamics of failure in ductile materials has long been accepted. As a result, the dynamics of failure in ductile materials has been extensively studied. However, the dynamics of failure in brittle materials is not so well understood, because brittleness has traditionally implied that fracture is complete almost as soon as it has begun.

blocked by either inertial barriers, where particles may possess too much kinetic energy to stay in the deepest potential wells, or potential barriers, where particles may not have enough kinetic energy to get out of shallow potential wells, within the short time allowed by the simulation.

Although the limitations of molecular dynamics are numerous, its strengths are obvious. Molecular dynamics is a technique that can be used to study the atomic processes and the resulting properties of material systems that are not conducive to a study by analytic means. A quick inspection of the disordered surfaces of fragments of a fracture event illustrates the complexities involved in fracture. Thus, molecular dynamics offers the ability to witness the events that occur during fracture that result in these surface morphologies.

Processes in noncrystalline solids such as vitreous silica cannot be understood without such a simulation technique because of the complexities involved. Traditionally, the properties of glasses have been described by thermodynamics because of an inability to understand the dynamics involved. Most glasses have an enthalpy function of temperature that displays a glass transition region. The glass transition region is the temperature region wherein the enthalpy in a super-cooled liquid ceases to behave as a liquid and begins to behave as a solid upon cooling. The laws of thermodynamics tell us that within the glass transition region there must be certain limits on the changes in enthalpy. For example, since both the enthalpy and the specific heat of a liquid are greater than those for a crystal, a linear extrapolation of the enthalpy function for a liquid to lower temperatures may cross the enthalpy function for the crystalline phase.

However, because of the excess configurational potential energy of a liquid as compared to a crystal, the enthalpy of a liquid should never be lower than the enthalpy of a crystal at the same temperature. This is the Kauzmann Paradox. In a sense, it guarantees that the liquid of the composition must go through a glass transition if it does not crystallize first. After a material passes through a glass transition upon cooling, its structure becomes configurationally arrested, and both glass and crystal phases have nearly the same specific heats. At this point the glass and crystal enthalpy curves become parallel, so that the glass curve will not cross the crystal curve, therefore avoiding the paradoxical situation. Simulation is important in the investigation of these transformations because one can pinpoint the types of liquid-like behaviors possible at different temperatures, rather than lumping behaviors into a featureless normal distribution. Thus, nonequilibrium molecular dynamics has become an important technique in the study of glasses.

It is in this backdrop that simulations of fracture in a brittle material, a glass, vitreous silica are performed. Molecular dynamics not only gives us the ability to simulate a dynamics event such as fracture, it provides us also with a way to obtain the structure, in the case of a glass, so that these simulations can be performed on facsimiles of real materials. Limited as it may be, MD gives us the ability to study the events that we cannot view directly.

Statement of Problem

Vitreous silica is a material in which the intrinsic fracture behavior has become important. Silica optical fibers are routinely made to near theoretical strength by eliminating surface and bulk flaws. Despite this control over the state of flaws in this material, variations in the strength of samples still exist. The Griffith criterion, when applied to the variation in sample strengths, predicts flaw sizes on the order of a few angstroms. This work seeks to find the source of this variation in strength in this material.

Additionally, the dynamics of fracture, although not directly observable in fracture experiments, leave a signature on the resulting fracture surfaces. Reading this signature is the subject of the science of fractography. Fractography has been successful in locating the flaw that initiated fracture and in finding the state of stress in the material when fracture was initiated. However, the dynamic processes that result in the exact path that fracture takes after being initiated have remained elusive. The simulation technique that we use should be able to shed some light on these processes.

CHAPTER 2 BACKGROUND

In this work, we use molecular dynamics simulations to study the atomic-scale fracture processes in silica. Therefore, we will review the important aspects of this study. Since we hope to generalize the results of our brittle fracture simulations to brittle fracture in general, we will start with a discussion of fracture. Then we will examine the various phases of silica that are at the center of our particular study. We will then discuss the technique of molecular dynamics, including the limitations of this technique as well as the extent of applications. Various simulation models for silica will then be reviewed. We will then describe how fracture is simulated and studied using molecular dynamics. Finally, we will identify the aspects of fracture that a dynamical technique such as MD may allow us to study. Because of the various fields that are drawn together, a smooth progression between topics will not be attempted in the background section.

Brittle Fracture

Characteristics of Brittle Fracture

Brittle fracture is the mechanical failure of a material without plastic deformation. Brittle fracture is not limited to traditionally brittle materials. Metals or polymer materials that are considered to be plastic or ductile can be brittle under certain conditions of temperature and strain rate. Even inorganic glasses that are the epitome of brittle solids at room temperatures behave as viscous liquids at temperatures above the glass transition and are not brittle at low strain rates.

Experimentally, brittle fracture is generally a sudden process, so the dynamics of this process are not well known. Observations made during the fracture process by Dickinson et al.⁵ show that brittle fracture is accompanied by an ejection of particles and light. To date, measurements of these fractoemitted particles remain one of the few methods for characterizing the dynamic processes leading to brittle fracture.

The Ultimate Strength of Materials

The ultimate strength of a material without pre-existing surface flaws that fails by brittle fracture can be calculated based on a knowledge of its structure and the properties of its interatomic bonds. This value is known as the cohesive strength of the material, and it can be calculated for a material given the Young's modulus, the surface energies, the atomic structure, and an assumption of the form of the interatomic potential.^{2,6,7}

A cohesive strength calculation may use one of many pair potential functions. Two possible potentials are the Morse potential and the Born potential. The Morse potential is applicable to covalent systems and has the form $\phi_2(r) = \phi_o \left[e^{-2a(r-r_o)} - 2e^{-a(r-r_o)} \right]$

where $\phi_2(r)$ is the pair potential energy function of r , r is the interatomic distance, r_o is the equilibrium interatomic distance, and ϕ_o and a are constants that can be found from materials properties. The Born potential is applicable to ionic systems and has the form

$$\phi_2(r) = -\frac{A}{r} + \frac{B}{r^n}$$

where ϕ and r are as described above, and A , B , and n are constants that

can be found from materials properties.

Cohesive strengths are derived from these pair potential functions by calculating the derivatives of the functions and finding an expression for the maximum stress encountered in breaking the chemical bonds. Stress is defined as $\sigma = \frac{1}{A} \frac{d}{dr} \phi_2(r)$ where σ

is the stress, and A is the cross-sectional area covered by the bond. The maximum stress

is then found where $\frac{d}{dr} \phi_2(r)$ is a maximum, or when $\frac{d^2}{dr^2} \phi_2(r)$ is zero. Thus, the

theoretical cohesive strength is found by calculating the value of r for which $\frac{d^2}{dr^2} \phi_2(r)$

is zero, then substituting this value of r into the expression for $\sigma = \frac{1}{A} \frac{d\phi_2(r)}{dr}$.

The resulting expressions for the cohesive strength for the two potentials are, for

the Morse potential, $\sigma_{th} = \sqrt{\frac{Y\gamma}{4r_o}}$ and, for the Born potential, $\sigma_{th} = \frac{E}{2} \left(\frac{2}{n+1} \right)^{\frac{n+1}{n-1}}$ where γ

is the surface energy, E is the Young's modulus, and $n = \frac{1}{2} r_o E$.

For vitreous silica, with $E = 7.3 \times 10^{10}$ Pa, $\gamma = 4.56$ J/m², and $r_o = 1.62 \times 10^{-10}$ m, the theoretical strength given by the Morse potential is 23 GPa. This compares favorably with the highest strength of 14.3 GPa measured for treated silica fibers in liquid nitrogen by Proctor et al.,⁸ but is about two orders of magnitude greater than the measured strength for bulk silica or untreated silica fibers.

The Effect of Flaws

Discrepancies between theoretical strengths and measured strengths are common in brittle materials. This occurs because the presence of flaws in materials result in local strains that are much greater than the average strain within the material under stress. Plastic deformation does not readily occur in brittle materials, so the stresses in these areas of locally high strain cannot be relieved. These regions of high stress cause failure to occur in a material even when the average stress throughout is much less than the theoretical cohesive strength. Because of this, flaws may be considered as stress concentrators in the fracture of brittle materials.

Griffith¹ calculated the tensile stress, σ_c , which could be supported by a sample of a material containing a crack of a given length, c . His calculation was based on the assumption that a crack will propagate under an applied stress when the rate of decrease in elastic strain energy during crack propagation is greater than the rate of increase in surface energy resulting from the formation of new surfaces. Thus, for a sheet with an edge crack of length c , the critical stress is given by⁹
$$\sigma_c = \sqrt{\frac{2E\gamma}{\pi c}}$$
. Similar expressions

have been derived for various types of crack geometries.

Regimes of Brittle Fracture

The limiting processes in the brittle fracture of glasses in reactive environments are different in the three regimes categorized by Wiederhorn.¹⁰ Fracture processes of regimes I and II are limited by environmental effects and occur at stresses, or stress intensities, well below the theoretical strength of the material, and crack growth velocities are affected by species in the chemical environment. In type III fracture, the material becomes unstable under the applied stress without regard to environmental effects and the high crack growth velocities that result are limited only by the mechanical properties of the material.

Environmental Effects

Stress-induced corrosion or slow crack growth corresponding to types I and II fracture are important in limiting the strengths of materials in many applications.

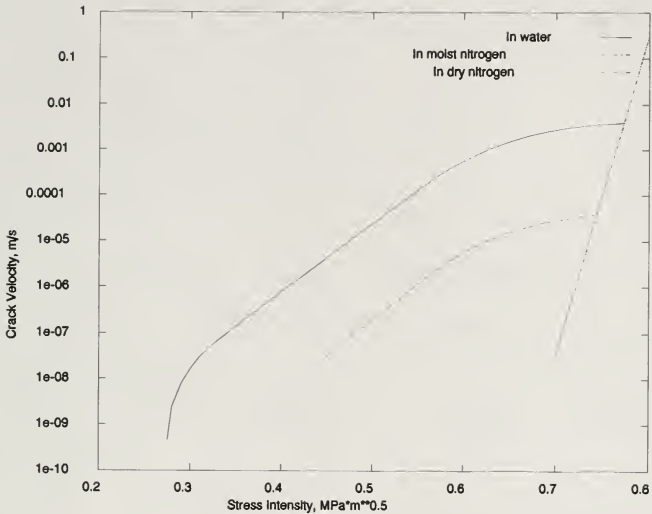


Figure 2-1. Schematic showing crack propagation velocities as a function of stress intensity factor. Adapted from Michalske.¹¹

Michalske¹¹ studied the fracture surfaces created by slow crack growth to better understand the mechanisms involved. In this type of fracture, environmental species diffuse to the crack tip, weakening the chemical bonds at the tip and causing crack growth at stress intensities less than σ_c but greater than some minimum stress. The velocity of the crack tip is then controlled by different mechanisms in the two regions. Since the reactivity of the material to corrosion at the crack tip is dependent on the local stress, the rate of reaction and therefore the crack growth velocity is dependent on the

stress intensity at the crack tip in type I fracture. The rate of diffusion of the environmental species to the crack tip controls the crack growth velocity and is nearly independent of the stress intensity in type II fracture. Thus, the crack growth velocity in region II has a lesser dependence on stress intensity than in region I. A schematic showing this behavior is given in Figure 2-1.

Crack Propagation Velocities

The maximum velocity of crack fronts in type III fracture is limited by the speed at which information of the approaching crack front may travel through the system. In a mechanical system, this speed is the speed of sound. Different methods have been applied to calculate to maximum crack propagation speed in real materials, giving similar

expressions of the form¹² $v_c = C \sqrt{\frac{E}{\rho}}$ where C is a constant between 0.4 and 0.6, and ρ

is the density of the material. Maximum crack velocities are found by experiment to be consistently less than, but on the same order as, the values given by the above expression.

Reading the Fracture Surface

Because brittle fracture is a sudden process that does not easily lend itself to real-time study, much of the analysis of brittle fracture is performed by fractography, the study of fracture surfaces. Since we seek to describe the processes occurring during fracture, we need to understand what fracture surfaces can tell us about these processes.

Through fractography, one can determine the location of the flaw that initiated fracture, determine the size of the initiating flaw, and determine the stress at which the sample fractured by examining the patterns on the fracture surface.

Brittle fracture surfaces have four distinct regions--the smooth mirror region near the initiating flaw, the rougher mist region beyond the mirror region followed by the coarse hackle region, and finally the crack branching region extending beyond the hackle to the limits of the fractured sample. By locating the smoother regions of a fracture surface, one approaches the area of the initiating flaw, and by advancing to the center of the smoothest region, the mirror region, one can pinpoint this flaw.

Fracture surfaces can provide information on the strain state of the material before fracture as well as the location of the initiating flaw. The transitions between the mirror and mist regions, the mist and hackle regions, and the hackle and crack-branching regions are distinct. It has been found that the radii of these regions are related to the failure stress by the relationship¹³ $\sigma_f \sqrt{r_j} = M_j$ where σ_f is the failure stress, r_j is the transition radius corresponding to either the mirror-mist, the mist-hackle, or the hackle-crack-branching transitions, and M_j is a material dependent constant for each of the transitions.

Recently efforts have been made to describe the aspects of the fracture surface that have traditionally eluded a meaningful quantitative description. These aspects are the seemingly random fluctuations that exist within all regions of fracture on varying

scales. Fractal geometry has been used to describe the statistical nature of these fluctuations, as will be discussed later in this review.

Silica

Bonding in Silica

Silica is the chemical compound SiO_2 . Oxygen is a group VI element and silicon is a group IV element. Oxygen is more electronegative than is silicon, but the difference in electronegativities is not great enough to make the bonding in SiO_2 purely ionic, so the bonding has significant covalent nature. Because silicon is a group IV element, it requires four bonds to complete its valence if covalent bonding is assumed, or it has four valence electrons to donate if ionic bonding is assumed. Oxygen is a group VI element, so it requires two bonds to complete its valence if covalent bonding is assumed, or it will gain two electrons to complete its valence if ionic bonding is assumed.

Structure of Silica

The basic structural unit of most condensed silica phases is the silica tetrahedron as shown in Figure 2-2.¹⁴ In each silica tetrahedron, there is one silicon atom tetrahedrally coordinated by four oxygen atoms. Each oxygen atom is then shared by two such tetrahedra to maintain local charge neutrality. Because the silica tetrahedron is the basic structural unit of silica glass as well as most crystalline phases of silica, even the glass phase is not without short-range order on the scale of a silica tetrahedron. Because of this, we refer to this phase as vitreous rather than amorphous.

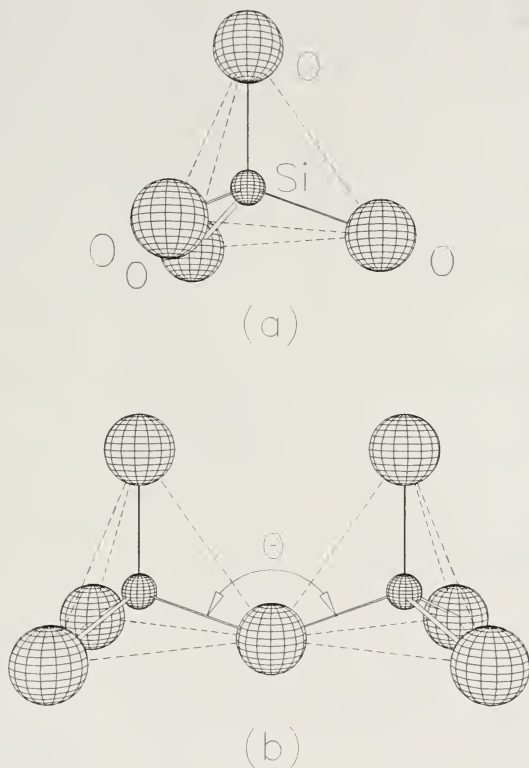


Figure 2-2. The silica tetrahedron is the basic structural unit of silica structures. a) One silica tetrahedron. b) Two tetrahedra linked by corner sharing. θ is the Si-O-Si bond angle. Adapted from Holloway.¹⁴

Phases of Silica

Because silica structures are relatively open, they are relatively free to change symmetry with temperature. Thus, silica comes in several polymorphic phases. The major crystalline phases of silica are quartz, the phase thermodynamically stable at temperatures below 1140 K, tridymite, stable in the temperature range of 1140 K to 1770 K, cristobalite, stable between 1740 K and the melting point of 2000 K, and coesite, the high pressure phase.^{15,16} In addition, there are further distinctions within the individual phases. The quartz, tridymite, and cristobalite phases are subdivided into high and low subphases. The transformations between the subphases are displacive, meaning that there is no rearrangement of the structural elements necessary for transformation, only reorientation of the structural units. The transformations between the major phases are reconstructive, meaning that there are structural rearrangements required to go from one phase to another. The vitreous phase is the usual result of cooling molten silica to a solid when no effort is made to induce crystallization. For a summary of the phases of silica, see the review article by T.D. Coyle.¹⁷

In crystalline silica, the tetrahedral units are linked in an orderly fashion, resulting in a structure possessing long-range order. In vitreous silica, the tetrahedra are linked in an apparent disordered fashion. This results in a structure possessing short-range order given by the rigid constraints on the size and shapes of the tetrahedral units, which diminishes rapidly beyond the first coordination distance because of the less ordered

Table 2-1
 Characteristics of the Phases of Silica

| Phase | Symmetry | Density (g/cm ³) | Tet Linkage |
|--------------|------------------|------------------------------|-----------------------------|
| Low Quartz | Hexagonal | 2.6 | Corner |
| Tridymite | Hexagonal | 2.22 | Corner |
| Cristobalite | Tetragonal-Cubic | 2.33 | Corner |
| Coesite | Monoclinic | 3.01 | Corner |
| Keatite | Tetragonal | | Corner |
| Shishovite | Tetragonal | 4.35 | Octahedrally Coordinated |
| Silica-W | Tetragonal | 1.97 | Edge |
| Vitreous | NA | 2.20 | Corner |

linkage of the tetrahedral units. The characteristics of the phases of silica are given in Table 2-1.

The Crystal Structure of Cristobalite

Cristobalite is of interest to us because its high symmetry, low density structure is probably the most comparable to the vitreous phase. At room temperatures, both phases are essentially thermally arrested high temperature phases. Thus cristobalite is the crystal phase of choice to compare to vitreous silica in studies of the effects of structural order and disorder in silica.

Although quartz may be the equilibrium phase, the cristobalite phase can be relatively stable when quenched to low temperatures because the reconstructive

transformations between the major phases is slow. Within the cristobalite polymorph, two sub-polymorphs are present, high, or beta, and low, or alpha, cristobalite, which undergo a displacive transformation within the temperature range of 470 - 540 K. This displacive transformation results in a symmetry change from the high temperature cubic symmetry to the lower temperature tetragonal symmetry upon cooling.

The structure of high cristobalite¹⁸ is similar to the diamond structure. The silicon atoms are in the diamond positions and oxygen atoms are located between each pair of silicon nearest neighbors. The symmetry of high cristobalite is cubic, and the structure belongs to the $Fd\bar{3}m$ (O_h^7) space group. The unit cell of high cristobalite has an edge length of 7.16 Å at 560 K and contains eight formula units.

The structure of low cristobalite has the same connectivity as the high cristobalite structure. Although this phase has tetragonal symmetry with prism dimensions $a_0 = 4.96$ Å and $c_0 = 6.92$ Å, the structure is pseudocubic when the cell is rotated by 45° about the c-axis and the sides a_0 are transformed into diagonals of the base of the prism, that is, $a'_0 = \sqrt{2} a_0 = 7.02$ Å and $c'_0 = c_0 = 6.92$ Å. In this description, the structure is a relatively small distortion of the high cristobalite structure. The unit cell of low cristobalite contains four formula units and belongs to the space group $P4_12_1$ (D_4^4).

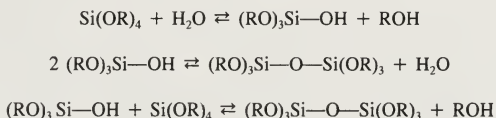
The Ring Structure of Silica

A useful description of intermediate structure in the phases of silica is the ring-size distribution. The statistical nature of this measure allows it to be used for vitreous

silica structures as well as crystalline structures. The ring structure plays prominently in the description of silicate structures because these structures are relatively open as a result of the low coordination of silicon and oxygen atoms, allowing identification of individual rings in the network.

A ring in a silica structure is a closed loop of adjoining tetrahedra that are identified by the number of tetrahedra contained in the ring rather than by the number of atoms that are bonded to form the ring. Work by Galeener¹⁹ has shown that different numbers of tetrahedra in rings give rise to differences in the energies of the structure. Works by Mariani and Hobbs^{20,21} and Mariani and Burdett²² have described the topological constraints on the ring size distributions in crystalline and vitreous forms of silica and on vitreous silica surfaces. Most crystalline forms of silica are composed entirely of six-membered rings, whereas vitreous forms necessarily have some ring sizes different from six.

The ability to make vitreous silica by a sol-gel route has enabled a detailed study of the role of rings in the formation of a silica network structure. In sol-gel processing of silica, silicon alkoxide precursors in an aqueous solution undergo condensation reactions such as the following, where alkoxides are identified by the formula unit (OR):²³



As the polymerization process continues, a network structure gradually forms. Because of the thermal and environmental constraints on the system, the resulting gel is not generally structurally similar to bulk silica. The absence of a high temperature step in the gelation process prevents the system from exploring different structural configurations that would result in the system seeking a global metastable state similar to that obtained by fused silica. Instead, the system structure is the result of a growth process by which $\text{Si}(\text{OR})_4$ molecules react first to form chains, then to form a network structure as $\text{SiO}_n(\text{OR})_{(4-n)}$ groups become linked with an associated loss of water molecules. Because the interim structure results from the dynamic growth process emanating from reaction centers, the structure tends to be fractallike--the geometry of the structure grows from a center point and through a series of branches, attempts to fill space. Silica gels are transformed into bulk silica structures by the processes of drying, stabilizing, and densifying. During drying, liquid water and reaction by-products are removed from the gel. In stabilization, physically adsorbed water is removed. Finally in densification, chemically adsorbed water is removed, and the structure attains full connectivity. During the densification step, structural changes occur that elucidate some of the medium-range structural details of silica.

Raman studies of gels during the densification process tell an interesting story. Superimposed on a somewhat broad Raman spectrum are narrow "defect" bands at 490 and 608 cm^{-1} , so called because their presence cannot be explained by continuous random network models.²⁴ As gels are stabilized by driving off chemically combined water in the structures and then densified by collapsing the porous gel structure, the intensity of

these defect bands increase, then decrease. This has permitted identification of these bands with the condensation of dangling silanol groups on the surfaces of the gels. As these dangling bonds become linked, highly strained three- and four- membered rings are formed and subsequently destroyed as the gel densifies and the internal surfaces are eliminated. This shows that the concept of rings corresponds to a real structural component in silica glass.

Elastic Properties of Vitreous Silica

Mallinder and Proctor²⁵ found that vitreous silica at low temperatures displayed a nonlinear elastic modulus in which the apparent elastic modulus is increased at high strains. At 77 K, the Young's modulus, E , and the shear modulus, G , as functions of strain, ϵ , were found to be $E=71.9(1+5.75\epsilon)$ GPa and $G=31.5(1+3.06\epsilon)$ GPa, respectively. The authors attributed this behavior to the opening of Si-O-Si bond angles in the structure, causing the elongation of silica rings. They reasoned that extension of the structure could be more easily accomplished by initially opening the Si-O-Si bond angle than by elongation of Si-O bonds.

The same authors also found that sodium silicate glasses exhibited a nonlinear elastic modulus in which the apparent elastic modulus decreased with increasing strain under similar conditions. In this case the authors reasoned that the extra cations were positioned in the structure so as to prevent the rotation of tetrahedra under low strain. The function for the elastic modulus given for this material was given as $E=71.1(1-5.11\epsilon)$ GPa.

Thomas and Brown²⁶ studied the elastic properties of fused silica and found that this material exhibited a similar nonlinear elastic modulus at room temperature. The authors suggested that this anomaly may play an important role in crack propagation and fracture.

Proctor²⁷ examined the effects of a nonlinear elastic modulus on the fracture behavior of fused silica. The author concluded that the nonlinear elastic effect must be considered when calculating either failure strains in high strength samples or stress values from failure strains, but that the nonlinear effects on the calculations of the size of fundamental Griffith flaws are self-cancelling and generally can be neglected.

Kulawansa et al.²⁸ performed an atomic force microscopy (AFM) study on silica fracture surfaces. The authors of this study analyzed the details of the fracture surface. They explained that some of the surface features observed were the result of a crack blunting mechanism caused by a hardening of the material under high strain, as they claimed would be consistent with a nonlinear elastic modulus that increases with strain.

The Fracture Strength of Silica

Measurements of the strengths of silica fibers indicate that nearly flaw-free fibers have been produced. Proctor et al.⁸ performed strength measurements on as-drawn fibers and found a narrow distribution of material strengths, indicating that samples were nearly flaw free. When the samples were fractured in liquid nitrogen, the authors obtained a maximum strength of 14.3 GPa. Kurkjian and Paek²⁹ performed an analysis of the tensile strength statistics for silica fibers and found that most of the variability of the

apparent strengths of fibers could be attributed to the variability of fiber diameters along the gauge length of the tensile test, giving a nearly single-valued strength of 5.75 GPa with a variation of less than 1%.

In a seminar at the University of Florida Department of Materials Science and Engineering in the Spring of 1990, Kurkjian noted that measurements suggested that fiber strengths were not completely single valued and indicated the presence of flaw sizes on the order of a few angstroms. A scanning tunnelling microscope (STM) was used to examine the topography of as-drawn fiber surfaces to explore the nature of the possible flaws.

Proctor²⁷ interpreted fracture strengths for silica fibers and found that average stresses were well below the highest measured value. Using elastic modulus data obtained in earlier work, he obtained values of flaw sizes of 3.6 nm for fused silica fibers and 7 nm for soda-lime glass. He then made the assumption that the most prevalent surface flaw is the largest broken ring of silica tetrahedra on the surface of the fiber and thus deduced average ring sizes of 5 to 7 tetrahedra for fused silica and 8 to 12 tetrahedra for borosilicate glass. The corrected strengths obtained from the later strength data ranged from 17.9 to 18.7 GPa for fused silica and 6.8 to 10.1 GPa for borosilicate glass.

Stress Corrosion of Silica

A model for the chemical reactions resulting in the stress corrosion of vitreous silica was proposed by Michalske and Freiman³ and was further explored by Michalske

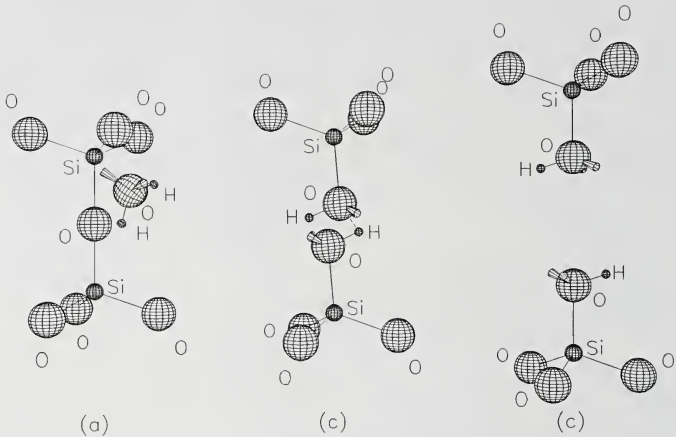


Figure 2-3. Chemical reaction proposed by Michalske and Freiman for environmentally enhanced Si-O-Si bond rupture. The strained crack tip bond (a) adsorbs a water molecule, (b) is cleaved by dissociative reaction, and (c) is converted to surface silanol groups. Adapted from Michalske and Bunker.³⁰

and Bunker.³⁰ In this model, the authors propose that a water molecule aligns itself with a strained Si-O-Si bond, resulting in a weakening of the bond, and the water molecule is consumed in a reaction that breaks the bond and creates a pair of silanol groups. By this model, three properties may be common to all active corrosive species: (1) the molecule has at least one lone (nonbonding) electron pair (Lewis base), (2) the molecule possesses a labile proton (Bronsted acid), and (3) the distance between the acid and base sites conforms with the Si-O bond distance (0.163 nm). A schematic of this process is given in Figure 2-3 and shows three stages in bond cleavage.

Hench and West^{31,32} studied the reaction paths in the fracture of Si-O bonds in rings of various sizes using molecular orbital calculations. They found that when particular bonds of unconstrained rings were strained, the energies required to break the bonds were significantly lower than the expected energy of the Si-O bond. This behavior resulted because unconstrained rings of various sizes, each having one strained Si-O bond, underwent a ring contraction mechanism whereby another tetrahedron within the ring approached the oxygen atom of the strained bond, five-coordinating the tetrahedron, and weakening the initially strained Si-O bond. The authors found that 4-membered rings were the weakest rings, with an activation energy for Si-O bond breakage of 320 kJ·mol⁻¹, followed by 3-membered rings with an activation energy of 400 kJ·mol⁻¹, and 5-membered rings with an activation energy of 430 kJ·mol⁻¹. When water was introduced into the system, the various sized rings showed different tendencies for hydrolysis, the critical step in environmentally assisted fracture. In this case, the authors found that 3-membered rings were the easiest to hydrolyze, with an activation energy of 30 kJ·mol⁻¹, followed by 4-membered rings, with an activation energy of 120 kJ·mol⁻¹ and 5-membered rings with an activation energy of 160 kJ·mol⁻¹. In both the water-free and water-present cases, the authors concluded that the ring structure of bulk silica influences the fracture of Si-O bonds, and must be considered when studying this process.

Because water is an active component in the stress corrosion of silica, and since it is prevalent throughout the atmosphere, it plays an important role in all fracture experiments on silica except for those experiments in which it is purposely and carefully

excluded. Understanding the role of water is of vital importance when interpreting the observations of any fracture experiment. The fracture of silica in the absence of water is quite different from the fracture of silica in a water-free environment, as demonstrated by a comparison of strengths measured by Proctor⁸ (14.1 GPa) in a water-free environment at 77 K and by Kurkjian and Paek²⁹ (5.75 GPa) in a laboratory environment at room temperature.

All simulations to be presented in this work pertain solely to a water-free environment.

Molecular Dynamics

Survey of Applications

A molecular dynamic (MD) simulation is, as its name implies, a technique that models the movement (the dynamics) of particles (of molecules). As pointed out by Hoover³³ in an introductory article on the subject, interesting results can be obtained from even the simplest of systems because of the many-body interactions that may be involved.

Molecular dynamic simulations are not difficult to visualize. Imagine the collective motion of several balls on a billiard table with a frictionless surface and perfectly elastic bumpers. Imagine now a computer model of this motion, and you have envisioned an MD simulation of a two-dimensional hard-sphere system with rather peculiar boundary conditions. Further, MD simulations are capable of extracting thermodynamic quantities such as pressure and temperature from the dynamic system,

providing a simulation link between the system of discrete particles in motion and the thermodynamic quantities that describe that system.

Molecular dynamic simulations were first used by Rahman⁴ to study the correlations of atomic motions in liquid argon. MD was first used in simulations of liquids for various reasons. Clearly, liquids are dominated by particle dynamics, therefore, their properties can be quite well simulated by MD methods. Since liquids are fluid, their structures are sufficiently dynamic so that slow nucleation and growth processes are not required to obtain reasonable simulations of their structures, and comparatively short MD simulations are capable of simulating reasonable structures. Finally, despite the dynamic nature of liquid, there are strong interactions among atoms and transient structures of sufficient interest to warrant a simulation of structure and properties, as opposed to an ideal gas where there is little interaction between atoms and no structure.

The applications for MD simulations have expanded over time. Non-equilibrium MD is concerned with the dynamics of systems and not in thermodynamic equilibrium, and is used in simulating glass structures. The structure and dynamics of materials surfaces have been studied. For example, Heyes et al.^{34,35} and Heyes³⁶ studied the structure and dynamics of surface and near-surface regions in ionic crystal films. Broughton and Gilmer^{37,38,39} studied crystal-fluid interfaces of Lennard-Jones metals. Gilmer, Grabow, and Bakker⁴⁰ used MD simulations to model epitaxial growth in Lennard-Jones systems. Brünger et al.⁴¹ reported the use of MD simulations in the

determination of crystallographic structures of protein molecules from X-ray and neutron diffraction data.

There has been recent interest in using MD to study the interactions between surfaces in a field called "nanotribology." Landman and Luedtke⁴² reported MD simulation results in studies of the interaction of metal tips with metal substrates. Harrison et al.⁴³ reported the use of MD in studies of friction between diamond surfaces. Belak et al.⁴⁴ used MD simulations to model atomic scale deformation of surfaces by a process similar to machining.

The evolution of computer hardware, along with the evolution of computer codes, is continually increasing the capabilities of MD simulations. MD simulation codes are capable of being run efficiently on parallel computers with some modification. Furthermore, researchers have developed specialized computers for performing certain simulations more quickly and efficiently. An example of such a computer is described by Bakker et al.⁴⁵ A result of the development in computer hardware is that systems composed of tens of millions of particles can now be simulated on parallel computers consisting of thousands of processors, whereas systems having fewer than one thousand particles were simulated in the infancy of MD.

Recently, MD simulations have reached popular appeal with the advent of commercially available MD simulation software packages, such as the Insight package from BioSym Inc. One can now buy a simulation system that is capable of simulating a wide range of materials and configurations. It is likely that the use of MD in all types of materials simulations will increase dramatically since it is no longer necessary to either

write simulation codes or modify existing simulation codes for a wide range of applications. Despite the advent of commercially available simulation codes, many researchers will most likely continue using custom-made codes, which are optimized for the simulation of certain systems or to run on specific computer hardware.

Survey of Potential Functions

The identity of a simulation is strongly dependent on the potential function used, which in turn is based on the type of bonding in the material being simulated. There are several common potential functions that are used in MD simulations.

In order to simplify the description of the various potential functions in common usage, we will use the same means of summation for all potentials, and common symbols whenever possible to permit comparison between the potentials (see the Key to Symbols in the Appendix). Summations are not necessarily listed as they would be performed the most efficiently in the computer code, but are written for logical simplicity. The general interaction potential for a system will be written as

$$\Phi = \sum_{i=1}^N \left[\frac{1}{2} \sum_{j \neq i} \left(\phi_{2uv}(r_{ij}) + \sum_{k \neq i, k \neq j} \phi_{3uvw}(r_i, r_j, r_k) \right) \right]$$

where N is the number of atoms in the system,

i, j , and k represent individual *atoms* as specified in the summations,

u, v , and w represent the atom *types* of i, j , and k , respectively,

$\phi_{2uv}(r_{ij})$ is the function representing the two body portion of the potential for types

u and v , and

$\phi_{3uvw}(r_i, r_j, r_k)$ is the function representing the three body portion of the potential for types u , v , and w . Since the three body portion of the potential is most often a function of two bond lengths and a bond angle, it may usually be equivalently referred to as $\phi_{\theta uvw}(r_{ij}, r_{jk}, \theta_{ijk})$. We have written the summations to work most directly with this form because it is applicable among all the three-body potential functions that we will review.

The use of indices u , v , and w to denote atom types is a departure from the usual notation in the literature. This notation is used to unambiguously differentiate the constants or functions are dependent on atom types only from the variables that are dependent on individual atoms. Although this is usually clear from context, there have been some cases of ambiguities and errors in the literature. For systems of only one atom type, the subscripts u , v , and w will not be used.

A common pair-potential used for the condensed phases of noble elements is the Lennard-Jones 6-12 potential. The function for this potential is $\phi_2(r) = -\frac{A}{r^6} + \frac{B}{r^{12}}$, where A and B are positive constants and r is the distance between atoms. This potential is usually written in the dimensionally more appealing form $\phi_2(r_{ij}) = 4\epsilon f_2\left(\frac{r_{ij}}{\sigma}\right)$, where $f_2(r) = r^{12} - r^6$ is a dimensionless function, and $\sigma = (B/A)^{1/6}$ and $\epsilon = A^2/4B$ are constants.⁴⁶ This potential was also commonly used in the simulation of metals, since it often results in a close-packed crystal structure similar to the structure of many metals.

Recently, a potential based on the embedded-atom-method (EAM) developed by Daw and Baskes⁴⁷ has become a popular method of simulating processes in metals with empty or filled d bands.⁴⁸ This potential uses the assumption that atoms are embedded into a local electron density provided by the remaining atoms of the system. The electron density function of the system is a many-body interaction problem, so this potential is a many-body potential. This potential has an advantage in metals because it is less empirical than is the Lennard-Jones 6-12 potential traditionally used in these systems.

Covalently bonded materials require a potential with an angularly dependent term to simulate the angularly dependent bonds that result from bonding through molecular orbitals. One such potential was developed for silicon by Stillinger and Weber.⁴⁹ An angular dependence is obtained by adding an appropriate three-body term to a truncated Lennard-Jones-type potential. The form of the potential is $\phi_2(r_{ij}) = \epsilon f_2\left(\frac{r_{ij}}{\sigma}\right)$ for the two-

body part, and $\phi_\theta(r_{ij}, r_{jk}, \theta_{ijk}) = \epsilon f_\theta\left(\frac{r_{ij}}{\sigma}, \frac{r_{jk}}{\sigma}, \theta_{ijk}\right)$ for the three-body part. The function f_2 in the

two-body part of the potential is

$$f_2(r) = \begin{cases} A(Br^{-p} - r^{-q}) \exp\left(\frac{1}{r-a}\right), & r < a \\ 0, & r \geq a \end{cases}$$

while the function f_θ in the three-body part of the potential is

$$f_{\theta}(r_{ij}, r_{jk}, \theta_{ijk}) = \begin{cases} \lambda \exp\left(\frac{\gamma}{r_{ij}-a} + \frac{\gamma}{r_{jk}-a}\right) \left(\cos\theta_{ijk} + \frac{1}{3}\right)^2, & r_{ij} < a \wedge r_{jk} < a \\ 0, & r_{ij} \geq a \vee r_{jk} \geq a, \end{cases}$$

and the constants ϵ and σ serve to make f_2 and f_{θ} dimensionless functions.

Ionic materials are generally modeled using a potential that incorporates a coulombic potential with an exponential repulsive term. The Born-Mayer-Huggins potential is such a potential. It has the general form

$$\phi_{2uv}(r_{ij}) = \frac{q_u q_v}{r_{ij}} + A_{uv} e^{-br_{ij}} + C_{uv} r_{ij}^{-6} + D_{uv} r_{ij}^{-8}$$

where r_{ij} is the inter-ionic distance, q_u and q_v are the ionic charges, and A_{uv} , b , C_{uv} , and D_{uv} are constants.

Potentials for Silica

There are several commonly used potentials for modeling silica. The first of these is a variant of the Born-Mayer-Huggins described by Busing,⁵⁰ first used in silica by Woodcock et al.⁵¹ and later modified by Soules. The second is a variant of the Born-Mayer-Huggins potential that incorporates a three-body term similar to that used in the Stillinger-Weber potential. These two potentials will be described in detail in the procedure section of Chapter 4.

Vashishta et al.⁵² derived a potential function that included a three-body part and applied it to various silica polymorphs. The two-body portion of the potential is given by

$$\phi_{2uv}(r_{ij}) = \frac{H_{uv}}{r_{ij}^{\eta_{uv}}} + \frac{q_u q_v}{r_{ij}} - \frac{1}{2} (\alpha_u Z_v^2 + \alpha_v Z_u^2) \frac{1}{r_{ij}^4} e^{-r_{ij}/r_u}$$

and the three-body portion of the potential is given by

$$\phi_{\theta_{uvw}}(r_{ij}, r_{jk}, \theta_{ijk}) = \begin{cases} B_{uvw} \exp\left(\frac{l}{r_{ij}-r_0} + \frac{l}{r_{jk}-r_0}\right) (\cos\theta_{ijk} - \cos\bar{\theta}_{uvw})^2, & r_{ij} < r_0 \wedge r_{jk} < r_0 \\ 0, & r_{ij} > r_0 \vee r_{jk} > r_0 \end{cases}$$

with constants H_{uv} and η_{uv} representing the strengths and exponents of the steric repulsion, Z_u and α_u representing the effective charge and the electronic polarizability of ions of type u , r_{0i} representing the decay length of the r^{-4} interaction term, B_{uvw} , r_0 , and $\bar{\theta}_{uvw}$ representing the strength, the cutoff distance and the preferred bond angle for the three-body interaction, and l an unspecified constant. The authors claim that this potential gives the correct Si-O-Si bond angle distribution where earlier potentials failed.

Another potential function that is now commonly used for silica is described by Vessal et al.⁵³ This potential function has the most adjustable parameters of any reviewed here, and claims an excellent fit to experimentally measured properties of various phases of silica. Wright⁵⁴ found this potential created a vitreous silica structure

having the best fit to neutron diffraction data of any MD simulated structure at the time of the comparison. The authors also claim agreement with the presumed Si-O-Si bond angle distribution in real silica. The functional form of this potential is quite complex. The two-body portion of the potential has long-range and short-range parts. The long-range Coulombic portion of the potential is calculated using the Ewald⁵⁵ method applied to a fully ionic system of silicon and oxygen. The short-range part of the potential is given by the four-part Buckingham potential

$$\phi_{2uv}(r_{ij}) = \begin{cases} A_{uv} \exp\left(\frac{r_{ij}}{\rho_{uv}}\right), & r_{ij} < r_{1uv} \\ A_{1uv} r_{ij}^5 + B_{1uv} r_{ij}^4 + C_{1uv} r_{ij}^3 + D_{1uv} r_{ij}^2 + E_{1uv} r_{ij} + F_{1uv}, & r_{1uv} < r_{ij} < r_{2uv} \\ P_{1uv} r_{ij}^3 + Q_{1uv} r_{ij}^2 + R_{1uv} r_{ij} + S_{1uv}, & r_{2uv} < r_{ij} < r_{3uv} \\ -\frac{C_{uv}}{r_{ij}^6}, & r_{3uv} < r_{ij} < r_{cuv} \end{cases}$$

where r_{ij} is the interatomic distance between i and j , and most other constants are purely empirical. The three-body potential for O-Si-O interactions has the form

$$\phi_{\theta_{uvw}}(r_{ij}, r_{jk}, \theta_{ijk}) = \frac{1}{4} A_{uvw} \left(B(\theta_{ijk}) \right)^2 \exp\left(-\frac{r_{ij} + r_{jk}}{\rho} \right)$$

where A_{uvw} is a constant given by $A_{uvw} = \frac{k_{uvw}}{2(\theta_0 - \pi)^2}$, $B(\theta_{ijk})$ is a function given by

$B(\theta_{ijk}) = (\theta_0 - \pi)^2 - (\theta_{ijk} - \pi)^2$, and the constants k_{ijk} and θ_0 are the three-body spring constant and the tetrahedral bond angle, respectively. With various spline approximations, etc., this potential has more than 40 parameters. With so many adjustable parameters, it is not surprising that this potential function can claim the best fit to the experimental properties of silica, although the simultaneous optimization of all parameters is impressive nonetheless.

Alavi et al.⁵⁶ proposed a potential that adjusts the effective charge of silicon and oxygen ions based on their coordination. This potential was proposed to correct problems created when network-modifying ions are included in the structure in which some of the network forming ions are not fully coordinated. The concept of variable charge may be important in fracture studies as well where coordination of atoms change during fracture. Tsai et al.⁵⁷ have used such a mechanism in the simulation of fracture in silicon. Thus, this charge-transfer potential may be one to watch in the future.

Applications of MD in Models of Silica

Woodcock et al.⁵¹ first simulated a silica-like structure using a variant of the Born-Mayer-Huggins potential as used for ionic systems. These authors acknowledged

that a purely ionic potential was not fully applicable to a system with a fair degree of covalent character, but they tried the potential since it was available and easy to apply. Despite the known limitations of this potential, comparisons of simulation derived pair correlation functions (PCF's) with PCF's deduced from x-ray diffraction data showed rough agreement and a comparison of system energies showed that the potential energy calculated from the simulation was 5% less than an experimentally derived Born-Haber lattice energy for quartz. The authors made observations and performed experiments on the simulated system. They measured diffusion constants at various temperatures and pressures, and studied the permanent compaction of silica by the application of a compressive stress. Mitra et al.⁵⁸ performed simulations of vitreous silica structures using a variant of the Born-Mayer-Huggins potential and reported good agreement to x-ray and neutron diffraction data. These authors also examined the internal energy as a function of temperature and reported that the simulated system exhibited a glass transition at 1500 K.

Soules⁵⁹ performed a simulation of sodium silicate glasses using a potential similar to Woodcock et al.⁵¹ Again, the structure was reported to be in significant agreement to x-ray diffraction data. Soules found that alkali and alkaline earth cations clustered around non-bridging oxygens, as is generally predicted for these structures. Coordination information showed that the number of non-bridging oxygen atoms was strongly dependent on the amount of alkali ion present. Ring size distribution data showed changes with varying alkali content as well, although it was not clear from the limited extent of the reported ring size distribution what the changes were. Soules and Busbey⁶⁰

further performed simulations to study diffusion of sodium in alkali silicate glasses and found that diffusion coefficients obtained from simulation at high temperatures were in agreement with extrapolated experimentally measured values. They then concluded that purely ionic potentials for silica were sufficient to model transport properties.

Garofalini and Levine,⁶¹ and Feuston and Garofalini⁶² examined the structural changes on surfaces of vitreous silica. These simulations created arbitrary surfaces by removing periodic boundary conditions between a pair of sides of the MD cell. The general finding of these simulations was that less-highly charged ions tended to segregate toward the surfaces. In pure vitreous silica, these species were oxygen ions, while in the alkali silicates, alkali ions also tended to segregate toward the surfaces.

Garofalini⁶³ studied the reactivity of water on vitreous silica surfaces. He found that water reacts with a silica surface through a series of penta-coordinated silicon transition geometries in which water molecules are somewhat paired on the surfaces.

Comparisons of Simulated Structure to Experiment

Researchers generally do not like to point out the discrepancies of their models in the published results of their MD simulations. They often compare radial distribution functions derived from simulation with those deduced from diffraction experiments, and if there are the same number of peaks in the distribution function and they occur in the same general location, they call it a "good" fit. However, based on some minimal constraints on the structure such as the preferred Si-O bond length for silica, in no case can radial distributions be too far wrong. Wright^{64,54} has attacked the casual comparisons

of RDF's derived from MD simulated structures to the RDF's deduced from experimental techniques such as neutron diffraction data and has proposed a standard for comparing the experimental and simulated RDF's. This standard is a variant of the

crystallographic R factor, and is given by
$$R_x = \sqrt{\frac{\sum_i [T_{\text{exp}}(r_i) - T_{\text{sim}}(r_i)]^2}{\sum_i T_{\text{exp}}^2(r_i)}} .$$
 By this standard,

the current champion in the fit of simulated structure to experiment is Vessal et al.⁶⁵ with an R_x factor of 9.0% .

MD Simulations of Fracture

The use of molecular dynamics for studying the failure of materials is not new. Two approaches have been taken in these studies. The first has been to perform fracture experiments in simplified MD systems in order to perform detailed studies of the elements of fracture. The second has been to study fracture using MD simulations that attempt to model real systems.

Paskin et al.,^{66,67} Dienes and Paskin,⁶⁸ and Sieradzki et al.⁶⁹ performed simulations of crack growth in two-dimensional crystalline lattices. These works demonstrated the applicability of the Griffith criteria in simple 2-D systems modeled by molecular dynamics, and studied mechanisms of crack growth, including the formation of dislocations and speed of crack propagation, as functions of applied stress, crack length,

and potential parameters. These works provide an atomistic basis to fracture mechanics, however, they do not provide details on the fracture of particular materials.

MD simulations of fracture in silicate glasses were first performed by Soules and Busbey⁷⁰ on sodium silicate glass samples at elevated temperatures. The periodic boundary conditions used made this experiment equivalent to the fracture of a fiber with a diameter of about 50 Å, so this study did not model fracture in a bulk material. The essential characteristic of glass fibers in the real world that gives them interesting mechanical properties is the absence of surface flaws, resulting in nearly theoretical strengths, but the simulated "fibers" did not share this characteristic. At the atomic scale, the surfaces appear rough and would not be considered pristine if the simulated "fibers" were scaled to the size of real fibers. Thus, behavior similar to fibers is not to be expected, and is not observed. What is observed is that samples undergo necking as the simulated surfaces dominate their mechanical properties. Cavitation within the samples is also observed, indicating that the system sometimes takes this route to absorb the added volume while maintaining connectivity and minimizing the total energy at each stage of strain.

Soules⁷¹ examined the role of the vitreous structure in the fracture of silica by comparing fracture in vitreous silica to fracture in high cristobalite silica. He investigated how the Si-O-Si bond must break during fracture and found that for the bond to break under an applied strain, the bridging oxygen must vibrate out of its potential well. Thus, he showed that fracture in silica is an activated process and undergoes a

relaxation. He also found that high cristobalite exhibited a high strength of 70 GPa as compared to a strength of 24 GPa for vitreous silica.

Kieffer and Angell⁷² applied an isotropic tensile strain to a silica sample in order to rupture the structure. They found that the resulting structures had a fractal character similar to that of aerogels, and that the fractal dimension was dependent on density but independent of strain rate, indicating that the fractal dimension for silica under a given set of thermodynamic constraints is unique.

Ochoa and Simmons⁷³ examined the role of strain rate in the fracture behavior of vitreous silica. They found that within the range of 0.4 - 4.0 ps⁻¹, the strength, as defined by the maximum stress supported by the system during strain to failure, increased as a function of strain rate from about 45 GPa to 95 GPa. They attributed the decrease in strength with decreasing strain rate to a relaxation process where atomic vibrations caused some reorientation of the structure capable of lowering its cohesive strength. They also found that the effects of strain on the structure were dependent on strain rate, with the highest strain rates causing an elongation of Si-O bonds and lower strain rates resulting in an opening of Si-O-Si bond angles in the strained structures prior to fracture. Finally, they discovered that the maximum stress did not occur at a strain immediately prior to rupture of the structure, but rather at some point where some fraction of the bonds were broken internal to the structure.

Ochoa et al.⁷⁴ examined the role of thermal vibrations in the fracture of vitreous silica and high cristobalite by simulating the fracture of these materials at strain rates ranging from 0.2 - 8.0 ps⁻¹. They used a potential function based on the Born-Mayer-

Huggins potential with two sets of potential parameters to investigate the sensitivity of results on a specific potential. The authors found that the maximum stress during strain-to-fracture increased with increasing strain rate for the vitreous silica samples, ranging from 30 GPa to 65 GPa, but was nearly independent of strain for the cristobalite sample at 80 GPa. They explained that the decrease in strength of the amorphous structure with decreasing strain rate was a result of rotation of $(\text{SiO}_4)^4$ tetrahedra during strain-to-fracture at low strain rates that was not allowed at high strain rates. They found that voids placed in the samples resulted in a decrease in the strengths of the samples and altered the mechanism of fracture at low strain rates. Finally, they found that the differences in the potential parameters did not significantly affect the behaviors observed.

Simmons et al.⁷⁵ examined the mechanisms required for stabilization of silica surfaces following fracture. They found that fracture is stabilized by the movement of dangling silicon atoms back into the structure, leaving predominantly oxygens on the surface, resulting in a repulsion between the two freshly created fracture surfaces.

Chaos in Fracture: Determinism and Fractal Surfaces

We earlier discussed brittle fracture in silica. That discussion was based on the principles of fracture mechanics--maximum strengths of static structures, the effects of flaws on the strength of materials, and the role of environmental species during fracture. However, although fracture mechanics may serve to identify the causes of fracture, it is ultimately unable to predict the path of fracture that results in the seemingly random structure of fracture surfaces. The complexities of fracture surfaces indicate that the

particular dynamics of the fracture process is important in determining the path of fracture. Although molecular dynamics simulations may be capable of elucidating the role of dynamic processes during fracture, we cannot analyze every atomic motion in the fracture of a simulated system. Because we can easily observe the deviation of the system when we make a small perturbation in the starting conditions, the concept of chaos with its sensitivity on initial conditions gives us a handle on analyzing the complex behavior that cannot be analyzed on an atom-by-atom basis. Thus, without looking at all dynamic interactions in detail, we can find the significance of these interactions in a qualitative way.

In nature, fractal-like shapes often result from chaotic processes. This is seen in brittle fracture as well. Thus we will also discuss fractal geometry and its appearance in brittle fracture.

Investigations of Chaotic Processes

"Chaotic" is a descriptive term applied to systems that follow paths which are strongly dependent on initial conditions. The term, "strongly dependent on initial conditions" implies that *any* deviation in initial conditions ultimately results in system paths as divergent as system paths resulting from large deviations in initial conditions.

The concept of chaos originated from simulation work of weather patterns by Lorenz.^{76,77} Lorenz found that small deviations in the starting conditions of a numerically solved differential equation resulted in a divergence of the system behavior over time. Although the paths of the systems remained close for some time, they gradually deviated

to the point that they no longer possessed any correlation that would indicate a shared beginning. The paths taken by the simulated systems deviated as a result of the loss of precision associated with converting the computer's internal representation of numbers into a decimal representation of limited precision, then re-converting this representation into an internal binary representation when re-starting the simulation. Although the simulation was not necessarily capable of a fully accurate representation of the weather, it demonstrated that without a total knowledge of starting conditions and external effects, the prediction of weather for indefinite periods of time would be impossible. The general implication of Lorenz's work is that the behavior of systems described by coupled nonlinear equations cannot be predicted within a certain range in the long term. In an MD simulation where a material described by coupled nonlinear potential functions, similar behaviors may be expected.

Mathematical descriptions of chaos are particular. One of the tools used in investigating the chaotic nature of a system is a Poincaré map, which is a map of the path of a system in a space of some or all of its variables. Chaotic systems are often found to have maps that approach but never achieve a periodic behavior, and such a map was constructed by Lorenz. Often a projection of these maps creates either a fractal or an intricate pattern. Another method used in investigating the chaotic nature of a system is an investigation of an apparently randomly varying quantity. In fractoemission experiments, Langford et al.⁷⁸ performed autocorrelation, Fourier transform, and box-counting dimension analyses on the curves of fractoemission intensity as functions of time. They found evidence of deterministic chaos from these analyses, and related it to

the fractal dimension of the resulting fracture surfaces as found by the slit-island technique. We will discuss the implications of a fractional dimension in a real material later in this review.

Predictability of Brittle Fracture

Fracture occurs when a mechanical system becomes unstable by the application of strain. What does it mean when a system becomes unstable? A system is unstable when it is in a state that will undergo a transformation to a favored state under any perturbation. This means that as a system becomes unstable, even previously insignificant dynamics within the system may play a role in determining the path to the favored state. This seems to be the case in brittle fracture where the fracture mechanics that can quite accurately predict when a system will become unstable is ultimately unable to predict the precise path to fracture after it has become unstable.

The choices available in predicting the path of brittle fracture are quite limited. Either brittle fracture either occurs by cleavage, where fracture surfaces approach atomic smoothness, or it does not. In cleavage, the path to fracture is known or controlled. But in all other fracture events, the path is not known and is not exactly controlled. For example, distributions of sample strengths have not been completely explained by known sample flaws as pointed out by Kurkjian previously. Also, according to a private discussion with T.A. Michalske in 1991, there appears to be some uncertainty in the dynamics of slow crack growth in pristine silica under vacuum where there should be no environmental effects, and thus, no effect of stress on the rate of crack growth. The

question arises--is the inability to completely describe the fracture process the result of this process being chaotic?

Fractal Geometry

A fractal is a mathematical set of points that is best described by fractal geometry and has a fractional dimension. Fractal geometry is a branch of mathematics that encompasses Euclidean geometry as a special case--the case of integral dimensions. Objects in geometry are idealized and are not realized in the physical world, and are referred to as sets. Although a set is a mathematical abstraction, physical objects may approximate sets. Thus, when a surface is described as being fractal, it really means that the shape of the surface approximates a fractal set, just as when a physical object is described as spherical, the description implies that the shape of the object approximates a sphere to certain tolerances. Thus, physical objects may be *fractal-like*, but they can not be *fractal*.

One of the most fundamental descriptions of a set is its size. The measurement of sets is made using mathematically rigorous techniques. In order to measure a set, the proper dimension for the set must be used. The Hausdorff dimension for a set is the dimension in which a meaningful measurement of the set can be made. As its definition is beyond the scope of this discussion, refer to Falconer⁷⁹ for a complete definition of the Hausdorff dimension.

The Hausdorff dimension is the only dimension for which the set may have a finite non-zero measure. For example, in Euclidean geometry, the measure of an area

is infinite if the measurement is made using a measure of length, is zero if the measurement is made using the measurement of volume, and can only be non-zero and finite only if the measurement is made using the same dimension of the set, that is, using a measurement of area. However, in contrast to examples of sets in Euclidean geometry, it is not always obvious in what dimension a measurement of a non-Euclidean set should be made. Thus, although the Hausdorff dimension is not in itself a measure, it is essential to the measurement process, and it is a useful descriptor for a set.

The Hausdorff dimension is the most fundamental definition of the dimension of a fractal set, but other definitions are also used. The box counting dimension operates

on the graph of a set, and is defined as $\dim_B F = \lim_{\delta \rightarrow 0} \frac{\log N_\delta(F)}{-\log \delta}$ where F is the set that

describes the object, the function N_δ gives the number of boxes of linear dimension δ required to cover F .⁷⁹ In many cases, the box-counting dimension is equivalent to the Hausdorff dimension.

Fractal sets are of interest to mathematicians because of their unusual properties, but why are sets that are best described using fractal geometry of interest to physical scientists? The answer is that shapes found in nature often approximate the shapes of fractal sets. Since mathematicians have discovered the generating functions for creating fractal sets, physical scientists may assume that the physical processes that result in the formation of such shapes are described by similar functions.

Several authors have related how physical objects approximate fractal shapes. The "proof" that they give to show that these objects are fractal is that the "fractal

dimension," a limited approximation to the box-counting dimension, is not an integer. The definition of "fractal dimension" used by Mecholsky et al.⁸⁰ is given by the relation $Nr^D = 1$, where D is the "fractal dimension," N is the number of boxes of size proportional to r that cover a set, or the number of ruler lengths proportional to r that measure the length of a curve. These are related to quantities in the definition of the box-counting dimension where $\dim_b F \rightarrow D$, $N_\delta \rightarrow N$, and $\delta \rightarrow r$. An important distinction is that no limit is involved in the definition of the "fractal dimension" as described here. Thus, the quantity D is a useful description of an object that approximates a fractal over a limited range of r . However, it does not prove that the object is fractal, only that it possess some properties that approximate those of a fractal object over a limited range of scale.

Although the Hausdorff dimension remains the most precise definition of the dimension of a fractal set, the term "fractal dimension" is often used in the physical sciences to denote the approximate box-counting dimension as defined above. Because of this, we will follow the same usage for the remainder of this work. However, one should bear in mind that this fractal dimension is obtained only over a limited range of scale, and the validity of extrapolations to different size scales must be tested.

Applications of Fractal Geometry to Fracture

Recently, there has been a great deal of interest in describing fracture surfaces using fractal geometry. There are several reasons for doing this.

The first is that all statistically significant details of these seemingly random surfaces can be described with a limited amount of information, because the same surface features may be found over a wide range of scales, with the atomic scale being the absolute lowest limit. Thus, the description of fracture surfaces using fractal geometry provides a possible link between those observations made by fractography and those made by atomic scale simulation.

The second is that a scalar quantity, the fractal dimension, is obtained for the description of fracture surfaces. Just as the pair correlation function is a useful description of a random glass structure, the fractal dimension is a description of the random structure of a fracture surface. However, a fractal dimension, like a pair correlation function, does not unambiguously describe the structure. It is merely a statistic of the structure that may be compared to test the possible similarities of various structures. Despite its limitations, the fractal dimension can be related to material fracture properties, as will be shown.

Finally, and probably most important from the standpoint of understanding fracture, a description of a fracture surface as fractal-like may help in the understanding of fracture processes. Fractal sets can be created by iterated generator functions. By describing a fracture surface as fractal-like, one may be able to find the generating function for the surface, and then elucidate some of the processes which occur during the progression of fracture. Since fractal-like shapes often imply a chaotic generation process, do the fractal characteristics of fracture surfaces imply that fracture is chaotic?

Later in this work, we will attempt to show how fracture may proceed to form fractal-like surfaces.

The Fractal-like Nature of Fracture Surfaces

If fracture occurred only by the orderly cleavage of crystal planes in crystals and it always created minimum energy surfaces in glasses consistent with the applied mechanical constraints, then the science of fracture would be nearly complete. However, brittle fracture is not that simple. During the formation of fracture surfaces, the effects of the dynamic lattice seem to counter the attempts of the material to minimize its surface energy. Even in the fracture of a highly ordered material such as single-crystal silicon, Tsai and Mecholsky⁸¹ found that the resulting fracture surfaces were not smooth, but had a fractal-like character. Mecholsky et al.⁸⁰ reported that fracture surfaces of ceramic materials also exhibit fractal-like characteristics from investigations of alumina and glass ceramic fracture surfaces. Such surfaces indicate that a dynamic process is at work in determining the path that fracture follows in brittle materials.

Because the description of fracture surfaces as being fractal-like implies that fracture surfaces may have detail to nearly the atomic scale, such a description may provide a link between macroscopic measurements and microscopic or atomic scale behavior. Thus, the finding that fracture surfaces have a fractal-like character opens new avenues for study into brittle fracture.

Mecholsky et al.⁸² reported a relationship between the toughness of a material and the measured fractal dimension of a fracture surface of that material. They found that

the toughness was related to the fractional part of the fractal dimension by the relation $K_{IC} = E\sqrt{a_0 D^*}$ where K_{IC} is the fracture toughness, E is the Young's modulus, D^* is the fractional part of the fractal dimension, and a_0 is a constant with units of length, which may be representative of some characteristic length in the material or of the process zone during fracture. Since surfaces with a higher fractal dimension generally appear more tortuous, an easy way to remember this relationship is the phrase, "the rougher, the tougher."

Applicability of Fractal Analyses to MD Simulated Systems

An important question that needs to be answered is the capability of modeling fractal-like structures by MD simulations. Quality fractal analysis requires a range of scale that is not readily available to MD simulations. Can one derive *any* valid results from an analysis of fracture surfaces formed in MD simulations.

Kieffer and Angell⁷² reported on the isotropic fracture of silica. Under these conditions, a bulk silica sample appeared to attain a structure reminiscent of silica aerogels. By using a box-counting technique applied to pair-correlation functions, they found the fractal dimension of such samples to be less than two.

In meetings with John J. Mecholsky and Joseph H. Simmons, we discussed what would be necessary to perform an analysis of fractal dimension on surfaces created by uniaxial fracture. Mecholsky used a slit-island technique that is essentially a box-counting applied to a surface on real fracture surfaces. We looked at Kieffer's paper as

a model to see how a fractal analysis might be accomplished on the fracture surface created by an MD simulation. Kieffer's method viewed the fractured silica as a mass fractal, whereas the method used by Mecholsky examined surface fractal characteristics.

In a mass fractal analysis, an object may have a dimension ranging from three, corresponding to a continuous three-dimensional network solid, through two, corresponding to a layer structure, to one, corresponding to a linear molecule. All samples are composed of a finite number of atoms that can be arranged in three-, two-, or one-dimensional arrays. Since scattering or pair correlation functions treat atoms as point particles, this analysis has no bias towards finding a set to be three dimensional, and the dimension found is wholly dependent on the arrangement of particles in three-, two-, or one-dimensional structures.

Clearly, this analysis was not suited for finding the surface fractal dimension of a solid as $2 + D^*$ where $0 < D^* < 1$. Such an analysis would be best performed by some kind of slit-island analysis. There are two problems associated this type of technique. The first is that it is not a simple matter to define the fracture surface in a MD system because the system is logically a system of point particles. The second is that our samples are too small to perform a fractal analysis, because samples of size on the order of tens of Angstroms and composed of units on the order of Angstroms could not have the range of scale required to perform an accurate analysis of fractal dimension. Thus, although a slit-island analysis could be performed in an MD system, it might not give an accurate representation of the true fractal character of the surface.

Y.L. Tsai et al.⁵⁷ recently conducted a molecular dynamics study of the fracture of single crystal silicon on the atomic scale. This system was chosen because of previous measurements of the fractal dimension on fracture surfaces of this material using a scanning tunneling microscope. Also, this system had already been simulated using molecular dynamics, and the potential function (Stillinger-Weber) was similar to one that was already written into code (Feuston-Garofalini). The authors were successful in performing a slit-island analysis of a fracture surface simulated by MD, and were able to calculate a fractal dimension, although the range of measurement on which this dimension was based was necessarily limited.

The technique used by Tsai differs from the technique used by Kieffer in an important respect. Tsai's method is dependent on the space occupied by the constituent atoms of a material, while Kieffer's method is dependent only on the spatial distribution of atom centers. Tsai assumes that the constituent atoms can be described as spheres of a convenient radius while Kieffer assumes that the constituent atoms are point particles. This difference in approach is due to the difference between surface and mass fractals. An important effect that results from this difference is that the method that used by Tsai is dependent on the shape of the space chosen to envelope the atom center, or simply, the shape of the atom. Since atoms do not have unambiguous shapes, the possible effects of the shape chosen on the dimension measured is worrisome. On the other hand, the creation of a surface by carefully chosen atom shapes may compare well to the surface that may be measured by a scanning tunneling microscope or an atomic force microscope if such techniques were truly capable of single atom resolution. A fractal dimension

obtained by this technique would then be comparable to one obtained from a microscopic analysis on real fracture surfaces. Results of that study show a strong correlation between fractal dimensions and surface roughness calculated from the MD simulations and those calculated from experiments for 100, 110, and 111 surfaces.

Because of the problems associated with finding the fractal dimension of a fracture surface created by MD simulations of fracture, we will not report any such analysis in this work. We will, however, try to relate the atomic processes we observe to possible generating functions that may result in the formation of fracture surfaces having a fractal-like character.

CHAPTER 3 PROCEDURE

Using Molecular Dynamics to Model Fracture

In this work, we conduct a series of simulations of brittle fracture in a simple "model" material for which a wealth of experimental measurements is available. Although limitations of the modeled interatomic potentials and the spatial and temporal extent of the simulated systems make it impossible to supply an exact match of the experimental strength of the material or to calculate exact crack growth velocities, the simulations were performed to investigate the underlying mechanisms for the trends observed in fracture.

One of the biggest challenges in modeling fracture on the atomic scale in real materials, and especially in glasses, is sorting out all the interacting processes that occur during fracture. Logically, a material may be treated as a large system of interacting particles. The dynamics of such a system are difficult to predict, and the cause and effect relationships are difficult to describe analytically. Often the symmetry of such systems can simplify the analysis, but this approach can not been applied to problems of fracture where the order of systems is broken. In some cases, the modeling of fracture in symmetric systems can be treated analytically, as in modeling cleavage fracture where the system symmetry is dominant over the system dynamics. When a system has little

structural order at the outset, as in the case of a glass, an analytic treatment fails, and a numerical treatment must be used.

Authors who present results from MD simulations often try to directly relate their results to experimentally obtained results. An example of this is the direct comparison of the system pressure as a function strain in MD systems to stress-strain curves of real materials undergoing fracture. However, molecular dynamics gives a perspective of materials fracture on a microscopic scale that cannot be directly compared to materials fracture on a macroscopic scale. Therefore, the results of MD simulations are best used to build an understanding of the processes that occur on the microscopic scale. With an understanding of microscopic fracture processes and how such microscopic processes might effect fracture on the macroscopic, one may be able to predict what the macroscopic experimentally observed behavior will be, possibly to explain previously unexplainable behaviors. It is not reasonable to expect that MD simulations will give results which will directly relate to the macroscopic.

The potential function gives the simulated material its molecular identity. Boundary conditions, system size, system density (for constant volume simulations), and temperature serve to describe the equilibrium state of a system. In non-equilibrium molecular dynamics, the path by which the structure is derived is also significant, and needs to be studied. The study of fracture using MD then breaks down into a simulation of the sample structure followed by the simulation of strain application and examination of the resulting processes.

Potential Functions

Modeling of physical systems is possible because many of the interactions within a physical system can be ignored and fairly accurate predictions can still be made about certain aspects of the system. Molecular dynamics modeling is possible in our systems, for example, because the collective behavior of a large group of atoms is relatively independent of the motion of electrons about individual atoms. In an MD system, the processes that one intends to model are atomic motions that are controlled by interatomic potential functions. Because MD approximates electronic bonding structure with interatomic potentials and ignores electronic states, it cannot be applied to study the formation of electronic defects in materials, but it has shown great success in studies of multiple particle dynamics.

Although the fracture of a bond begins with a restructuring of the electronic configurations forming the bond, the role of nearest neighbors becomes more significant as the bond is stretched and, as will be shown, dominates the bond fracture process. The complications caused by environmental species on bonding are eliminated by examining fracture in a vacuum. In this case, again as will be shown later, MD calculations yield a bond fracture process similar to the molecular orbital models proposed by West and Hench.³¹ The MD simulations further benefit from the ability to examine properly the effect of the broken bond on the behavior of the ensemble of neighboring atoms. A problem not examined here is that of environmentally driven fracture, because of the major role played by the chemical interaction of environmental species (H^+ and OH^- in water) on the strained bond. In this latter case, ab-initio approaches that examine the

details of the electronic configurations of the bond are essential, as shown by West and Hench.³²

It is recognized that the forces between atoms are the result of the interaction of electrons about the individual atoms, however, good results can be obtained by assuming that the electrons are in some sort of stationary configuration, and that interatomic forces can be modeled from some pseudo-potential. Systems of atoms with spherically symmetric electron configurations are well modeled by a two-body potential, which represents purely ionic character. Systems of atoms with non-spherically symmetric electron configurations are better modeled by a three-body potential. A three body potential that models a covalent-like electron configuration thus attempts to model a covalent system.

In the case of silica, the potential functions that are commonly used either model silica as a purely ionic system (Woodcock), a pseudo-ionic system (Soules), an ionic system with a pseudo-covalent character (Feuston-Garofalini), or a pseudo ionic-covalent system (Vessal). All these potential functions have limitations.

For our simulations of fracture, we have picked two potential functions that have demonstrated good fits to various pieces of experimental data for silica, and yet are quite simple. These are the truncated Born-Mayer-Huggins potential developed by Soules⁸³ and the empirical three-body potential for vitreous silica developed by Feuston and Garofalini⁸⁴ that includes an angularly dependent term. The Soules potential is purely pseudo-ionic in nature, while the Feuston-Garofalini potential incorporates a pseudo-covalent nature.

The Born-Mayer-Huggins Potential

The basis of both functions is the Born-Mayer-Huggins potential. This potential function has the form

$$\phi_{2uv}(r) = \frac{q_u q_v}{r} + \beta_{uv} b \cdot \exp\left(\frac{(\sigma_u + \sigma_v) - r}{\rho}\right) + C_{uv} r^{-6} + D_{uv} r^{-8},$$

where u, v signify atom types,

ϕ_{uv} is the potential between atoms of type u and v as a function of r ,

r is the separation distance between atomic centers,

q_u, q_v are charges on atoms of types u and v respectively,

σ_u, σ_v are radius repulsive parameters,

b is a positive constant,

ρ is a hardness parameter,

C_{uv}, D_{uv} are the coefficients of dipole - induced dipole and dipole - induced quadrupole terms, respectively,

β_{uv} is the Pauling coefficient, given by

$$\beta_{uv} = \left(1 + \frac{Z_u}{n_u} + \frac{Z_v}{n_v}\right),$$

where Z_u, Z_v are the units of charge of type u and v , respectively, and

n_u, n_v are the numbers of valence electrons of u and v , respectively.

The multipole terms become important when the atoms are highly polarizable and are separated by small distances, but are generally neglected in the simulation of silica glass.

Some have questioned the accuracy of this simplification since oxygen exhibits a high

degree of polarization and the atoms are closely spaced in condensed phases. The justification for ignoring these terms is that atoms within a solid are generally constrained to the point that these terms would have minimal effect, and these terms involve many-body interactions that are computationally difficult. When the multipole terms are neglected, the potential function simplifies to

$$\phi_{2uv}(r) = \beta_{uv} b \cdot \exp\left(\frac{(\sigma_u + \sigma_v) - r}{\rho}\right) + \frac{q_u q_v}{r}.$$

By collecting terms, this becomes

$$\phi_{2uv}(r) = A_{uv} \cdot \exp\left(-\frac{r}{\rho}\right) + \frac{q_u q_v}{r},$$

where

$$A_{uv} = \beta_{uv} b \cdot \exp\left(\frac{\sigma_u + \sigma_v}{\rho}\right).$$

From here, the Soules and the Feuston-Garofalini potential functions take divergent forms.

Truncation or Screening Functions

In a simulation, it is desirable to have a potential of limited range in order to minimize the number of particle interactions. However, the Coulombic portion of the Born-Mayer-Huggins potential approaches zero slowly as the reciprocal of distance and many neighbors would be required for calculations of all potentially significant interactions. To overcome this problem, a screening or truncation function is used to

limit these interactions. This truncation process simulates the result of a lattice of alternating charges as used in the calculation of a Madelung constant.

One method of dealing with the slowly convergent Coulomb potential is to perform an Ewald sum.⁵⁵ If one knows the symmetry of a crystal, the electrostatic potential of ions in the crystal can be more quickly summed by performing the sum in Fourier space. This is the basis of the Ewald sum approach. From the Ewald sum, a screening factor is derived that breaks up the Coulombic part of the potential into a local part that is summed over individual ions, and thus contributes to inter-particle forces, and a background part that is just added to the overall potential energy and has no effect on inter-particle forces. Strictly speaking, the results of an Ewald summation are only valid for the crystal system for which they were derived, however, the functional form of the screening factor is useful even when the inverse lattice sum has not been performed for a particular system. Thus, the Ewald convergence parameter may be used in the summation of the system potential energy using the modified Born-Mayer-Huggins potential function

$$\phi_{uv}(r) = A_{uv} \cdot \exp\left(-\frac{r}{\rho}\right) + \frac{q_u q_v}{r} \cdot \operatorname{erfc}\left(\frac{r}{\epsilon L}\right),$$

where $\operatorname{erfc}()$ is the error function complement function,

ϵ is a constant, typically 0.175 - 0.35,⁶⁰ and

L is a linear dimension of the molecular dynamics cell or r_{max} .

Table 3-1
Parameters Used in the Soules Force and Potential Functions

Potential Function Parameters

$$\rho = 0.290023 \text{ \AA}$$

$$A_{\text{Si-Si}} = 3300 \text{ p ergs}$$

$$A_{\text{Si-O}} = 3000 \text{ p ergs}$$

$$A_{\text{O-O}} = 2300 \text{ p ergs}$$

$$q_{\text{Si}} = +4e$$

$$q_{\text{O}} = -2e$$

where e is the electron charge

Truncation Function Parameters

$$r_{\text{max}} = 5.5 \text{ \AA}$$

$$n = 3$$

The term ϵL is termed the convergence parameter. It is dependent on an arbitrarily chosen constant and the size of the molecular dynamics cell, but it is independent of the type of interaction.

The Soules Potential Function

The Soules force function has been shown to simulate vitreous silica structures with approximately the correct density and with nearest neighbor distances in significant agreement with neutron diffraction data. It is the product of the force function derived from the Born-Mayer-Huggins potential and an empirical truncation function. A direct differentiation of the Born-Mayer-Huggins potential gives

$$F_{\text{BMH},uv}(r) = -\frac{d\phi_{2uv}}{dr} = \left[\frac{A_{uv}}{\rho} \cdot \exp\left(-\frac{r}{\rho}\right) + \frac{q_u q_v}{r^2} \right]$$

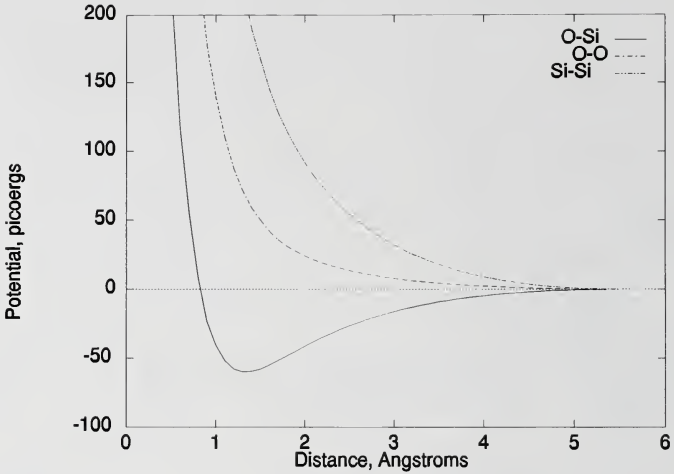


Figure 3-1. Plot of the Soules potential function for various interactions.

The truncation factor has the form $T(r) = \left[1 - \left(\frac{r}{r_{\max}}\right)^n\right]$. The Soules force function is

then

$$\begin{aligned}
 F_{\text{Soules},uv}(r) &= -F_{\text{BMH},uv}(r) \cdot T(r) \\
 &= \frac{1}{r} \left[\frac{A_{uv}}{\rho} \cdot \exp\left(-\frac{r}{\rho}\right) + \frac{q_u q_v}{r^2} \right] \cdot \left[1 - \left(\frac{1}{r_{\max}}\right)^n \right].
 \end{aligned}$$

The potential function that corresponds to the Soules truncated Born-Mayer-Huggins force function is

$$\begin{aligned}\phi_{\text{Soules},2uv}(r) &= - \int_r^{\infty} F_{\text{Soules},2uv}(r) dr \\ &= - \int_r^{\infty} \left[\frac{A_{uv}}{\rho} \cdot \exp\left(-\frac{r}{\rho}\right) + \frac{q_u q_v}{r^2} \right] \cdot \left[1 - \left(\frac{r}{r_{\max}}\right)^n \right] dr ,\end{aligned}$$

which is not analytically integrable. Thus, the potential energy of the system is calculated using a numeric integration of this expression. The parameters used in the Soules force function are given in Table 3-1. A plot of the Soules potential function is given in figure 3-1.

The Feuston-Garofalini Potential Function

The three-body potential developed by Feuston and Garofalini is a sum of the modified Born-Mayer-Huggins potential an empirical convergence parameter and the three-body portion of the Stillinger-Weber potential.⁴⁹ The two-body portion of the potential is

$$\phi_{2uv}(r_{ij}) = A_{uv} \cdot \exp\left(-\frac{r_{ij}}{\rho}\right) + \frac{q_u q_v}{r_{ij}} \cdot \operatorname{erfc}\left(\frac{r_{ij}}{\beta_{uv}}\right).$$

Notice that the ϵL term of the convergence parameter has been replaced by β_{ij} . This makes the screening function independent of cell size, but dependent on the type of

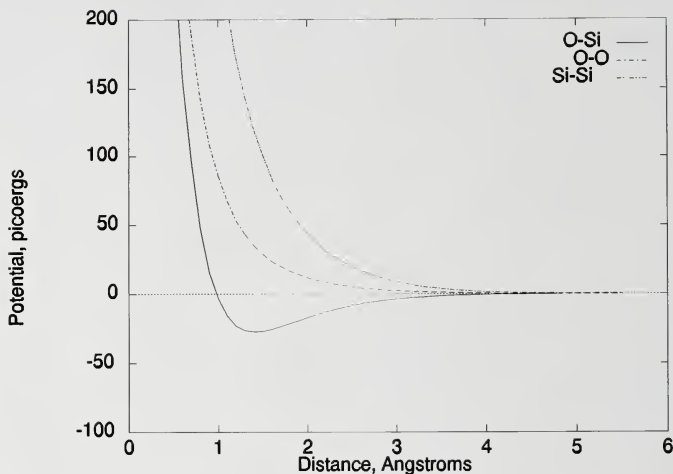


Figure 3-2. Plot of the two-body portion of the Feuston-Garofalini potential function for various interactions.

interaction, and adds another set of adjustable parameters. The three body portion of the potential is

$$\phi_{\theta uvw}(r_{ij}, r_{jk}, \theta_{ijk}) = \begin{cases} \lambda_{uvw} \exp \left[\frac{\gamma_{uvw}}{(r_{ij} - r_{uvw}^c)} + \frac{\gamma_{uvw}}{(r_{jk} - r_{uvw}^c)} \right] (\cos \theta_{ijk} - \cos \theta_{uvw}^c)^2, & r_{ij} < r_{uvw}^c \wedge r_{jk} < r_{uvw}^c \\ 0, & r_{ij} \geq r_{uvw}^c \vee r_{jk} \geq r_{uvw}^c \end{cases}$$

The parameters used in this potential function are given in Table 3-2 and a plot of the two-body portion of this potential is given in figure 3-2. This shows a shallower

Table 3-2
Parameters used in the Feuston-Garofalini Potential Function

Two-body Potential Parameters

$$\begin{aligned}\rho &= 0.290023 \text{ \AA} \\ A_{\text{Si-Si}} &= 1880 \text{ p ergs} \\ A_{\text{Si-O}} &= 2960 \text{ p ergs} \\ A_{\text{O-O}} &= 720 \text{ p ergs} \\ q_{\text{Si}} &= +4e \\ q_{\text{O}} &= -2e\end{aligned}$$

where e is the electron charge

$$\begin{aligned}\beta_{\text{Si-Si}} &= 2.29 \\ \beta_{\text{Si-O}} &= 2.6 \\ \beta_{\text{O-O}} &= 2.34\end{aligned}$$

Nonzero Three-body Potential Parameters

$$\begin{aligned}\lambda_{\text{O-Si-O}} &= 180 \text{ p ergs} \\ \lambda_{\text{Si-O-Si}} &= 3 \text{ p ergs} \\ \gamma_{\text{O-Si-O}} &= 2.6 \text{ \AA} \\ \gamma_{\text{Si-O-Si}} &= 2.0 \text{ \AA} \\ r_{\text{O-Si-O}}^c &= 3.0 \text{ \AA} \\ r_{\text{Si-O-Si}}^c &= 2.6 \text{ \AA} \\ \cos \theta_{\text{O-Si-O}}^c &= -1/3 \\ \cos \theta_{\text{Si-O-Si}}^c &= -1/3\end{aligned}$$

potential well in the Si-O interaction and a weaker repulsion in the Si-Si and O-O interactions than is obtained for the Soules potential.

Simulation Techniques

Integration Algorithms

Molecular dynamics is a computationally intensive technique in which the simultaneous integration of the motion of many individual particles is performed over short time steps.

Integration of functions may be performed in many different ways, but only a couple of different techniques are commonly used when integrating the equations of motion of a molecular dynamics system because they are well known to provide reasonably good accuracy with a minimum amount of computation. These are the Verlet "leapfrog" algorithm and the Gear Predictor-Corrector algorithm.

Verlet algorithm

Our simulations generally made use the Verlet algorithm,⁸⁵ given by the vector equation

$$r_{i,t+\Delta t} = 2 \cdot r_{i,t} - r_{i,t-\Delta t} + \frac{2 \cdot \Delta t^2}{m_i} \cdot \left[\sum_{j \neq i} F_{ij} + \sum_{(j \neq k) \neq i} F_{ijk} \right],$$

where

$r_{i,t+\Delta t}$ is the position of the particle after the time step,

$r_{i,t}$ is the position of the particle before the time step,

$r_{i,t-\Delta t}$ is the position of the particle before the last time step,

t is a particular time,

Δt is the length of a time step,

m is the mass of the particle,

$\sum F_{ij}$ is the sum of all two-body force components on the particle.

$\sum F_{ijk}$ is the sum of all three-body force components on the particle,

where applicable.

Fifth-order Gear predictor-corrector algorithm

The fifth-order Gear predictor-corrector algorithm, as encoded by J.M. Haile,⁸⁶ was also tested. This was done to verify that the Verlet algorithm, known for its speed and stability, but not for its overall precision, gives reasonable results as compared to the slower but more precise Gear algorithm.

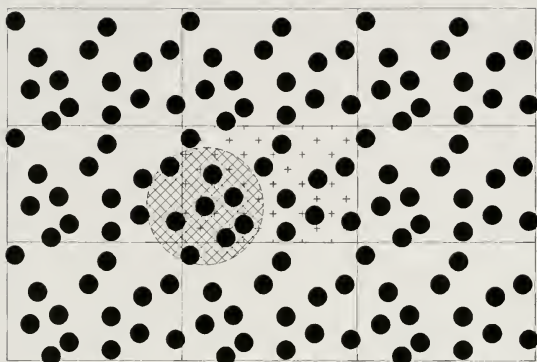
The Time Step

The time step is the basic unit of time in a molecular dynamics simulation. The time step is an approximation for an infinitesimal amount of time that is valid for the processes under observation. During this fundamental time step, in the Verlet algorithm, the acceleration is assumed constant. In the Gear predictor-corrector method, approximations are developed that move the constant function to a higher order time derivative. In the selection of the fundamental time-step, it is desirable to use a value short enough to maintain a constant system energy, yet a value long enough to observe a physically significant process. The usual test for deciding if a time step is of sufficiently short length is to perform a simulation over about a thousand steps and check to see if the system energy remains fairly constant. If not, then the time step is too long. A time step of 0.5×10^{-15} s was found to be of acceptable length, and was used in these simulations. This corresponds to about 1/40 of an atomic vibration period.

Limiting Particle Interactions

The magnitude of the task of calculating particle interactions is reduced by limiting the spatial extent over which these interactions are considered. Neighbors lists for all particles that include all neighbors which may possibly interact with a central particle are compiled. Only these neighbors are then considered when calculating interactions with the central particle. The neighbors lists are updated periodically by finding all particles within a distance given by the maximum interaction distance plus the maximum distance a particle may travel during the period between updates. The period between updates in these simulations is ten time-steps. The maximum distance, found by Ochoa,⁸⁷ that a particle may move in a solid in ten time steps at 0.5×10^{-15} s each is 0.5 \AA . Thus, the maximum distance for inclusion in a neighbors list from the central atom is 0.5 \AA greater than the cutoff distance for interaction between particles, or 6.0 \AA in the case of a interaction cutoff at 5.5 \AA .

The Pythagorean theorem is used to find the squares of inter-particle distances. Finding inter-particle distances requires square root operations that are computationally time consuming, and are avoided. The force table is tabulated in terms of the square of inter-particle distances, so inter-particle distances are required only when pair correlation functions or bond angle distribution functions are accumulated.



Primary cell



Repeated secondary cells



Neighborhood about atom

Figure 3-3. The effect of periodic boundary conditions in a simulated system. Note that the neighborhood of an atom may extend beyond the primary cell.

Application of Periodic Boundary Conditions

The use of periodic boundary conditions allows one to model a bulk-like material with a limited number of particles. A schematic showing the effect of periodic boundary conditions is presented in figure 2-3.

Periodic boundary conditions are applied to the simulated system when finding inter-particle distances. If the difference in any coordinate is greater than one-half the corresponding dimension of the cell, then the corresponding image of the particle located in an adjacent cell will be closer to the central particle than the particle in the primary cell. The difference in the coordinate is then adjusted to reflect this by either adding or subtracting the corresponding dimension of the cell to minimize the absolute values of the difference. It is the resulting difference that is used in the Pythagorean relation to find the square of the distance between the particles. The algorithm by which this is performed is as follows: The differences in coordinates are calculated from

$$d_{uij} = x_{ui} - x_{uj},$$

and are subsequently adjusted with

$$d'_{uij} = d_{uij} - s_u \cdot \text{round}\left(\frac{d_{uij}}{s_u}\right),$$

and used in the Pythagorean relation

$$r_{ij}^2 = \sum_{u=1}^3 d'_{uij}{}^2$$

where $u = 1, 2, 3$ denote the Cartesian dimensions of space,

x_{ui} is the u Cartesian coordinate of atom i ,

x_{uj} is the u Cartesian coordinate of atom j ,

d_{uij} is the u coordinate difference between atoms i and j ,

d'_{uij} is the u coordinate difference between atoms i and j after correction
for periodic boundary conditions,

s_u is the u dimension of the cell,

$\text{round}(x)$ is a function that returns the integer nearest to its argument, x ,
and

r_{ij} is the distance between atoms i and j .

The application of periodic boundary conditions gets more difficult when the cell is sheared. Suppose that one puts the cell oriented with the coordinate axes into simple shear as shown in figure 2-3. The opposite sides of the cell are shifted with respect to each other. This must be taken into account when applying periodic boundary conditions across the shifted faces. The periodic boundary condition equations are

$$c_u = \text{round}\left(\frac{d_{uij}}{s_u}\right)$$

$$d'_{uij} = d_{uij} - \tau_{uv}(s_v c_v) - \tau_{uw}(s_w c_w)$$

$$d''_{uij} = d'_{uij} - s_u \cdot \text{round}\left(\frac{d'_{uij}}{s_u}\right)$$

$$r_{ij}^2 = \sum_{u=1}^3 d''_{uij}^2$$

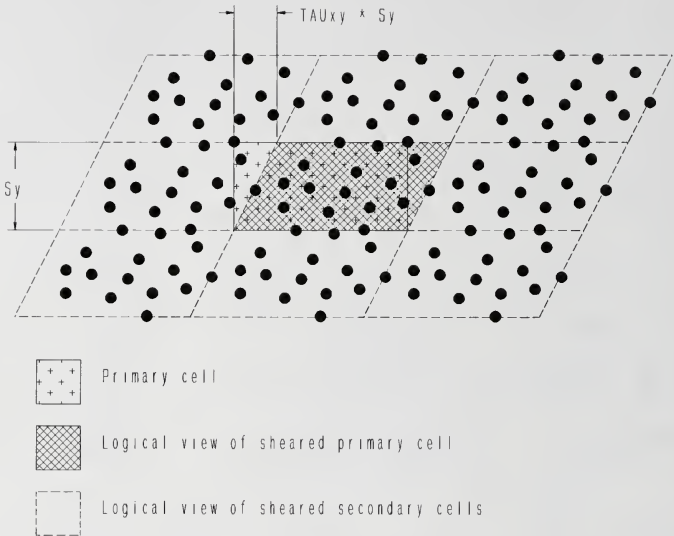


Figure 3-4. Schematic showing the application of periodic boundary conditions to a system under shear strain.

By this method, full periodic boundary conditions are maintained even when the virtual shape of the cell changes.

Handling Particle Interactions

Interactions between particles are handled by the following process--interaction geometries are found, interaction forces are found, components of interaction forces are

summed on all participating particles, and particle positions are updated to reflect the effect of interactions.

In the case of two-body potentials, the interaction geometry is simply the square of the distance between pairs of central atoms and neighbors. The interaction force is found from the force table, which is subsequently broken into components and summed on each particle.

When the three-body component of the force function is applied, the interaction geometry becomes the distances between the central atom and two of its coordinating neighbors of a certain type, and the angle between the two "bonds." Since the number of interaction variables is large, but the actual number of interactions is rather small, a force table for a three body potential would be difficult to compile, but fortunately, is not required. The force is calculated for all three body interactions as they are needed, and components are summed on each interacting particle.

As a particle moves, it may leave the primary cell. When this occurs, the particle is translated back into the primary cell by subtracting the appropriate cell dimension and adjusting for shear, as required. Thus particles that leave through one side of the cell reappear through the opposite side of the cell, perhaps shifted if the cell has undergone shear. This allows one to control the dimensions of the cell while permitting the atoms to move as their environments dictate.

Observing the System

As a simulation progresses, one can collect information to find out what the system is doing. Any aspect of a simulation can be recorded. A few that are commonly recorded are instantaneous or average thermodynamic properties, particle positions and velocities, pair correlation functions, and bond angle distribution functions.

System thermodynamics

Thermodynamic properties, such as system temperature, energy, and pressure are calculated. A running average of these values may be kept, so that outputs of either instantaneous thermodynamic properties or average properties may be made.

The temperature of the system can be found by assuming that the system behaves as a classical statistical system, with average particle kinetic energies given by the equipartition theorem, $E_k = \frac{3}{2}k_B T$. The temperature can then be adjusted by scaling the velocities of all particles to give the proper average kinetic energy.

The system pressure or stress tensor is calculated using the Virial of Clausius, which has the form

$$P = \frac{1}{V} \left(Nk_B T - \frac{1}{3} \sum_{i=1}^{N-1} \sum_{j>i}^N \left[r_{ij} \cdot \nabla \Phi(r_{ij}) \right] \right)$$

When converted for use in simulations, it takes the form

$$P_{mn} = \frac{10^3}{3V} \cdot \sum_{i=1}^N \left(m_i v_{i,m} v_{i,n} + \sum_{j>i}^N r_{ij,m} F_{ij,n} \right),$$

where P is the system pressure in kbar,
 V is the volume of the cell in \AA^3 ,
 v_i is the velocity of particle i in $\text{\AA}/10^{-14}$ s,
 F_{ij} is the interatomic force between atoms i and j in 10^{-12} erg/ \AA ,
 r_{ij} is the interatomic separation between atoms i and j in \AA ,
 m_i is the mass of particle i in 10^{-24} g.

The potential energy for a system is calculated in a manner similar to the calculation of forces on individual particles. When the neighbors lists are updated, interaction potentials are found using the potential energy table. The potential energies for all interactions are then summed to find the potential energy for the system. The system potential energy is added to the system kinetic energy as previously obtained to find the system internal energy.

System structure

Particle positions are saved periodically to be analyzed later. These positions may be used to view the structure of the system, perform ring statistics, or investigate regions of high or low local density.

Pair correlation function distributions for each type of interaction are accumulated when updating neighbors lists. This is done by incrementing arrays representing each type of interaction and each segment of distance every time a pair with some separation is found. The accumulated data is converted to a normalized pair distribution function using

$$G_{uv}(r) = \frac{2 V n_{uv}(r)}{4 \pi r^2 \Delta r N_{uv}},$$

- where $G_{uv}(r)$ is the pair correlation function for types u and v ,
 r is the separation distance,
 Δr is the resolution of the distribution,
 V is the volume of the cell,
 n_{uv} is the number of u - v pairs found between the distances r and Δr from
the central atom,
 N_{uv} is the number of possible u - v pairs in accumulation,
 $N_{uv} = m N_u N_v$
- where m is the number of accumulations,
 N_u is the number of atoms of type u ,
 N_v is the number of atoms of type v ,
- and $4\pi r \Delta r$ is recognized as the volume of a spherical shell in which a non-
central atom may be located about the central atom.

Bond angle distributions are calculated by finding the coordinating neighbor atoms during updates of the neighbors lists, then applying the definition of a dot product to find bond angles between central atoms and these neighbors. The formula for doing this is

$$\theta_{jk} = \arccos\left(\frac{x_{ij}x_{jk} + y_{ij}y_{jk} + z_{ij}z_{jk}}{r_{ij}r_{jk}}\right),$$

- where θ_{jk} is the bond angle,
 j denotes the apex atom,

i, k denote the end atoms,

x_{ij}, y_{ij}, z_{ij} are the vector components between atoms i and j ,

x_{jk}, y_{jk}, z_{jk} are the vector components between atoms j and k , and

r_{ij}, r_{jk} are the distances between atoms i and j , and j and k , respectively.

The accumulated distribution is then normalized by dividing the number of counts at each bond angle by the total number of counts, that is, the total number of bond angles found. This is contrasted to another bond-angle distribution technique that divides the number of counts at a particular bond-angle interval by the cosine of the angle in order to normalize to the area of the annular ring on a sphere represented by the bond-angle interval. Our technique finds a bond angle distribution as would be derived from X-ray diffraction data, while the latter technique would show structural predominances towards a particular bond angle, since it removes the predominances that would result from totally random configuration of coordinating atoms about a central atom.

Force Distributions

A segment of code was added to the simulation program to make distributions of the forces experienced by particles during simulations of fractures at different strain rates. This was done in order to verify that variations in strain rate dependence in fracture simulations were the result of complicated rearrangements in the structure rather than the inability of the atom in the system to remain in local equilibrium during the application of strain at high strain rates. The principle involved is that when particles fall out of local equilibrium, they undergo greater forces, so that the force distribution,

defined as the number of particles under a certain range of applied forces, should broaden.

Damped Motion Molecular Dynamics

A modification was made to the molecular dynamics program to apply critical damping to the motion of particles during an MD simulation. This was done to provide verification of the results found by the force distribution study as mentioned above. The results are similar, but are different in an important respect. In this type of simulation, thermal vibrations are damped out, but particles are free to move to their equilibrium positions, albeit with some damping. Thus, the role of thermal vibrations is studied directly.

Modification of the MD program was made by simply scaling the atom velocities at each time step. Critical damping was applied by choosing a scaling factor that would damp the velocity involved in a thermal vibration by a factor of $1/e$ in one thermal vibration period. The scaling of velocities was applied within the Verlet or Gear algorithms, as applicable.

Assigning Initial Velocities

Velocities must be assigned to atoms at the start of a simulation when there is no pre-existing velocity data present. This is done by giving atoms random velocities conforming to a Maxwell velocity distribution. Such a distribution is created using

Gaussian deviates, scaled by a factor to give the proper average temperature. The equations that are used to assign velocities in a three-dimensional system are⁸⁸

$$v_{x,i} = \sqrt{-\frac{2k_B T}{m_i} \cdot \ln(R_1) \cdot \cos(2\pi \cdot R_3)}$$

$$v_{y,i} = \sqrt{-\frac{2k_B T}{m_i} \cdot \ln(R_1) \cdot \sin(2\pi \cdot R_3)}$$

$$v_{z,i} = \sqrt{-\frac{2k_B T}{m_i} \cdot \ln(R_2) \cdot \sin(2\pi \cdot R_4)}$$

where $v_{x,i}$, $v_{y,i}$, $v_{z,i}$ are the components of the velocity of particle i ,
 R_1 , R_2 , R_3 , R_4 are random numbers evenly distributed between 0 and 1,
 m_i is the mass of particle i ,
 T is the temperature corresponding to the velocity distribution, and
 k_B is Boltzmann's constant.

Analytical Techniques

We now discuss some of the auxiliary techniques developed for examining the output from simulations.

Graphic Representations

Graphic representations of structures provide an insight into processes that occur on the atomic scale. If one desires to perform an experiment where one wishes to study something more than the thermodynamics of a system, having graphic representations of the simulated structure is indispensable. We have developed a technique with which a 3-D animation of the particles can be performed. Three-dimensional imaging is achieved through the use of stereo pairs and an appropriate viewer, and has the advantage that one can see the presence of voids or other structural features in three dimensional images that are not visible in a two dimensional projection. This technique allows visualization of all aspects of particle motion in an admittedly small system. An important feature of this technique is that it runs fast enough on our Apollo DN10000 computer to allow viewing of the evolution of a system in reasonably smooth animation, either forward or backwards. This allows one to trace events noted in later parts of a simulation back to their beginnings. The technique, based on a program originally written by Greg O'Rear, also permits one to zoom in on particular events, display coordination information of single atoms, and find the lengths of particular bonds.

Free Volume Sphere Analysis

In this work we have found that the change of "free volume" in the simulated material reflects an important aspect of the expansion-to-failure process. Therefore, we have developed a method for the analysis of "free volume spheres." This analysis gives the positions of holes within a structure and a distribution of hole sizes. The method is

performed by taking combinations of four atoms within the structure that define spheres, and testing to see if the defined spheres contains any other atoms. If a sphere does not contain any other atoms, it is termed a free volume sphere. More specifically, one may realize that the number of combinations of four atoms in a structure containing atom structure is huge,

$$\frac{1152!}{4! \cdot 1148!} = 7.3 \times 10^{10}.$$

This is not a feasible calculation. However, the magnitude of the calculation can be reduced by limiting all the possible combinations involving an atom to lie within a radius of 11 Å of that atom. This sets a limit on the maximum free volume sphere size that can be found because the diameter of the sphere must be less than or equal to the cutoff distance. However, since there generally is a maximum on the size of the free volume spheres found, the accuracy of the method is not reduced, so long as the cutoff distance is greater than the diameter of the largest sphere. For this calculation, assuming a maximum of 300 neighbors in a sample size of 1080 atoms, there are about 3.03×10^8 possible combinations. This is a feasible calculation on our machine.

One problem with the technique as described is that the same hole may be counted many different times as smaller holes on the edge of the larger holes. In an attempt to eliminate this, another requirement that not all the defining atoms may lie in a given hemisphere of the sphere was included. This reduced the number of spheres found by more than half and improved the accuracy of the distribution obtained, but with the

drawback in that spheres can more easily come into and go out of existence during simulations, making it difficult to track holes during fracture simulations.

Ring Statistics

Ring statistics analyses were performed. Since vitreous silica has no long-range structure, and even intermediate-range structure is difficult to characterize, researchers try to characterize structures in terms that are meaningful and can be determined algorithmically. One such measure of intermediate structure is ring statistics, where ring size distributions are presented.

There is some ambiguity in the literature on how rings should be defined as is evidenced by differences in definitions put forth by Goetzke and Klein,⁸⁹ and Mariani and Hobbs,¹⁷ and apparently many different algorithms for finding rings. Thus some discussion of our definition and algorithm is warranted.

We used an independently developed ring statistics algorithm to find rings. The algorithm works as follows. Consider a vertex in a structure linked to n other vertices.

It can then be incorporated into rings $\frac{n(n-1)}{2}$ different ways (combinations of 2 in n),

that is, a ring may be found passing through the central vertex and any combination of two adjoining vertices. Our algorithm works from the central vertex and finds the shortest ring that completes the circuit through each pair of adjoining vertices.

Unfortunately, it is not enough to find rings, we must also count them. Inevitably, a ring found by this method will be duplicated when a search for rings is

performed about one of the other vertices contained in the ring. Then an n -membered ring may be counted n times. A quick fix to the problem would be to divide the number of n -membered rings by n to get the actual number of n -membered rings. However, this does not work either, since the shortest ring passing through a triplet of vertices found when starting at one vertex may not be the shortest ring found passing through the triplet of vertices when starting at the center of the triplet. Thus, each n -membered ring is not necessarily counted n times.

In order to solve counting problems, all rings are catalogued as they are found, so that only the unique rings are counted.

Unfortunately, this technique is not completely compatible with counting techniques recently described by Goetzke and Klein. Our technique finds rings that are most similar to the non-decomposable strong rings that they describe.

The difference in counting results from the requirement that all combinations of adjacent vertices must contain a ring. This is not always true for strong or primitive rings. Chemically speaking, our ring finding technique might be more appropriate, since it finds all the rings to which an atom may belong. From a network counting standpoint, the Goetzke-Klein technique is better. That is, our technique finds all of the smallest rings that may influence the local chemical environment of an atom, while the Goetzke-Klein technique finds the rings that one would use in a description of network topology.

Structural Defects

The bonding defects listed are derived from the ring statistics program, which finds rings by finding nodes (silicon atoms) and bridges between those nodes (oxygen atoms). The defect information is then more applicable to the network structure than the chemical state of atoms, as coordination of silicon atoms by oxygen atoms is not given directly, but is rather inferred since oxygen atoms act as bridges between silicon atoms. The maximum coordination distance for the bridging oxygen atoms about silicon atoms is set to 2.0 Å.

Composition Profiles

Studies by Feuston and Garofalini⁶² have indicated that there is an abundance of oxygen atoms on empirically formed silica surfaces. We felt that a study of the abundances of species on a surface formed through a fracture simulation would add credibility to this finding. A program was written to make histograms of the number of the different types of atoms within segments of the MD cell separated by x-coordinate, so that the slices would be normal to the direction of strain and roughly parallel to the resulting fracture surface. This was done in order to see if there was a predominance of particular atom types in the slices near the fracture surfaces, and was similar to the technique used by Feuston and Garofalini.

Mechanical Properties

The moduli of the simulated samples were measured at a 0.05 ps^{-1} strain rate to a 10% expansion. Estimates of the slope of the stress versus expansion curves were made within the linear regions to find longitudinal moduli. These values were converted to Young's moduli by using the equation

$$E = \frac{(1 + \nu)(1 - 2\nu)}{(1 - \nu)} \cdot L,$$

where E is Young's modulus,

L is the longitudinal modulus,

ν is Poisson's ratio, assumed for simplicity to be 0.25.

Stress-strain curves for the simulated samples at the 0.05 ps^{-1} strain rate were compared to stress-strain curves predicted from published elastic constants in order to make comparisons of the nature of the curves.

This concludes the discussion of analytical techniques used in this work. All programs for analysis of simulation results were written in C by this author, unless otherwise noted.

Program Details

Overview

Recently it has become possible to purchase commercially available molecular dynamics simulation programs. This work was initiated before such applications became

available. Although this work did not start from scratch, as computer simulation codes originally obtained from Tom Soules and later modified by Romulo Ochoa and Rik Faith were utilized, much of the effort was involved in expanding the capabilities and optimizing the performance of this existing computer code.

The existing simulation codes did not include visualization programs. A visualization program written by Greg O'Rear gave us first glimpses of the systems that we simulated, but it was limited to providing snapshots, which did not provide insight into the dynamics involved in the evolution of the systems. In this work the graphics program was vastly expanded to provide animation and increased realism for visualization of the processes that we simulated.

Other analysis programs were also written in an attempt to make results quantifiable. Although the animated pictures provided by the visualization program clarified the processes occurring, the animation could not be placed in the literature. Thus, we attempted to present static data to support our claims made on observation of the systems.

The Structure of Computer Code

The structure used in the writing of code is dependent on the goals of the research project. Often in writing code, there is a trade-off between speed and clarity of code. In order to obtain optimal speed, one writes code with as few subroutine calls as possible. In order to improve the clarity, maintainability, and flexibility of the code, one makes liberal use of subroutines and uses a modern computer language having a more

logical syntax. The eventual form that a program takes balances these two aspects. First, let us understand why the form of the code is important in its execution and maintenance.

The primary cost in using subroutines is the overhead involved in calling a subroutine. This includes allocating computer memory for the subroutine instructions at the initiation of a subroutine call, copying data from the calling program unit to the subroutine, copying data from the subroutine back to the calling program unit, and freeing the memory used by the instructions in the subroutine at the conclusion of the execution of the subroutine. In practice, the cost of this overhead to execution time can be reduced by avoiding the use of subroutines in the deepest loops of a program, where such subroutines would be called most often.

Another cost involved in using subroutines is that optimizing compilers can only optimize within a program unit, so a program written using subroutines can only be optimized locally, whereas a program without subroutines can be optimized globally. Since optimizers work by rearranging code so that expressions are evaluated in the most convenient order for the computer, avoiding the use of subroutines that cause breaks in a program that place limitations on the order of the assignment of global variables reduces the effect of using subroutines on optimization of the program.

The primary benefit of using subroutines is clarity. By utilizing subroutines at different levels, one can obtain an overall view of how the program works by looking at a clearly written main program. Such a program may be quite short, and may serve as a sort-of table of contents for the rest of the code. Since optimal code should make

use of the symmetry involved in the problem to be calculated, such symmetry should be evident to aid one in a quick understanding of the program. From the main program, one can rapidly advance to points of interest within the code.

The maintainability of the code is increased by the use of subroutines. Bugs in the code are in general easier to find because debuggers are often capable of displaying the program unit in which an error occurred, but are less often capable of displaying the program line number on which the error occurred. Modifications are easier to make because the extent of variables in a subroutine is less than in a program not split up into subroutines, so the possibility of making inadvertent changes to an already defined variable is reduced. Finally, subroutines can be placed in separate program modules, or files, which are compiled independently and then linked to form an executable file. This increases the speed at which a program is compiled by limiting the modules that need to be recompiled whenever a change is made to the program. This is quite useful, especially when attempting to eliminate particularly persistent bugs.

The flexibility of code is also increased by the use of subroutines. Additional subroutines can be inserted into or removed from code as desired to change the functionality of the code. Subroutines may be substituted. Since a program that makes use of subroutines should provide a convenient framework for the subroutines it uses, it is easier to add code within this framework than insert it directly into code that is not broken into subroutines.

Just as subroutines are a way of grouping instructions together, data structures are a way of grouping similar types of data together. Similar pros and cons also apply to

data structures as apply to subroutines. Data structures provide convenient packages for referencing data that is somehow related, such as the display parameters for atoms in a graphics visualization program. However, the members of data structures cannot be register variables that can be referenced quickly, so the use of data structures in the deepest levels of a program may adversely affect the performance of the program.

Additional tools are often available to programmers to minimize the compromises that must be made in program design. Some compilers provide the capability for in-line functions that eliminate the overhead of normal function calls while retaining the logical simplicity of a subroutine. In-line functions work by inserting the code of the function within the code of the calling program at compile time. Unfortunately, not all compilers support in-line functions. Most compilers that operate within the UNIX programming environment support a C-preprocessor option. The C-preprocessor allows one to include or exclude certain blocks of code at compile time based on the values assigned to tokens embedded within the program. The tokens can be defined within the program itself, or can be defined in the command line when invoking the compiler. This allows one to customize the same source code for slightly different applications at compile time without having to modify the code. After running the C-preprocessor, the embedded tokens are removed so that only the customized standard language source code remains that can be ported to machines without a C-preprocessor.

The Choice of a Programming Language

Unfortunately, there is no perfect computer language. FORTRAN has traditionally been the language of choice for most scientific programmers. C is the language of choice by most systems programmers. BASIC is the language of choice for those who want a quick solution to a particular problem where high performance is not a requirement. PASCAL falls somewhere between C and FORTRAN, but its use is now generally being supplanted by C. C++ was developed as a simulation language, and is a superset of C. A short discussion of why different languages are preferable in certain instances is helpful.

Most scientific programmers work with FORTRAN because it was one of the first to cater to the needs of the scientific programmer. FORTRAN features a relatively simple syntax that provides all flexibility required to solve the equations that scientists could not solve analytically. Because of its use in "number crunching" applications and because benchmark programs are often written in FORTRAN, computer and software manufacturers generally optimize their FORTRAN compilers to create executable code with the highest throughput. As a result, FORTRAN still offers advantages over other languages. The syntax of FORTRAN up to and including FORTRAN 77 is rather antiquated, however. Because it was first used when punch cards were popular, the FORTRAN 77 syntax still limits one to 80 columns. Loop control is also rather arbitrary, as the FORTRAN standard requires a unique line number at the base of the loop. Input and output is also rather difficult and limited, as native print commands do not provide full control over the appearance of output. Thus FORTRAN is not

commonly used in control programs, or in programs where the appearance of the output is important. Finally, FORTRAN does not support the data structures required to transfer complicated data to functions that perform complicated tasks. All of these aspects result in a language that excels at number crunching, but suffers from a lack of logical simplicity when applied to more complicated tasks.

The C programming language provides much of what FORTRAN lacks, but it suffers from limitations in other respects. C provides a more logical syntax, better program control, more flexible I/O, and much more flexible data structures than FORTRAN. It provides access to low-level operations, such as bit-by-bit operations, for more efficient manipulation of binary data. It also provides means for dynamic memory allocation, which makes programs written in C more adaptive to systems of varying sizes. Thus, C is much more capable of harnessing system resources, and as a result, is often used in systems programming and in instrument control. The C programming language also provides for a command line interface, making C applications more user-friendly than FORTRAN applications. However, C has not traditionally been the language of choice for number crunching. Press et al provide a discussion of some of the shortcomings of the C programming language.⁹⁰ The original C, developed by Kernighan and Ritchie (K&R), performed all calculations in double precision, whether the extra precision was needed or not. This resulted in a severe loss in throughput on machines with processors of less than 64 bits. Some implementations of C, such as all ANSI C and some K&R C compilers, are capable of performing calculations in single precision if desired. Since C by nature is more modular than FORTRAN, programs

written in C are not globally optimized to the same degree as the type of program traditionally written in FORTRAN. Finally, the C language is meant to provide the syntax required as a framework for one's creativity, but it does not provide some of the mundane operators that scientists want to use when performing calculations, such as a raised-to-a-power operator. Thus, such operations that may be converted into a few multiplications by an optimizing FORTRAN compiler requires a function call in C. As a result of these limitations, we have found a significant performance penalty in programs written in C as compared to programs written in FORTRAN, although for most circumstances, a factor of 2 to 4 difference in execution speed is not a serious limitation to an otherwise well-written program. Part of this penalty may be attributed to the fact that the DOMAIN/OS operating system on the Apollo workstations used in our work used Pascal as the native compiler and FORTRAN as the number-crunching compiler, leaving C with no special precedence except compatibility with other UNIX operating systems. Since most other workstations use C as the native compiler, the performance penalty is probably not as great on those systems.

BASIC is popular in applications where performance is secondary to simplified development and debugging, such as in the computer solution of immediate problems and in instrument control. Because BASIC is in general an interpreted language that does not require compilation, development is streamlined. Debugging is also simplified for this reason because syntax errors and run-time errors can be found and fixed simultaneously. However, unless a program is destined to run on only the type of platform for which it was originally developed, one should try to program in a language that is portable to

other platforms. BASIC does not meet this requirement. As BASIC was not available on our workstations, this language was not used for any of this work.

C++ is a superset of C that makes it a flexible language that is modular in construction. It was originally designed to be a simulation language as operators and functions could be defined to work with logical objects representative of physical objects whose internal workings are hidden to the rest of the program. This allows programmers to define objects that can be manipulated but not corrupted, simplifying the task of debugging. However, the concepts and the syntax involved are much more complicated, so the use of this language really only pays off for large, complicated programs. None of our programs were of sufficient complexity to warrant the use of this language.

The Simulation Program

In order to maximize execution speed of the simulation program that would, in some cases, run for days, this program was written in FORTRAN with minimal use of subroutines. The program was originally written by Tom Soules, but major revisions were made by this author to increase its functionality. Blocks of code were added to enable the use of three body potentials, the Gear predictor-corrector algorithm, the application of shear strain, the accumulation of force distributions, and the capability to do a damped molecular dynamics simulation. A C-preprocessor was used to make customized versions of the program at compile time from the same source code so that improvements in common sections of the code could be incorporated into all versions of the code simultaneously. By making the code customized for each type of potential,

integration algorithm, etc., performance was optimized by not including unused sections of code in the executable code. A C-language subroutine was included to output a compacted data stream of position and coordination information because the C language gives one better control of input and output from programs. The stream could then be sent directly to a graphics program using the TCP/IP protocol for a remote real-time visualization capability, or it could be sent to a file for later viewing by a graphics program.

The Graphic Analysis Program

The most complicated analysis program is the graphics program called "mdtv" written in the C programming language. This program is a vastly expanded descendent of the "mdplot" program originally written by Greg O'Rear⁹¹ that used Masscomp native graphics and was capable of displaying snapshot views of the system as two-dimensional projections, of zooming in on certain areas of the projection and of displaying coordination information for certain selected atoms. The current version of "mdtv" uses the native graphics on an Apollo DN10000 workstation and displays animated views of the system in perspective using position and coordination information supplied by the simulation program to make it possible to see the smooth progression of the system. It also includes the capabilities to zoom in on the environment of selected atoms and display coordination information for those atoms. Additional capabilities provided are the abilities to create stereo perspective pairs, to show different perspectives of the system, to create images in TV mode (limited resolution and proper timing for capturing the

images on video, if the correct equipment is available), and to output images to a file in a Hewlett-Packard PCL-5 format compatible with a LaserJet III printer. An innovative capability incorporated in this program is the ability to receive position and coordination data directly from the simulation program through a TCP/IP socket as well as being able to read this information from a data file. This allows the program to display the results of our simulation program running on any host computer on the Internet in real time. This capability was added so that we could possibly produce a video on one computer while running the simulation on another computer without saving the huge amount of data required to produce such a video to a disk. Because of the complexity involved, this program is highly modularized, and it makes extensive use of data structures.

Other Analysis Programs

Because of the amount of I/O involved and the lesser importance of execution speed, most other analysis programs were also written in C with liberal use of subroutines. The C programming language provides better control of I/O and provides data structures that makes the writing of reasonably complex yet short programs easier.

Experimental Techniques

Initial Conditions

The simulations performed in this work were of systems consisting of 1152 particles, as constrained by the number of particles that could be put into a rectangular

cell of low cristobalite having reasonable dimensions. Full periodic boundary conditions were applied in order to model bulk properties.

Low cristobalite structures were formed using atomic positions as given by Wyckoff⁸ with randomly assigned atomic velocities. The structures were then held at a constant temperature for 4000 time-steps, corresponding to about 50 thermal vibration periods, before experiments were performed on them.

It was found that the Soules potential modeled this structure at the known lattice constants at close to zero pressure. The Feuston-Garofalini potential failed as a plausible potential to model low cristobalite as the system pressure deviated significantly from zero when the volume of the system was set to correspond to known lattice constants.

Glass structures were formed by a more complex approach, using two different techniques. The first is to simulate a crystal structure, melt the structure to form a liquid, then quench to form a glass. The second is to start off with a system of random positions and velocities to essentially create the high temperature liquid, then quench to form a glass.

The first method is desirable since one may assume the structure stays in equilibrium until it falls out of equilibrium as the liquid is quenched, just as in a real glass forming operation. However, it is difficult to get a perfect crystal to melt in a simulation. A significant difference between a crystal and a glass is that a glass can melt throughout its volume simultaneously, while a crystal must first melt at its surface or interface. In the simulation of a bulk material, periodic boundary conditions remove all interfaces, thus eliminating the route by which crystals normally melt. Although Feuston

and Garofalini⁸⁴ reported this method for creating a glass by melting at 6000 K, we could not get the initial crystal to melt at the temperature they reported. We therefore heated a cristobalite structure to a maximum temperature of 12,000 K at $1 \text{ K} \cdot \text{ps}^{-1}$, then cooled at the same rate to form a glass structure by this technique.

The second method, first used by Woodcock et al.,⁵¹ can be used to make a glass out of any chemical composition, and has frequently been used for this purpose. The validity of this method is ensured by first simulating the liquid created at high temperatures where much diffusion occurs so that the system loses its memory of its non-physical beginnings. Glass structures by this technique were created by randomly assigning positions and velocities to form a liquid at 20,000 K, then successively quenching to 5000 K, 4000 K, 2000 K, 1200 K, and 300 K with a hold of 4000 time-steps at each temperature.

Application of Uniaxial Strain

Fracture is more often associated with stress than strain, so at first thought, one might desire to model fracture by applying a uniform uniaxial stress on a system. However, on the atomic scale, there is no such thing as uniform stress, as stress becomes the sum of applied forces on individual atoms. In a perfect crystal, these forces would all be equivalent, but in a glass where each atom is in its own unique environment, distributing the applied forces among atoms would be difficult at best. In order to avoid this problem, we apply strain and measure stress, which is consistent with the other aspects of a V , T , N simulation.

We apply uniaxial strain by uniformly scaling particle positions periodically along one of the cell directions. By doing this, we assume uniform uniaxial strain throughout the sample, which is not strictly realistic. However, as we strain at lower strain rates, the empirical aspects of this approach become diminished as particle movements become dominated by thermal vibrations rather than by the applied strain and the applied strain redistributes itself within the structure. At high strain rates, we avoid the application of large instantaneous strains by reducing the periods between the application of strain. Consequently the application of uniform strain proves to be a simple yet effective method for simulating the conditions that result in fracture. By scaling positions uniformly rather than straining the system at a particular plane and letting the strain propagate through the system on its own, we avoid biasing the system towards fracture at a particular location.

The range of strain rate studies available to molecular dynamics is limited at the fast end by the duration of the time step, and at the slow end by the total duration of the simulation. For all strain rates, the size of the expansion must be small for each time step in order to avoid significantly changing the positions of the particles from their equilibrium positions.

In reality, tensile strain cannot be propagated faster than the speed of sound. However, we have investigated this regime (high strain rates) in order to study the behavior of the system while the thermal vibrations are essentially arrested. This result is invaluable for comparison to lower strain rates in order to determine the effect of these thermal vibrations. Therefore, the range of applied strains, 0.05 ps^{-1} to 5.0 ps^{-1} , spanned

the strain rates from a regime where the fracture occurred in 150 thermal oscillations to one where fracture occurred in 1.5 thermal oscillations.

Application of Shear Strain

When a system is elastic, stress and strain are proportional. Even for a viscous system where there is no shear, this is approximately true for small strains. However, when shear stress and shear strain is involved, a viscous system behaves much differently than an elastic system. Liquids are not capable of supporting a shear stress, or rather, do so only transiently. When the viscous properties of liquids are measured, they are generally measured at a constant shear rate, where the system reaches a steady state at a constant shear stress. Thus, whereas stress and strain are proportional for an elastic system, shear stress and shear strain rate are proportional for a viscous system. In order to place a viscous system under shear, we must do so by applying a shear strain at a constant rate. The question then arises, do we model the system so that it looks like a velocity profile is created from the perspective of the both the system and an external observer, or do we force the system into shear by effectively applying an underlying reference frame under shear to which the system must conform so that the system appears to be in constant shear to an external observer, but the particles within the system experiences no velocity profile with respect to that reference frame. As might be suspected, one is complicated, and one is simple.

Forcing the particles into a velocity profile by adding velocity in a static reference frame is problematic. Although we can add velocity to particles based on their position

to cause the formation of some velocity profile, the particles will tend to dissipate the velocity that we add, so we would need to keep adding it. However, we would not know what the resulting velocity of the system would be, so we would have trouble applying periodic boundary conditions. We also could cause an effective shear by shifting the periodic boundary conditions alone, but this would be similar to applying uniaxial strain by merely increasing the size of the cell without uniformly scaling particle positions--shear slip would be biased to occur at the edges of the primary cell. Thus, shear strain is applied in a manner quite similar to the method by which uniaxial strain is applied--by uniformly scaling the positions of particles, in this case, as a function of position in a direction perpendicular to the shear vector, and by changing the shape of the cell accordingly for the purposes of periodic boundary conditions. Because particles are shifted, but left with no residual velocity, shear by this method does not change the velocity profile as experienced by the system, and the system thermodynamics will not reflect the change in velocities. In other words, the reference frame from which particle velocities are measured is in shear itself, so only the deviations from the applied shear are measured by the system, not the shear itself. This is a better way of simulating shear, as velocities in the system frame are used to calculate the average kinetic energy of the system from which the measure of temperature is derived. Clearly any ordered motions should be cancelled out first, otherwise the choice of the reference frame would effect the measured temperature of the system. From the standpoint of an external observer, the system appears to possess a velocity profile consistent with a system in uniform shear.

Because we effectively force a uniform strain on the system, the same limitations on realism apply as in the application of uniaxial strain. The strain rate must be low enough for the particle motions resulting from the applied strain to be small with respect to the motions caused by thermal vibrations within the system in order to realistically simulate shear in a material.

Experiments and Analyses

Phases Simulated

Fracture simulations were performed on both cristobalite and vitreous silica. This was done for two reasons--to simulate fracture in a simple system where the processes of fracture could most easily be distinguished, and to contrast the fracture of a glass with that of a crystal having the same chemical composition and nearly the same density.

Strain Rates Simulated

Fracture of these forms of silica were simulated at different strain rates in order to isolate time dependent events and to simulate the range of local strain rates that a material might experience during fracture. Strain rates ranging from 0.05 ps^{-1} to 5 ps^{-1} were simulated.

Comparison of Potential Functions

The Soules and Feuston-Garofalini potentials were both used in simulations in order to distinguish the role of the three-body potential in the mechanical behavior of the

system. Since the three body potential models the covalent nature of the atomic bonds, this comparison is important for understanding the limitations of potential functions for modeling silica, which is known to have a significant covalent character.

Thermal Effects

Fracture simulations were performed under both isothermal and adiabatic conditions. These represented the cases of infinite thermal conduction and zero thermal conduction, respectively. In addition, by integrating the mechanical work done on the system during strain and comparing to the internal energy of the system under adiabatic conditions, we could get an estimate of the energy of surface formation.

Studies of Determinism

Simulations were performed in order to see if the systems were chaotic in nature. This was done to attempt to provide an atomistic explanation of the chaotic nature of materials observed in fracture at larger scales, e.g., fractal fracture surfaces and chaotic fracto-emission. Simulations were performed in which a small change was made in starting conditions, and the system was either fractured or held as is. Long simulations were performed and a state variable of the system examined to see if it varied in a way so as to suggest chaos in the system.

Studies of Nonlinear Viscosity

Studies of structural failure at high temperature were also conducted to investigate non-linear viscous flow in a silica melt. Here, simulated samples were sheared at various temperatures. Since shear flow of a material requires a liquid-like behavior, higher temperatures were required. Because of the small size and short time scale of MD simulations, temperatures in excess of the macroscopic melting temperature of silica were required to model liquid-like behavior. Temperatures ranging from 2000 K to 5000 K were used for these simulations.

CHAPTER 4 RESULTS AND DISCUSSION

The Models

One of the first questions that one poses to a materials modeler is how he or she knows that the model realistically simulates the intended system. Without some feel of the hits and misses of the model, one cannot have confidence in the results obtained from the model. Thus, we begin the results section with a discussion of the models used in this work. These models are the result of molecular dynamic simulations using two different potential functions.

Because our eventual goal is the understanding of the role of structure in the fracture of materials, one of the most important aspects to be verified for our model is that the structure it provides is correct, or that it at least deviates from the correct structure in understood manner. Thus we will first discuss the static characteristics of the models, that is, measures of structure and state, and will then progress into dynamic properties, such as the responses of the models to a changes in temperature and the application of strain.

Static (Structural) Characteristics

Of the static characteristics, we will first discuss scalar quantities, and will progress to higher order quantities that are significant in our study. These quantities are density, pair correlation functions, bond angle distributions, ring size distributions, free volume distributions, and defect concentrations.

Densities and pressure tensors

The density of the model is the first quantity that one should compare to experiment. However, since our simulations are performed at constant volume, we set the density and observe the resulting pressure. If the pressure of the model at the experimental density is negative (tensile), then the model wants to contract, and the zero-pressure density will be higher than the experimentally derived density at which we perform our simulations. If the pressure is positive (compressive), then the model structure wants to expand, and the zero pressure density will be lower. What we desire is near-zero pressure at the experimental density.

We find that the Soules two-body potential comes close to achieving zero pressure at the accepted densities for both low cristobalite and vitreous silica. The pressure of low cristobalite averaged over all directions is 12.6 kbar. However, this pressure is not isotropic, as it is resolved into stress components of -36.0 and 37.0 along the *c*-axis and *a*-axes, respectively. The pressure of the vitreous silica sample is 12.6 kbar, and is fairly isotropic. These results may be interpreted as suggesting that the densities of the phases modeled by the Soules potential are slightly low, and the *c/a* ratio of the modeled cristobalite phase is too small.

From this standpoint, the Feuston-Garofalini three-body potential does not fare as well. The pressures of the low cristobalite and the vitreous silica are 311 kbar and 122 kbar respectively, both being fairly isotropic. These results suggest that the densities of both simulated phases are too low, and the cristobalite density is far too low, although the c/a ratio may be correct. Feuston and Garofalini admitted that their potential function did not model cristobalite very well because of the presence of long-range interactions. If this is the case, then it is purely coincidental that the Soules two-body potential models both phases with reasonable accuracy, since the Soules potential does not consider any long-range interactions not considered by the Feuston-Garofalini potential. In any case, the Soules potential does apparently give better fits of system densities while using ten fewer adjustable parameters than the F-G potential, which gives it the advantage at this point.

Low-order pair-correlation functions

Differences in the densities of the models are partially explained by the low-order pair correlation functions (PCFs) for the vitreous silica structures.

Si-O first peaks. As figure 4-1 shows, the Si-O first peak for the F-G potential is shifted to a larger distance as compared to the Soules potential. This corresponds to a longer Si-O bond distance, tending to give the structures simulated by the F-G potential a larger specific volume, and therefore, a lower density. One should also compare the widths of the Si-O first peaks for the Soules and F-G potential simulated structures. One of the premises in developing the F-G potential was that the SiO_4 tetrahedra should be rigidly constrained units, with less variation in bond lengths and bond angles. As the

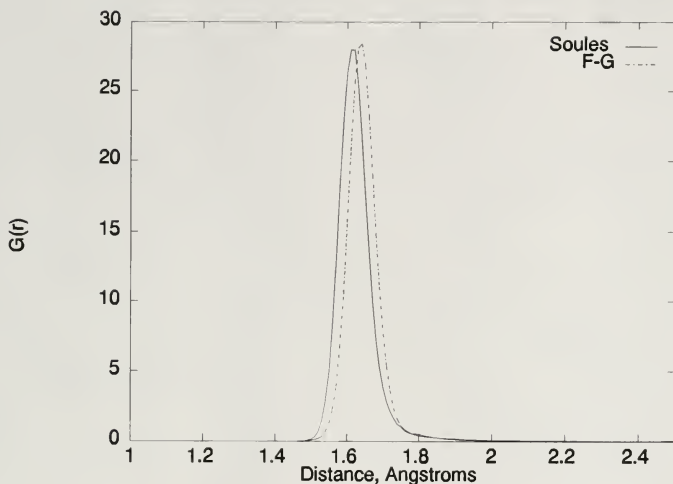


Figure 4-1. Comparison the first peaks of the Si-O pair correlation functions for vitreous silica as modeled by the Soules and the F-G potential functions.

Si-O first peak for the F-G potential is narrower, we find that the goal of a more rigidly constrained tetrahedral units is being approached, in terms of bond length variation. The bond angle comparisons will be made later.

O-O first peaks. A comparison of the O-O pair correlation functions in figure 4-2 shows a similar result. The O-O first peak for the F-G potential is shifted towards a larger distance than the peak for the Soules potential, as required by the larger Si-O first peak distance. Since the O-O first peak corresponds to the edge length of tetrahedra, and should therefore be a function of both bond length and bond angle, one would expect this

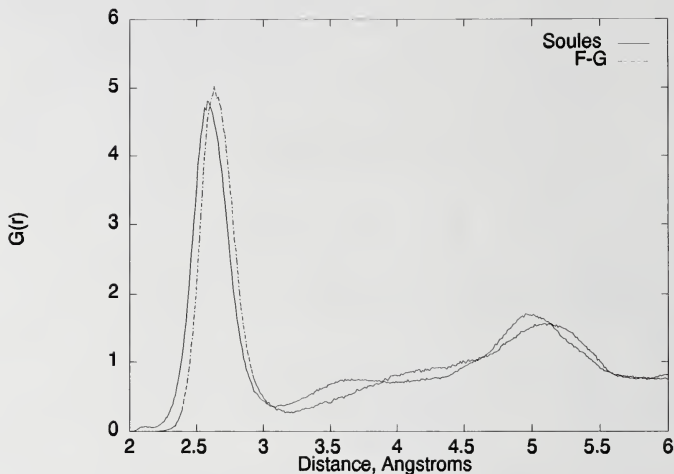


Figure 4-2. Comparison the first peaks of the O-O pair correlation functions for vitreous silica as modeled by the Soules and the F-G potential functions.

peak for the F-G potential to be narrower, as observed. This peak also does not have the tails seen in the O-O first peak from the Soules potential, which correspond on the low side to over-coordinated silicon atoms, and on the high side to some highly deformed SiO_4 tetrahedra.

Si-Si first peaks. The comparative behavior of the Si-Si first peak, shown in figure 4-3, mirrors the comparative behavior of the O-O first peak. Like the O-O first peak, the Si-Si first peak for the F-G potential is shifted to a larger distance as compared to the peak for the Soules potential. Also like the first O-O peak, the Si-Si first peak for

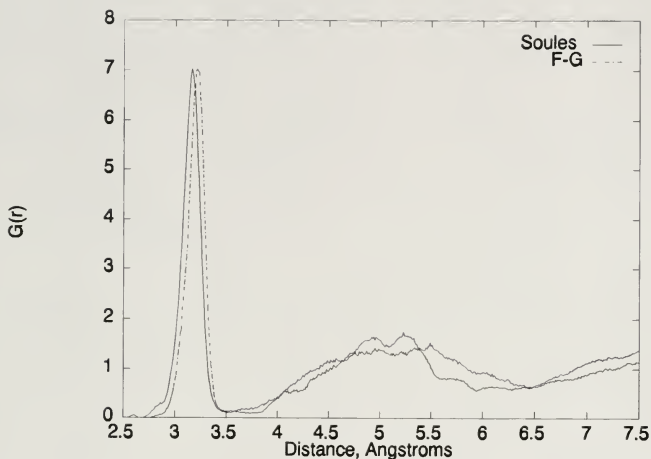


Figure 4-3. Comparison the first peaks of the Si-Si pair correlation functions for vitreous silica as modeled by the Soules and the F-G potential functions.

the F-G potential is narrower than the peak for the Soules potential, but in this case, as a result of a narrower Si-O-Si bond angle distribution rather than a narrower O-Si-O bond angle distribution, as constrained by the Si-O-Si portion of the three-body potential. Finally, the peak for the F-G potential does not have the low end tail observed on the peak for the Soules potential, again indicating fewer over-coordinated silicon atoms for this potential.

High-order pair correlation functions

Comparisons of higher order peaks also show some interesting information. In general, we find that the higher order peaks for the Soules potential are sharper than the corresponding peaks for the F-G potential, in contrast to first-order O-Si, O-O, and Si-Si peaks.

O-O second peaks. The second O-O peaks, which correspond to O-O neighbors on the inside and on the outside of the Si-O-Si bond angle, are distributed differently by the use of the different potentials, as shown in figure 4-2. The Soules potential function results in the formation of distinctly different second O-O peaks. The F-G potential results in the formation of one peak with a broad shoulder while the Soules potential shows a distinct inside O-O second peak. This indicates that the orientation of the tetrahedra may be less correlated with the F-G potential than with the Soules potential.

O-Si second peaks. The second and third O-Si peaks are sharper for the Soules potential than for the F-G potential, as shown in figure 4-4. This again indicates that the orientation of tetrahedra are more correlated with the Soules potential than with the F-G potential. It is also interesting to note the sharp increase of the third O-Si peak at 5.5 Å, which is the cutoff distance for the Soules force function. Though any sharp changes in the PCF at the cutoff distance are suspicious, truncation of the O-Si attraction should result in a sharp decrease in pair correlation at that distance, in contrast to the observed behavior. Thus we presume that this change is not a result of the truncation of the O-Si force function.

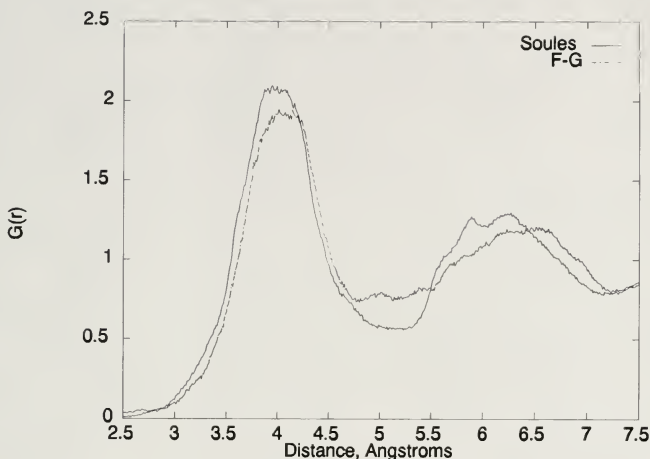


Figure 4-4. Comparison the higher order peaks of the Si-O pair correlation functions for vitreous silica as modeled by the Soules and the F-G potential functions.

Si-Si second peaks. The second Si-Si peaks are again sharper for the Soules potential than for the F-G potential, and the average of the peak is shifted to shorter distances, as shown in figure 4-3. Also, a sharp change in the Si-Si PCF is noted at 5.5 Å which is, as in the O-Si PCF, in the opposite direction of what would be expected from an artifact of the truncation function used.

Discussion of higher order peaks

Why are higher order peaks more correlated with the Soules potential than with the F-G potential? By comparing the functional form of the Soules and F-G potentials

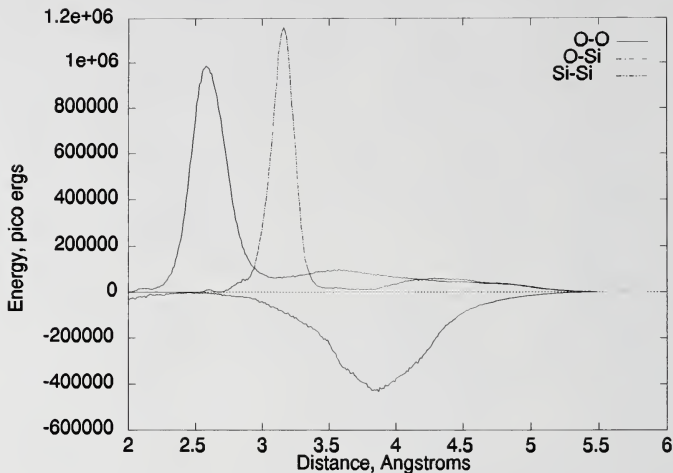


Figure 4-5. Contribution of various pair interactions to the potential energy of vitreous silica as modeled by the Soules potential function.

in figures 4-1 and 4-2, we find that interactions beyond the O-Si first peak are screened more completely in the F-G potential than in the Soules potential. Since the longer-range interactions should have a larger effect on determining the medium-range order, the increased correlation of tetrahedra with the Soules potential function is expected. In order to pinpoint the interaction that most determines this medium-range order, we examine the function of the product of the pair correlation function and the pair potential functions for each interaction type and for each potential, figures 4-5 and 4-6. We find that the relative dominance of the O-O first repulsion and the Si-Si first repulsion is

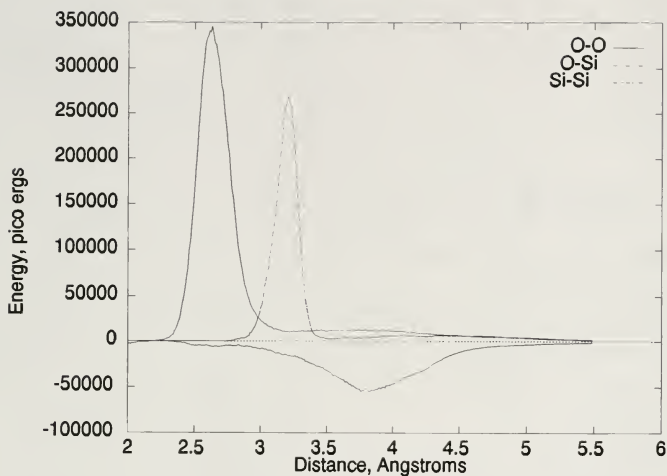


Figure 4-6. Contribution of various pair interactions to the potential energy of vitreous silica as modeled by the F-G potential function.

changed with the different potential functions, with the Si-Si first repulsion playing a relatively larger role in the Soules potential, and the O-O first repulsion playing a relatively larger role in the F-G potential. It is also found that the O-Si second attraction is relatively larger for the Soules potential than for the F-G potential. The O-Si second attraction may be the true reason for the enhanced correlation between SiO_4 tetrahedra since the O-O second peak is on average decreased, and thus the O-Si attraction is increased at the expense of the increased O-O repulsion.

The abrupt changes at 5.5 Å are probably the result of the end of the coordination of nearest tetrahedra at this distance. This change is probably more abrupt for the Soules potential where the orientation of adjoining tetrahedra are more correlated than for the F-G potential. If we try to make sense out of the peaks beyond 5.5 Å, we find that the different PCF's are roughly complementary, that is, an increase in the O-O PCF results in a decrease in the O-Si PCF and vice-versa. The same relationship holds between the O-Si and Si-Si PCF's. This demonstrates that for both models beyond the first tetrahedral neighbors, space is filled roughly uniformly, though some variations in the individual pair correlation functions still exist.

Bond angle distributions

O-Si-O bond angle distributions. Bond angle distribution functions show expected results. Figure 4-7 shows that the O-Si-O bond angle distribution is narrower and more symmetric for the F-G three-body potential than for the Soules two-body potential. The differences in symmetry are caused by differences in the number of defects resulting from the two potential functions. The Soules potential function results in more five coordinated silicon atoms than does the F-G potential, which is evidenced by a low-side shoulder on the O-Si-O bond angle distribution peak.

Si-O-Si bond angle distributions. The Si-O-Si bond angle distributions shown in figure 4-8 exhibit little difference between the two potential functions. There is a small peak present in the distribution corresponding to the Soules two-body potential at about 100° that occurs at the low end of the tail of the distribution corresponding to the F-G

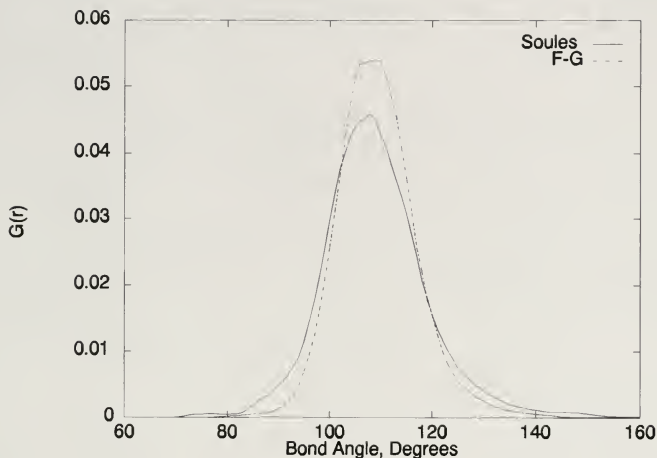


Figure 4-7. Comparison of O-Si-O bond angle distributions for vitreous silica as modeled by the Soules and the F-G potential functions.

potential. This peak may correspond to bonding between two highly deformed tetrahedra.

Comparison of structural distributions to experiment

Adrian Wright compared the radial distribution functions derived from a neutron diffraction experiment to those derived from our molecular dynamics simulations using the different potential functions. We find that there is a strong correspondence between the deviations of the simulated pair correlation functions with each other and the deviations of simulated radial distribution functions with the experimental radial distribution functions, as shown in figures 4-9 and 4-10. For example, it was shown in

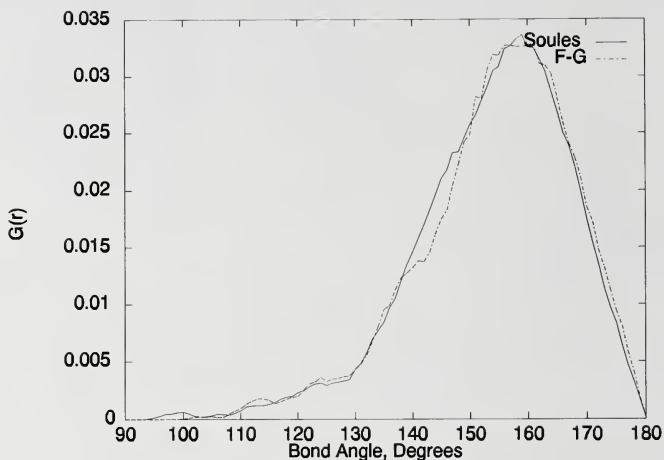


Figure 4-8. Comparison of Si-O-Si bond angle distributions for vitreous silica as modeled by the Soules and the F-G potential functions.

figure 4-1 that the first Si-O peak ($\sim 1.6 \text{ \AA}$) for the vitreous silica sample simulated by the F-G potential was shifted to a larger distance as compared to the peak in the sample simulated by the Soules potential. In the comparisons to the neutron diffraction data, we see that the radial distribution function for the F-G potential deviates significantly from the data at this point as a result of this shift. Although the O-O first peak ($\sim 2.5 \text{ \AA}$) given by the F-G potential is narrower than the O-O first peak given by the Soules potential, as was shown in figure 4-2, we find that both are too broad in comparison to experimental data. Because both simulated peaks are too broad and because the peak given by the F-G potential is again shifted to a larger distance, the F-G potential matches

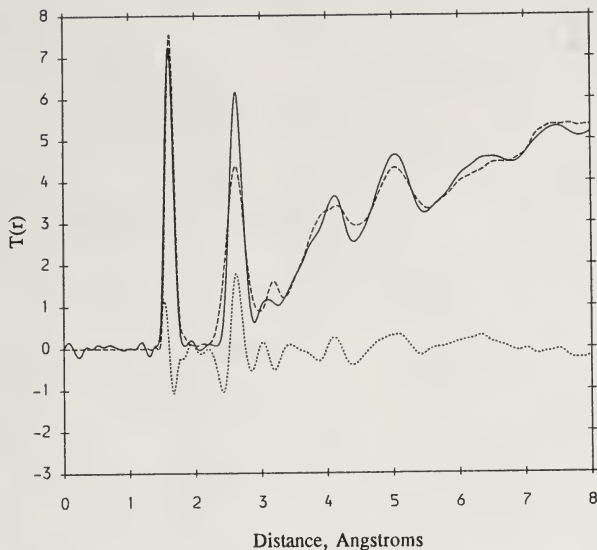


Figure 4-9. Comparison of radial distribution functions derived from a neutron diffraction experiment (solid line) and a molecular dynamics simulation using the Soules potential (dashed line).

the low side of the O-O peak more closely than does the Soules potential, but at the expense of a poorer fit at the high side of the O-O peak. However, since the F-G potential seems to result in fewer coordination defects, the small bump ($\sim 2.1 \text{ \AA}$) resulting from the over-coordination of silicon atoms by oxygen atoms on the low side of the O-O peak is avoided, so the F-G potential seems to match experiment better than the Soules potential in this respect. Neither potential does very well in fitting the Si-Si first peak ($\sim 3.1 \text{ \AA}$), as both are shifted to larger distances and are too sharp as compared to the

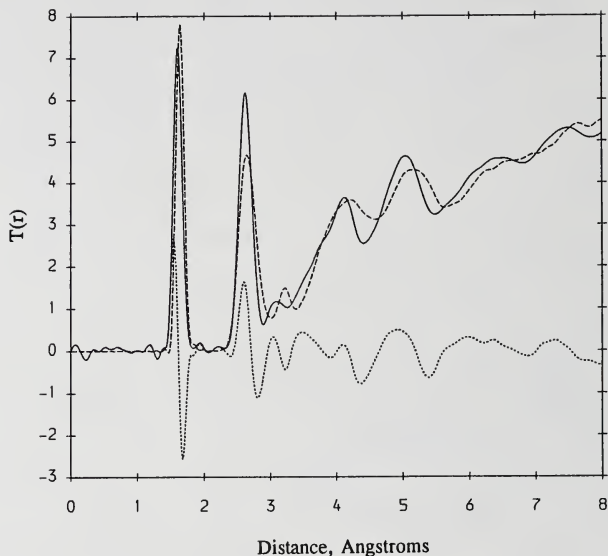


Figure 4-10. Comparison of radial distribution functions derived from a neutron diffraction experiment (solid line) and a molecular dynamics simulation using the F-G potential (dashed line).

experimental data. This indicates that for both potentials, the Si-O-Si bond angles are too large, on the average, and that the distribution is not broad enough. Because bond angle distributions are necessarily limited, this means that both potential functions result in bond angle distributions that are skewed towards 180 degrees. The higher order O-O peaks ($\sim 3.6 \text{ \AA}$ and $\sim 5.0 \text{ \AA}$) are fitted better by the Soules potential than by the F-G potential, but both are too broad as compared to the experimental data. Neither potential seems to fit the Si-O second peak ($\sim 4.0 \text{ \AA}$), as both seem to be too broad. Based on the

pair correlation functions shown in figures 4-2, 4-3, and 4-4, we argued that the Soules potential resulted in a greater degree of inter-tetrahedral correlation than the F-G potential. From these comparisons, it is clear that inter-tetrahedral correlations that are dependent on the rather flexible Si-O-Si bond angle are an important aspect in the structure of vitreous silica. The overall fits are quantified by the crystallographic R factor, which expresses the overall deviation over the range of comparison. Use of the Soules potential resulted in a better overall fit, with a R_x of 10.1%, than use of the F-G potential, with an R_x of 14.7%.

In agreement with the radial distribution function results, we find that neither the Soules potential nor the F-G potential creates a structure in which the Si-O-Si bond angle peaks at the 144° angle deduced by Mozzi and Warren⁹² in their determinations on the structure of silica, nor do either peak in the range of 142° to 151° as deduced by R.F. Pettifer et al.⁹³ However, it is interesting to note that Mozzi and Warren state that there is little correlation in the dihedral angle, which would be better exemplified by the F-G potential. Our simulations show that there seems to be a large degree of inter-tetrahedral correlation, which suggest that although there may be no one particular favored dihedral angle, there may be a preferred dihedral angle that is a function of the Si-O-Si angle, and Mozzi and Warren were unable to measure this correlation.

Ring statistics

For each potential, two ring distributions are shown in figure 4-11. The first is the ring distribution resulting from the quench of a melt formed by assigning random particle positions and velocities at 20,000 K, then quenching in steps to 300 K, while the

second results from melting a low cristobalite sample by continuously heating from 300 K to 12,000 K, then continuously cooling to 300 K to form a glass.

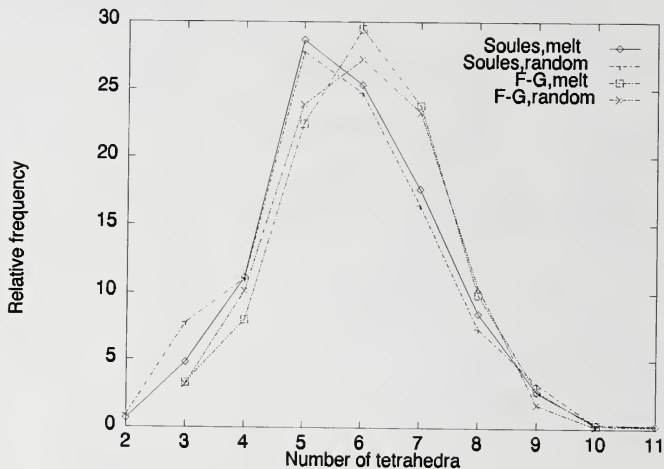


Figure 4-11. Comparison of the ring size distributions for vitreous silica as modeled by the Soules and the F-G potential functions and as formed by crystal melt and random position techniques.

The ring statistics distributions show the differences in the medium-range order developed by the different potential functions. The ring size distributions peak at five-membered rings when the Soules potential is used, and at six-membered rings when the F-G potential is used. It is difficult to find any correlations in the peak ring probabilities based on the forming conditions used.

We see that the F-G potential results in ring size distributions that have fewer two-, three- and four- membered rings as compared ring size distributions resulting from the Soules potential. Three- and four- membered rings have been observed in Raman scattering in silica and have been termed "defects" in the past because of their relatively small numbers, but are now believed to be a small but integral part of the vitreous silica structure.⁹⁴ Two-membered rings are not generally observed in experiments because they usually result from bond fracture and therefore reside most often on surfaces. In our simulation, they may be stable because there are no other species, such as water molecules, to hydrolyze the strained bonds. In a bulk material, two-membered rings are probably a defect, and the presence of these rings in a simulated bulk probably demonstrates a shortcoming of the simulation. Any occurrence of these rings in a simulation of a small sample of material implies a rather high concentration of the rings in a simulated bulk material.

We used various forming techniques in an attempt to improve the ring size distribution, that is, decrease the incidence of smaller rings. By forming structures using the melt-then-cool technique instead of the random-then-quench technique used in all previous simulations, we hoped that the ring size distributions of the original cristobalite structure might be preserved in some way during melting and subsequent cooling, reducing the abundance of small rings in the vitreous silica structures. The results, however, show little correlation between the ring size distribution and the forming method used. This indicates that the ring structure becomes totally disintegrated under

the melting conditions used in this experiment, resulting in ring structures that are much more dependent on potential functions than on the forming conditions used.

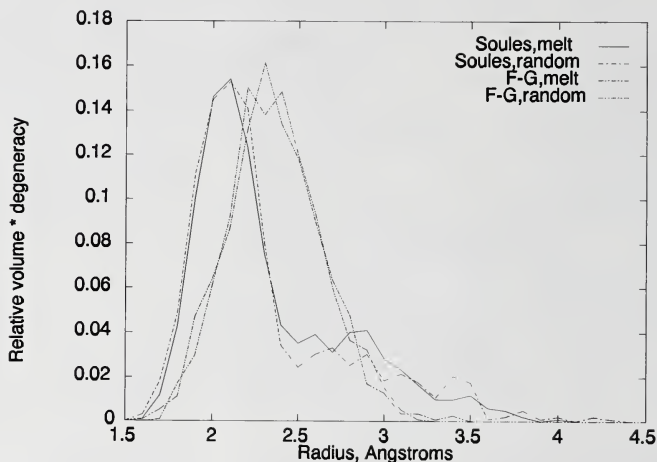


Figure 4-12. Comparison of the free volume sphere size distributions for vitreous silica as modeled by the Soules and the F-G potential functions and as formed by various techniques.

Volume distributions

In examining the free volume distribution functions shown in figure 4-12, we again find that there are differences in the medium-range order resulting from use of the two potential functions. The free volume distribution function for the Soules potential shows a narrow peak at about 2 Å radius, with a shoulder at 3 Å that extends to 4 Å. The free volume distribution function for the F-G potential shows a broader peak

centered at about 2.4 Å radius, with no shoulders, making the entire distribution narrower than for the Soules potential. Again we find that the structure is less sensitive to forming method than to the potential function used.

Table 4-1

Coordination of species in simulations using various potentials and methods of formation as found by the ring statistics program.

| Coordination | Predominance of Configuration | | | |
|--------------------|-------------------------------|------------|----------------|------------|
| | Soules Potential | | F-G Potential | |
| | Random, Quench | Melt, Cool | Random, Quench | Melt, Cool |
| Silicon by Silicon | | | | |
| 3 | 0.78 | 0.52 | 4.69 | 4.95 |
| 4 | 82.55 | 86.98 | 82.81 | 87.50 |
| 5 | 13.02 | 9.64 | 12.50 | 7.55 |
| 6 | 1.82 | 2.60 | 0.00 | 0.00 |
| 7 | 1.82 | 0.26 | 0.00 | 0.00 |
| Oxygen by Silicon | | | | |
| 1 | 0.13 | 0.39 | 1.95 | 1.69 |
| 2 | 97.14 | 97.53 | 96.09 | 97.14 |
| 3 | 2.73 | 2.08 | 1.95 | 1.17 |

Defects

In examining the bonding defects in the simulated silica structures, we find differences in the defect states of the samples based on their formation history and the potential function used as are summarized in Table 4-1. Although the effects of potential

function are larger than the effects of formation method, we find that the method of formation has a significant effect on gross coordination defects that are overshadowed in the higher-order correlations. The results show that the melt-then-cool method is a better method of producing a structure than is the random-quench method, at least with the parameters utilized here.

Dynamic Properties

We will now discuss the properties of the system that are dependent on the dynamics of the system. These include melting temperature and mechanical properties.

Melting temperature

The melting temperature of cristobalite modeled by the two potentials appears to be elevated with respect to experimental findings. The accepted melting temperature of high cristobalite is 2090 K, however, the melting of cristobalite by either potential function does not occur below 6000 K in our simulations. There are a few reasons for this.

The first is that super-heating occurs because there are no surfaces available on which melting can begin. In nature, crystals generally melt from their surfaces. This is contrasted to amorphous materials that undergo a gradual melting throughout their bulk with minimal surface effects. When a perfect crystal is provided no surfaces from which to melt, one may expect the melting point to be elevated over the experimentally determined melting point.

The second reason is that the time frame over which we observe a system is short in comparison to the time frame in which macroscopic processes occur. A small sample of liquid at 300 K over a period of a few picoseconds does not look much different from a solid under the same conditions. Thus, we are unable to clearly witness melting even when it does occur, and there is probably a lag between when melting actually occurs and when we observe it.

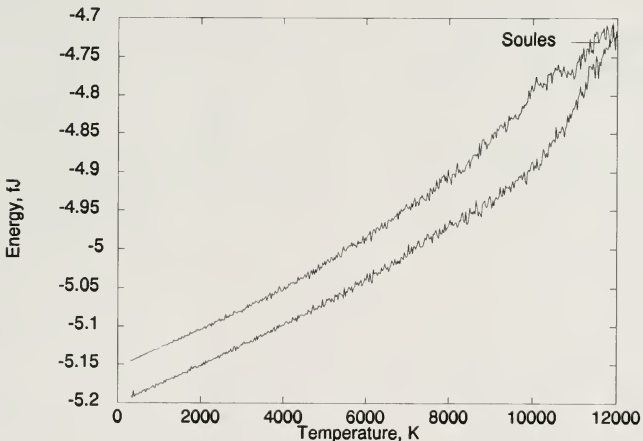


Figure 4-13. Potential energy as a function of temperature for cristobalite as modeled by the Soules potential.

The third reason for elevated melting temperatures is the result of limitations in the potential function used. The dependence of the melting point on the potential function is clearly seen in the system potential energy curves of figures 4-13 and 4-14.

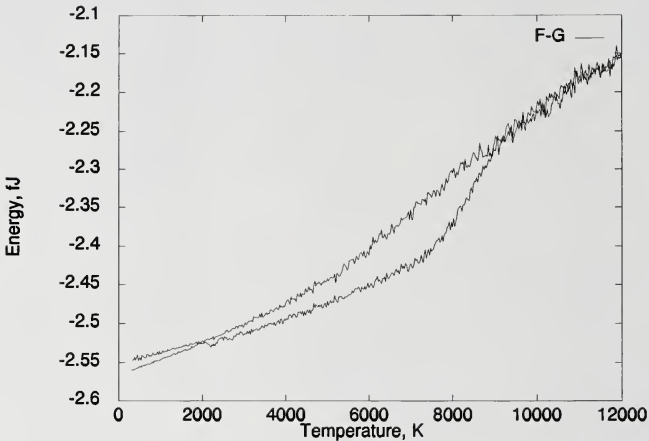


Figure 4-14. Potential energy as a function of temperature for cristobalite as modeled by the F-G potential.

The melting temperature when using the Soules potential is about 10,000 K, based on the change of the slope of the potential energy versus temperature curve at this temperature. When using the F-G potential, the melting temperature is about 8000 K by the same analysis. This indicates that the bonds are stronger using the Soules potential than with the F-G potential. This is also supported by the lower potential energy of the Soules potential system as compared to the F-G potential system, as is also evidenced in figures 4-13 and 4-14.

at 87.5 GPa up to 10% strain, then increasing to 125 GPa up to 20% strain, then increasing again to 225 GPa at 20% strain. This demonstrates that the connectivity of cristobalite silica is sufficient to give a non-linear elastic response that is over-accentuated in the case of the Soules two-body potential and is better handled by the F-G potential.

The non-linear elastic response of cristobalite silica is the result of different limiting mechanisms to the application of strain at different strain levels. At low strains, strain is added by increasing the Si-O-Si bond angles with little change in the Si-O bond lengths. At greater strains, the Si-O-Si bonds have been fully extended, so further strains must be accommodated by increasing bond lengths. With the Soules two-body potential, bond angles can be changed relatively easily, but changes to bond length require much more effort. With the F-G three-body potential, changes to bond angles require more effort, and changes to bond lengths require less effort, as compared to the Soules potential.

The vitreous samples do not show the desired behaviors. Both potentials result in structures in which the apparent longitudinal modulus decreases with increasing strain. The failure of the vitreous silica model to demonstrate a non-linear elastic response as observed by experiment may be caused by the over-abundance of small rings in our structures that result in a structure which is overly rigid at small strains. Perhaps if the abundance of small rings could be reduced, then the rigidity of the structure at small strains could be reduced without decreasing the overall strength of the material. The failure of the samples of either potential to behave as such may indicate that there are still too many small rings in the samples.

Mechanical properties

Experimentally, it is seen that vitreous silica has a non-linear elastic response, in which the apparent elastic modulus increases with increasing strain. We sought to duplicate this finding through our computer simulations.

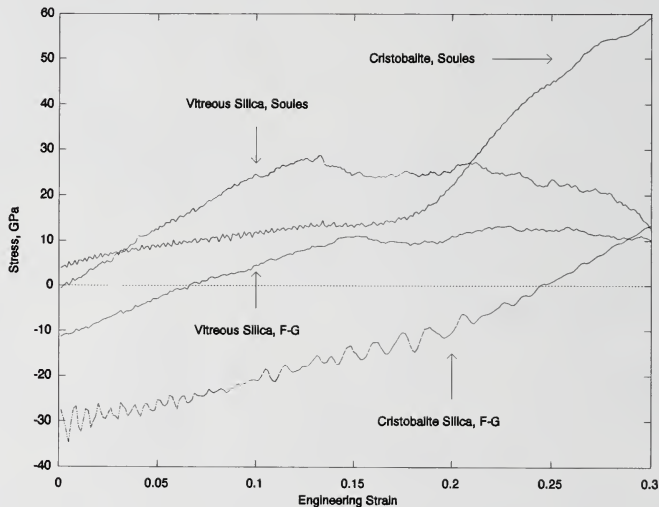


Figure 4-15. Equilibrium elastic stress-strain curves for cristobalite and vitreous silica as modeled by the Soules and the F-G potential functions.

As shown in figure 4-15, the stress-strain curve for cristobalite displays a highly non-linear elastic response. In the case of the Soules potential, the change in longitudinal modulus occurs abruptly at about 18% uniaxial strain, from approximately 66 GPa to 525 GPa. For the F-G potential, the change in longitudinal modulus is more gradual, starting

currently considered a fairly decent fit to neutron diffraction data with R_x factor of 10.1%. However, it completely ignores covalent nature of Si-O bond, and it uses stronger potentials to obtain tetrahedral bonding, resulting in elevated melting temperatures in the cristobalite sample and an unrealistically high elastic modulus in the vitreous silica sample.

The Feuston-Garofalini three-body potential acknowledges the covalent nature of Si-O bond. Because the three-body part of the potential encourages tetrahedral bonding of silicon atoms by oxygen atoms, a weaker two-body portion of the potential may be used, resulting in more realistic melting temperatures and elastic moduli. This potential also creates a vitreous silica structure having fewer topological defects. However, the densities for both polymorphs are not very good and are especially bad for low-cristobalite. Also, the neutron diffraction fits are worse with R_x factor of 14.7%.

Fracture by Application of Uniaxial Strain

Overview

Although a study of fracture in vitreous silica is our primary interest, the path leading to fracture in this material is too complicated to analyze without first attempting to analyze the fracture in a simpler material. In principle, by simulating the fracture of the crystalline form of silica that is most similar to the vitreous form, we should be able to separate the effects of structure from the effects of simulation potential. Thus, in describing fracture in silica, we first start with a description of the fracture of low cristobalite, then progress to a description and discussion of the fracture of vitreous

Another possible reason for the failure of our models to show the desired non-linear elastic modulus behavior is that our Si-O-Si bond angles are already extended in the unstrained case as compared to experimentally derived structures. Since the low-strain modulus is dependent on the opening of these bond angles, a structure in which these bond angles are already opened in its unstrained state will not show the same strain-dependence of its elastic modulus.

We calculated the elastic moduli of the various systems from the longitudinal moduli at low strains. The cristobalite samples had elastic moduli of 55 GPa and 73 GPa, and the vitreous silica samples had elastic moduli of 220 GPa and 125 GPa, for the Soules and F-G potentials, respectively. The values of the moduli for both the vitreous silica samples are greater than the experimentally determined value for the linear part of the elastic modulus of 71.9 GPa.²⁵ Again, the high value of the elastic modulus in vitreous silica when using the Soules potential as compared to the F-G potential can be attributed to the high bond strengths required to obtain tetrahedral bonding in a purely ionic system.

Review of Models

We have investigated models for vitreous silica and cristobalite described by two different potential functions. Each potential function has its advantages and disadvantages.

The Soules two-body potential has the advantage of being simple and fast. It works well for both the vitreous silica and cristobalite phases. It also provides what is

silica. We will see that the fracture of vitreous silica involves many concepts involved in the fracture of cristobalite, but progresses to a higher level of complexity.

It is instructive to introduce some terminology that we will use in the discussion of fracture. The point of *failure* will be defined as the point on the stress-strain curve where stress reaches a maximum. The point of *fracture* will be the point where the stress-strain curve reaches zero stress after reaching a maximum upon increasing strain. Ordinarily, in brittle fracture experiments, these are close to being one and the same. However, on the microscopic scale and over a very short time period, they differ appreciably. This is caused by several aspects of our simulation experiments. The first is that the high strain rates under which we strain result in the short but finite time from failure to fracture appearing to be smeared out on a stress-strain curve. The second is that we are modeling only the earliest stages of brittle fracture, the crack initiation in a small volume of a material. The third is that we are applying a constant strain rate to a sample, and not a constant stress. In most fracture experiments, a constant stress is applied that makes the fracture catastrophic once the point of failure has been reached. These factors collectively cause our stress-strain curves to appear different than those derived in a brittle fracture experiment, and to exhibit a separate point of failure from the point of fracture.

Low Cristobalite

Structures of low cristobalite were strained along a 100 axis to fracture at strain rates varying from 0.05 ps^{-1} to 5.0 ps^{-1} . The mechanical behaviors above 0.5 ps^{-1} were

clearly dominated by the limited dynamic compliance of the material at high strain rates, so we will discuss in detail only the results from strain rates at or below 0.5 ps^{-1} . Both isothermal and adiabatic fracture experiments were performed in order to better understand the thermodynamics of fracture.

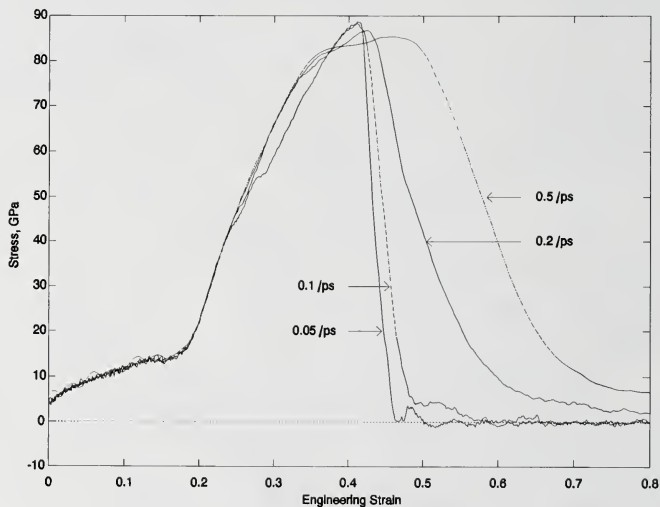


Figure 4-16. Comparison of stress-strain curves at various strain rates for low cristobalite as modeled by the Soules potential.

Stress-strain curves

The stress-strain curves for the cristobalite samples show several aspects worthy of mention. It is observed that elastic strain occurs that is nearly independent of strain

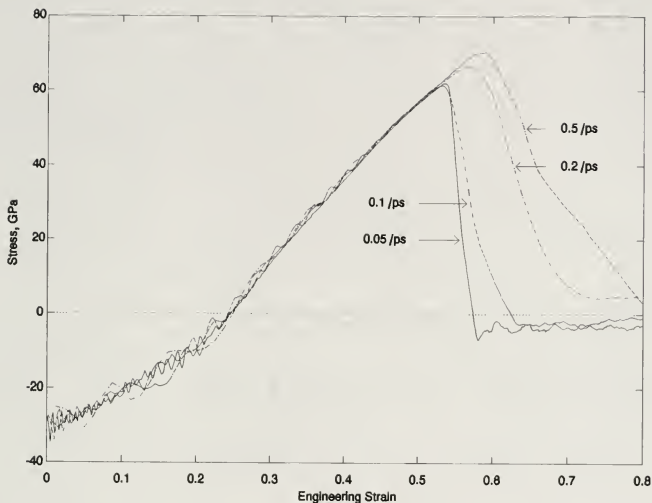


Figure 4-17. Comparison of stress-strain curves at various strain rates for low cristobalite as modeled by the F-G potential.

rate for both potentials. However, at the onset of failure, both strain-rate dependent and potential-type dependent effects are observed.

Figure 4-16 shows that the elastic properties of cristobalite simulated using the Soules potential is independent of strain rate to about 0.25 strain. At higher strains, the sample undergoes a transformation evidenced by a plateau in the stress-strain curves, the onset of which is strain rate dependent. After this transformation, stress again increases with increasing strain until the onset of failure. The stress at failure is nearly independent of strain rate at about 85 GPa, but the strain at failure is dependent on strain

rate, and varies from about 0.415 for a 0.05 ps^{-1} strain rate to 0.46 for a 0.5 ps^{-1} strain rate.

Figure 4-17 shows that the elastic response of the cristobalite sample simulated using the F-G potential is again independent of strain rate, but with no intermediate transformation, this behavior continues until the onset of failure at greater than 0.5 strain. Both the stress and strain at the point of failure are strain rate dependent, ranging from about 62 GPa at 0.53 strain for the 0.05 ps^{-1} strain rate to 70 GPa at 0.59 strain for the 0.5 ps^{-1} strain rate.

Differences in the strain at the point of failure between the different potentials may be partially attributed to the differences in stresses in the "unstrained" samples, and partially attributed to differences in the stability mechanisms of the strained samples. Since the F-G potential starts off with the cristobalite in compression along the strain axis, the sample is not put into tension until about 0.23 strain. By this analysis, it is found that the point of failure is reached at strains of 0.24 to 0.35 if we consider the sample at 0.23 strain to be the unstrained sample.

Differences in the failure stress for the two potentials is also noted. Part of this difference can be attributed to the differences in the magnitudes of the forces obtained from the potentials. The Soules potential leads to a stronger oxygen-silicon bonding as compared to the F-G potential, as is shown in figures 4-3 and 4-4. This should ultimately influence the failure stress of the material, resulting in the material simulated by the Soules potential being stronger than the material simulated by the F-G potential.

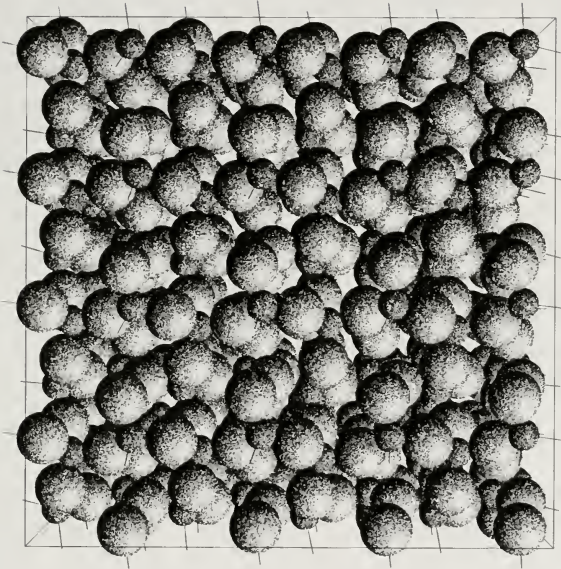


Figure 4-19. View down the C-axis of low cristobalite under an intermediate tensile strain applied along the C-axis, as modeled by the F-G potential.

low cristobalite during strain, as is shown in figures 4-18 through 4-21. Figures 4-18 and 4-19 show the structure at intermediate or low strain for the Soules and F-G potentials, respectively. It should be noted that both the Soules and F-G potential

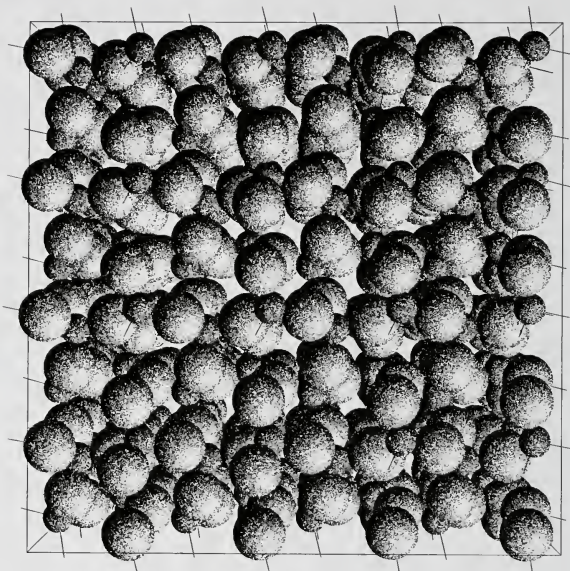


Figure 4-18. View down the C-axis of low cristobalite under an intermediate tensile strain applied along the C-axis, as modeled by the Soules potential. In this view and in all following views, oxygen atoms are represented by the larger, lighter balls, and silicon atoms are represented by the smaller, darker balls.

The differences in the point of maximum stress at different strain rates indicate that the path to instability may be different in the F-G cristobalite than in the Soules cristobalite. This path is identified by looking down the C-axis (the strain axis) of the

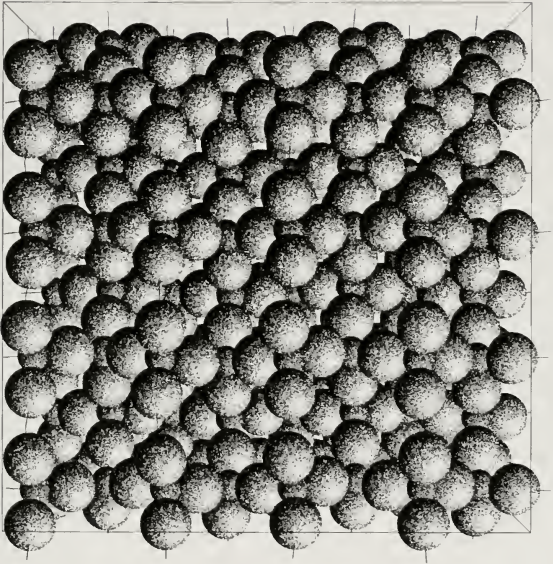


Figure 4-20. View down the C-axis of low cristobalite under a high tensile strain applied along the C-axis, as modeled by the F-G potential.

systems show a perturbed square lattice projection along the C-axis at low or intermediate strains. As the strain is increased, something interesting happens. For both systems, the perturbations from the underlying lattices decrease as thermal rotation of

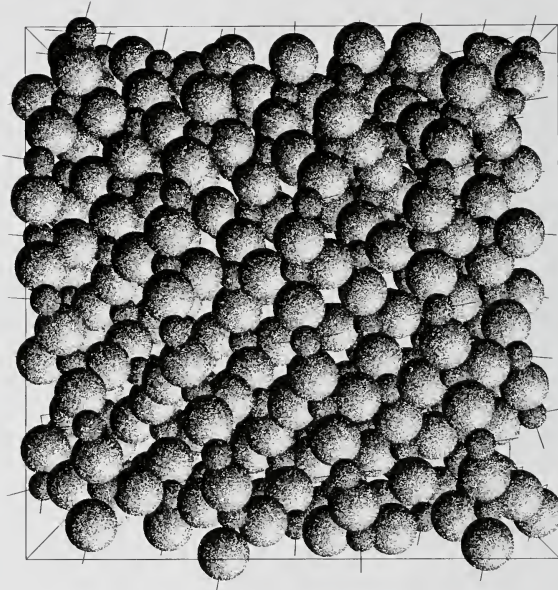


Figure 4-21. View down the C-axis of low cristobalite under a high tensile strain applied along the C-axis, as modeled by the Soules potential.

tetrahedra become more costly at higher strains. However, the symmetry of the Soules system breaks during the transformation observed in the stress-strain curves, while the F-G system retains its square projection symmetry, as is shown in figures 4-20 and 4-21

respectively. The lattice of the Soules system seems to undergo some type of twinning as planes of atoms become bent. The loss of symmetry differentiates certain bonds from others, which aids in the introduction of an instability into the system. This makes the point of maximum stress more strain-rate dependent for the F-G system than for the Soules system because instability in the F-G system is more dependent on statistical fluctuations in the system having a limited frequency of such fluctuations.

This demonstrates an interesting trend. The fact that the fracture stress is nearly single-valued for the Soules potential indicates that the same weak link is active at all strain rates. In the F-G system, there are no obvious weak links, so the system waits until one surfaces. Thus, at reasonably high strain rates, the strength of a more perfect system is less predictable than the strength of less perfect system, because the strength of the more perfect system is limited by unpredictable random motions of atoms in the lattice, while the strength of the less perfect system is limited by predictable flaws.

This illustrates an important point in the strength of a system. A system is not considered fractured and can support higher stresses until the equilibrium state of the system under its applied constraints shifts from connected to disconnected. In principle, this shift occurs when pair of atoms are separated at a distance at which the second derivative of the interatomic pair potential becomes negative, that is, increasing separation results in a decreased interatomic force. In a perfect crystal with no thermal vibrations, this may occur for all pairs of atoms simultaneously. In reality, thermal motions perturb interatomic bonds so that some pairs of atoms will reach this separation distance before others, even in a structurally perfect crystal. The more time a system

is given to fail, the more likely that a large perturbation will come along that will cause the system to fracture at some stress less than the maximum, and the more likely that fracture will be initiated from a single point, causing fracture to be localized. Thus, time in such a system has a similar effect to size in a system with a distribution of structural defects or flaws.

Once the point of maximum stress is reached in the cristobalite systems, it is observed that fracture occurs abruptly. This indicates that the elastic strain energy stored in the structure at the point of an initial instability is sufficient to fracture the entire structure.

The rate at which the stress falls off with increasing strain after fracture has occurred appears to be dependent on the strain rate, but is actually an artifact of the high strain rates investigated. The stress falls off at roughly a constant rate with respect to time, however, the amount of time represented by an increment of strain at a high strain rate is smaller than the amount of time represented by an increment of strain at a lower strain rate. Thus, the stress appears to fall off more slowly with strain at high strain rates than at low strain rates.

Energetics of fracture

Energy added by the application of strain to a material under stress is released in other forms as fracture occurs. During the application of strain, the system may store energy in a number of forms, including elastic strain energy, thermal energy, or configurational energy associated with a change in the structure of the system. When fracture occurs, this energy may be released in a number of forms. In real materials,

these forms include excess system potential energy resulting from surface formation, heat energy, which is subsequently conducted away from the fracture region, and the potential and kinetic energy associated with the emission of particles and light. Since our simulations are confined by closed volume periodic boundary conditions and are only capable of modeling atomic dynamics, the forms that this energy may take are limited to excess configurational potential energy and heat energy.

In most of our fracture experiments, we hold the system under isothermal conditions, that is, any energy created to heat is simply removed from the system. Because our simulations were not set up to measure the amount of energy removed, we can measure the heat energy liberated only during adiabatic fracture simulations, thus strain-to-fracture experiments were performed under adiabatic conditions to investigate the flow of system energies during fracture. The evolution of heat in the system can be differentiated from the change in the system configurational energies because heat appears as system kinetic energy, whereas the configurational energies appear as system potential energy.

An investigation of the system energies as a function of applied strain on low cristobalite modeled by the Soules potential shows distinct points of interest during strain-to-fracture. The first point of interest is a decrease in the slope of the potential energy-strain curves shown in figure 4-22 corresponding to the change in symmetry of the crystal under strain as discussed earlier. This represents a decrease in configurational energy during a period of increasing strain energy. Since the rate at which strain energy is added is proportional to the stress at a strain, which is always increasing to the point

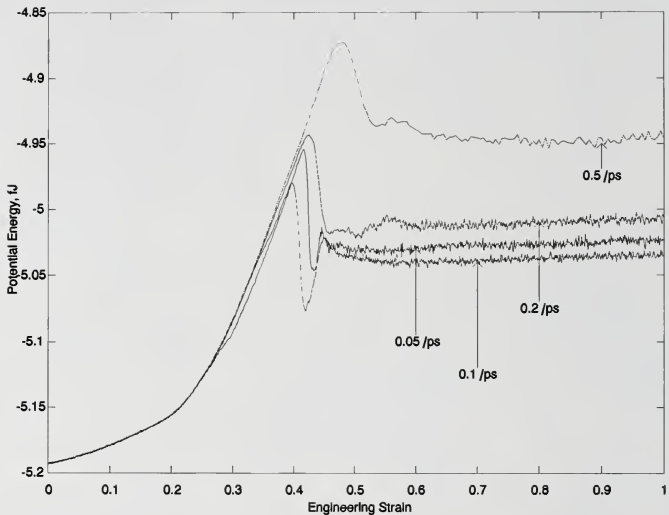


Figure 4-22. Potential energy as a function of strain for low cristobalite as modeled by the Soules potential function under adiabatic strain at various strain rates.

of failure, a temporary decrease in the slope of the potential energy-strain curve means that energy is going elsewhere. The missing energy is located in the kinetic energy-strain curve shown in figure 4-23. It is seen that the kinetic energy takes a jump at the same strain at which the potential energy takes a dip. Thus consistency is maintained.

The next point of interest is the point of failure. In such a perfect crystal at room temperature, the point of failure corresponds to the transition between the elastic and anelastic strain regions. Because a perfect crystal with no exposed surfaces can undergo

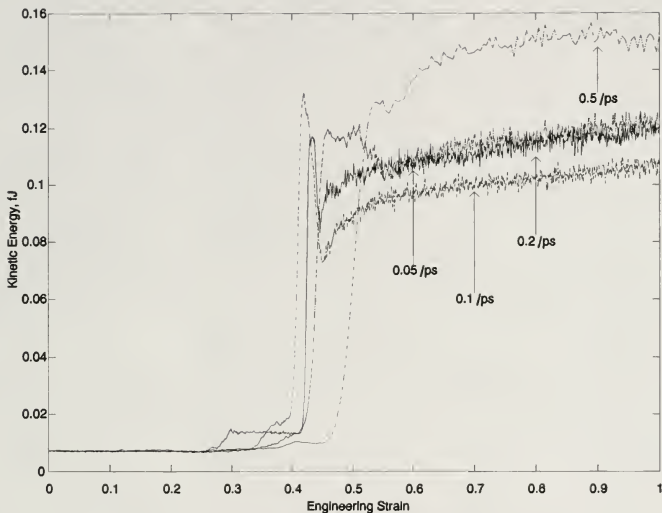


Figure 4-23. Kinetic energy as a function of strain for low cristobalite as modeled by the Soules potential function under adiabatic strain at various strain rates.

significant elastic strain before failure, the recoverable elastic strain energy stored in the lattice is sufficient to cause fracture once a crack is initiated. When a bond is broken, enough energy is released to form an avalanche of broken bonds throughout the structure so that elastic strain energy is almost completely released and converted to kinetic energy. Because the temperature of such a system is directly proportional to its kinetic energy, the temperature of the system increases during fracture. As a result of the large fracture-surface-area to volume ratio, the kinetic energy per particle, and thus the

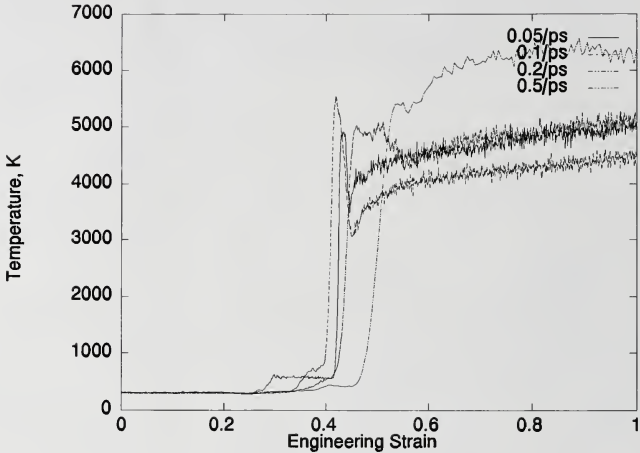


Figure 4-24. System temperature as a function of strain for low cristobalite as modeled by the Soules potential function under adiabatic strain at various strain rates.

temperature, of the sample increases dramatically, as shown in figure 4-24. A schematic showing the flow of energy during strain to fracture is given in figure 4-25.

It should be noted that there is little change in the system kinetic energy during the elastic portion of strain. Since kinetic energy really represents thermal energy, this means that the mechanical strain energy is not converted to heat in such a material until failure occurs, and that the strain is nearly totally reversible. As soon as bonds begin to break, elastic strain energy is converted to heat, and the strain is no longer totally reversible.

The Flow of Energy During Fracture

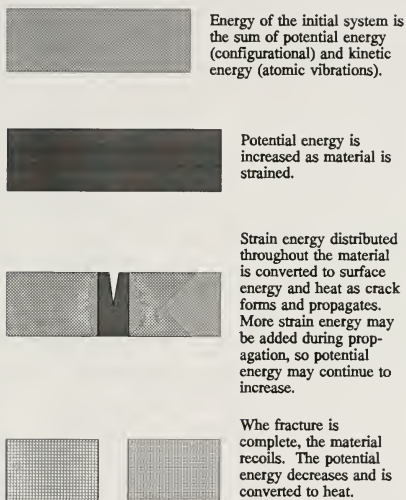


Figure 4-25. Schematic showing the flow of energy in a brittle material system during strain-to-failure.

Examination of potential energy as a function of strain for low cristobalite under isothermal fracture at various strain rates as shown in figure 4-26 reveals an interesting trend. The difference between the initial potential energy and the final potential energy is dependent on the strain rate, with the largest difference occurring at the highest strain

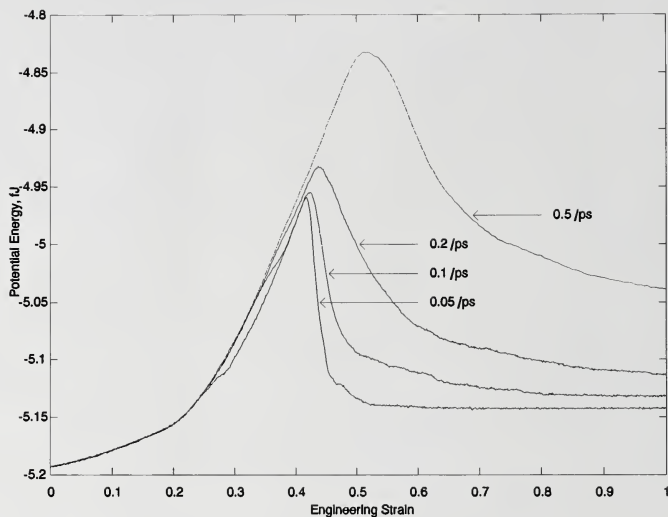


Figure 4-26. Potential energy as a function of strain for low cristobalite as modeled by the Soules potential function under isothermal strain at various strain rates.

rate. After fracture has occurred, elastic strain energy has been relieved, and differences in the potential energy are based solely on the system configuration. If the structure of the bulk remains essentially the same throughout fracture, then the increase in potential energy is a result of the surface creation during fracture. Since we find that this difference is strain rate dependent, this implies that the surface structure is dependent on the rate of strain during which fracture occurred.

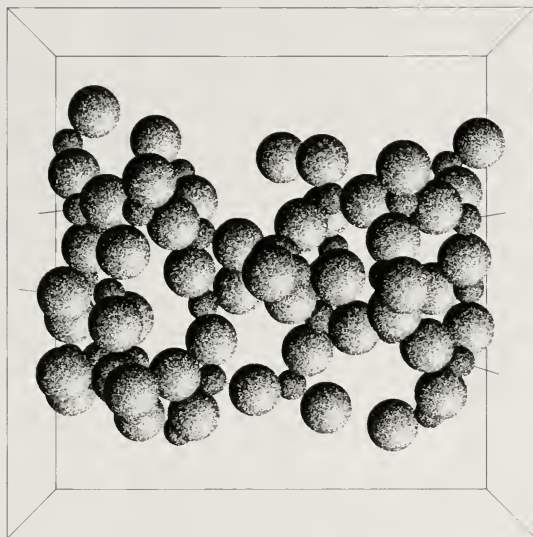


Figure 4-27. Normal view of a shallow slice of a surface created during the fracture of low cristobalite as modeled by the Soules potential under isothermal conditions at 0.05 ps^{-1} strain rate. The failure of the slice to fill the entire area is a consequence of the roughness of the surface.

Fracture surfaces

Contrary to what one might expect from a perfect crystal strained normal to a low-order plane, the surfaces resulting from fracture of cristobalite are not smooth, as

is shown in figure 4-27 for a cristobalite sample modeled by the Soules potential and strained at 0.05 ps^{-1} . Symmetry would suggest that fracture should follow a crystallographic plane. Fracture of that type would be cleavage, and although some crystals exhibit cleavage along some fracture planes, the mechanics of cleavage are not straightforward. Cleavage is essentially a low-energy fracture process that is initiated at a surface in tension. Whether or not cleavage can occur along a 100 plane in cristobalite is not addressed by these simulations because there are no surfaces available for the initiation of a cleavage crack and too much mechanical energy is added to the sample before fracture occurs. This high energy fracture results in energetic surfaces that are not atomically smooth. We do see, however, that fracture approximately follows a set of crystal planes that are not normal to the direction of strain at the lowest strain rates. In order to maintain periodic boundary conditions, the fracture must follow a zig-zag path across the MD cell.

As implied by the system thermodynamics, we also find that the surface structure is strain rate dependent. Figures 4-28 and 4-29 show remnants resulting from fracture experiments at 0.05 ps^{-1} and 0.5 ps^{-1} strain rates, respectively. We see that in general, the surface roughness increases with increasing strain rate. This supports the thermodynamic result of increasing configurational energy with increasing strain rate, as it is expected that the rougher and more disordered surfaces also possess the highest configurational potential energy.

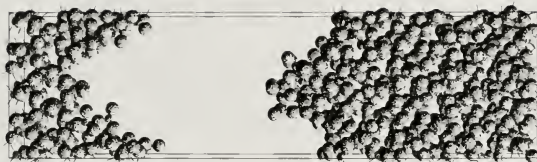


Figure 4-28. Side view of surfaces created during the fracture of low cristobalite as modeled by the Soules potential under isothermal conditions at 0.05 ps^{-1} strain rate.

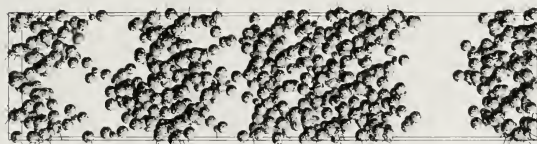


Figure 4-29. Side view of surfaces created during the fracture of low cristobalite as modeled by the Soules potential under isothermal conditions at 0.5 ps^{-1} strain rate.

One should also note that there appears to be a predominance of oxygen atoms on the fracture surface. A question that arises is whether or not this is a significant effect.

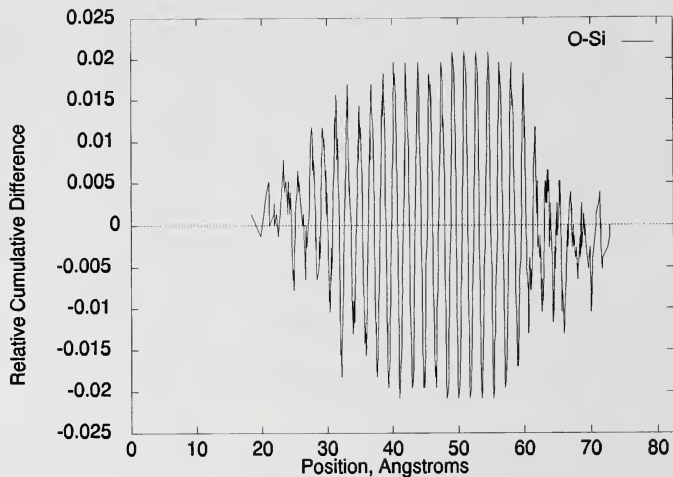


Figure 4-30. Relative abundance of oxygen and silicon atoms in slices along the length of the cell perpendicular to the direction of strain. Values plotted are the predominance of oxygen over silicon.

Oxygen atoms, with an ionic radius of 1.46 \AA , will always fill a much larger percentage of the area of a slice taken through a material than silicon atoms, with an ionic radius of 0.38 \AA . Thus, with no bias, it will always appear that there are more oxygen atoms on a surface than silicon atoms. What we really want to know is whether there is a bias towards placing oxygen atoms on the surface. We examine the location of atom centers. If we look at the relative predominance of oxygen centers to silicon centers along slices of the fractured sample, we would expect to find an oxygen rich

region near the fracture surfaces. However, we see this only to a small degree, as is shown in figure 4-30. The problem is that thickness of the surface roughness region is greater than the thickness of the possible oxygen enrichment region, resulting in blurred, at best, results.

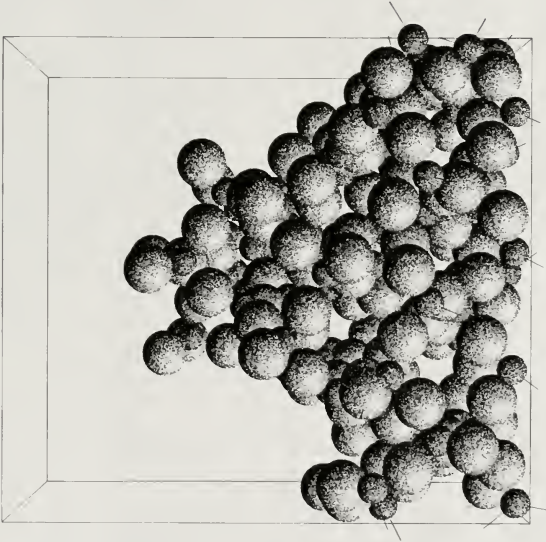


Figure 4-31. Close-up side view of surface created during the fracture of low cristobalite as modeled by the Soules potential under isothermal conditions at 0.5 ps^{-1} strain rate.

If we consider an oblique view of the fracture surface as shown in figure 4-31. we find that there appears to be a predominance of oxygen atoms hanging on dangling bonds, whereas silicon atoms appear to be sucked back into the structure by multiple bonds. It seems clear from this that oxygen atoms are preferred for under-coordination as compared to silicon atoms.

Vitreous Silica

Fracture experiments performed on vitreous silica were made to parallel those performed on low cristobalite. Samples of vitreous silica were strained to fracture at the same range of strain rates as was performed for low cristobalite, and both isothermal and adiabatic experiments were performed.

Stress-strain curves

The stress-strain curves for vitreous silica shown in figures 4-32 and 4-33 have some similarities to the stress strain curves for low cristobalite. As with low cristobalite, the start of the stress-strain curve for the F-G potential does not start at zero, but is displaced to a compressive stress. Because of this, analysis of the fracture of vitreous silica simulated by the F-G potential is not straightforward, and most of the analysis to be presented will be based on the Soules potential. Note that in the case of vitreous structures, variations in tetrahedral symmetry are less important to failure since there are more significant structural variations present, as evidenced by the broadened ring-size distributions. In this case, the covalent nature of the F-G potential plays a negligible role.

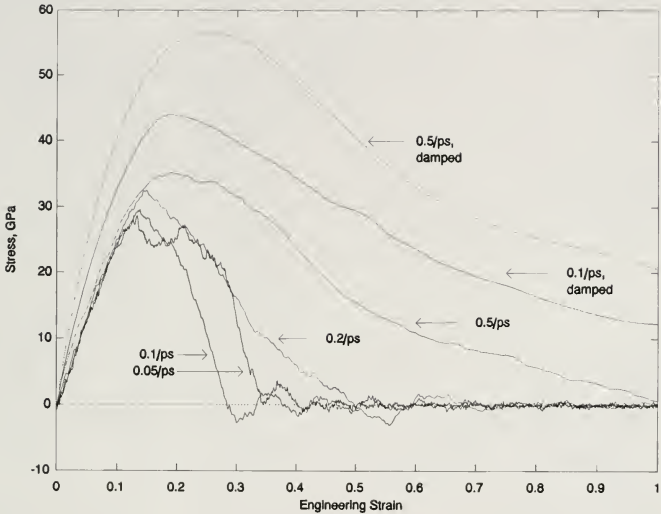


Figure 4-32. Comparison of stress-strain curves at various strain rates for vitreous silica as modeled by the Soules potential.

It is noted that the stress-strain curves for the vitreous silica samples simulated by either potential show a strong strain rate dependence for strain rates above 0.5 ps^{-1} . Again, as in our discussions on cristobalite fracture, we will focus on strain rates at or below 0.5 ps^{-1} . At these strain rates, the strain rate dependence in vitreous silica is more similar to the strain rate dependence observed for the more structurally perfect cristobalite modeled by the F-G potential than for the less structurally perfect cristobalite modeled by the Soules potential, because both the stress and strain at failure are strain

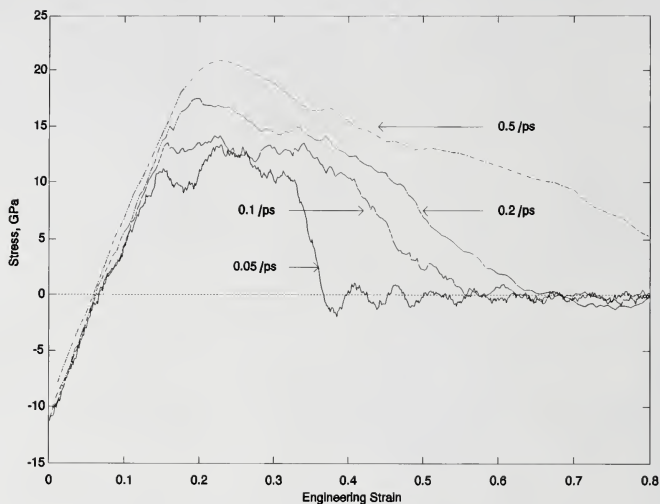


Figure 4-33. Comparison of stress-strain curves at various strain rates for vitreous silica as modeled by the F-G potential.

rate dependent. By almost any measure, vitreous silica is the least perfect structure of all, so it would seem to share less in common with the cristobalite sample modeled by the F-G potential than with the sample modeled by the Soules potential. However, the vitreous silica sample has a continuous distribution of structural variations that cause strain rate dependent failure, which compares more favorably to the distribution in the more perfect F-G cristobalite than the less perfect Soules cristobalite, even though the magnitudes of the variations are different. This is a sensible result, as thermal effects caused the variations in both--in the cristobalite, the thermal effects of the current

temperature, and in the vitreous silica sample, the thermal effects remnant from the system when it became thermally arrested.

A question that naturally arises is whether the strain rate dependence is a direct result of the limited compliance of the sample, or if it is the result of thermal vibrations that function to search configurational space and minimize system energy. Put in analogous terms of a configurational energy surface, is the strain rate limitation the result of the time that the system takes to directly "roll down the hill" on a configurational energy surface, or is it the result of the time it takes to rock the system out of local "gullies" in that surface. Because the system with which we are working is modeled as masses on springs, it has a characteristic relaxation time that is related to the thermal vibration period, so the characteristic times for both possible processes should be similar. Thus, to ensure that we ascribe the strain rate dependence to the proper process, we need to perform a simulation that can differentiate between the two processes. Two such simulations were performed.

The first simulation is based on the assumption that particles displaced from their local equilibrium positions will, on average, experience a greater force than particles that remain close to their local equilibrium positions. If a strain rate is applied that causes particles to be displaced from their local equilibrium positions, then the average force on the particles should increase. The distribution of forces on the constituent particles of a system under strain at various strain rates was examined, and the results are shown in figures 4-34 and 4-35. It is found that the force distribution narrows as strain is applied, at all strain rates. This was an unexpected result based on the assumptions made above,

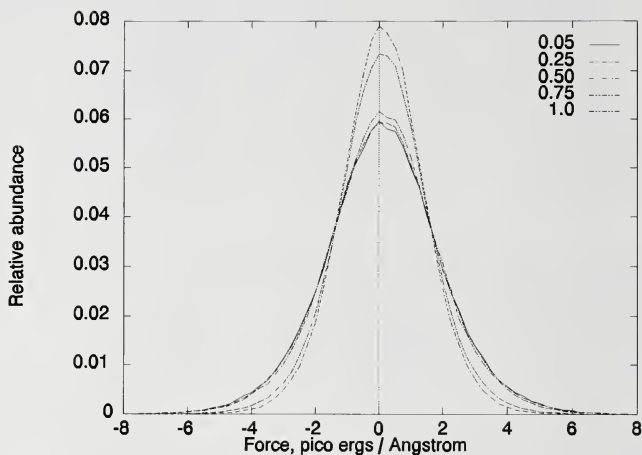


Figure 4-34. Distribution of forces on the atoms comprising a vitreous silica sample under strain at 0.05 ps^{-1} strain rate. Various curves represent different engineering strains.

but is explained by considering the shape of the effective potential well in which each particle is constrained. As the sample is strained, the width of the potential well increases, and the slope of the sides of the potential well decreases. Because particles in a system at non-zero absolute temperature have a kinetic energy component, the particles experience roughly the average force represented by the slopes of the sides of the well for heights less than the average kinetic energy. Thus, the average force on the particle decreases with strain, as long as the strain does not displace the particle beyond its constrained well.

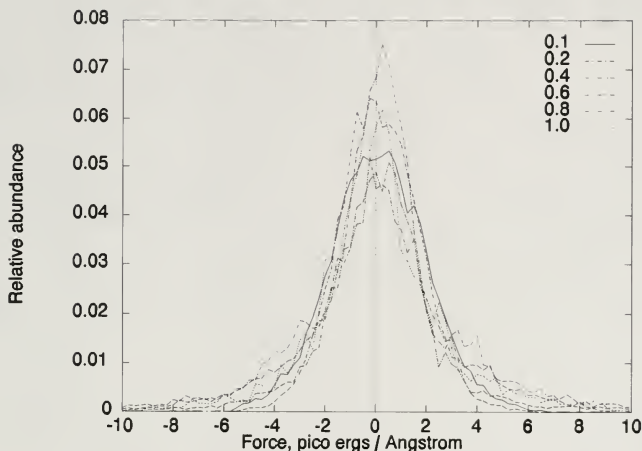


Figure 4-35. Distribution of forces on the atoms comprising a vitreous silica sample under strain at 5.0 ps^{-1} strain rate. Various curves represent different engineering strains.

Does this result *prove* that the strain rate dependence is an effect of thermal vibrations and not just a limitation of compliance? Probably not, because even slightly out of equilibrium, the walls of the potential wells that particles experience may be shallower. This result shows that we probably are not greatly displacing particles from their equilibrium positions, but it still does not directly identify the role of thermal vibrations.

In order to identify the role of thermal vibrations, a second type of simulation was performed. In this simulation, an artificial damping force was applied to each particle.

An attempt was made to choose a damping force of the proper magnitude to provide critical damping, so that thermal vibrations could be eliminated with a minimal impact on the compliance of the sample. The results of strain experiments performed with damped particle motions are shown in figure 4-32. It is seen that the act of damping particle motions results in a large effect on the stress-strain curve. If we assume that this is not an artifact of the decreased compliance resulting from the damping force, this indicates that thermal vibrations do indeed play an important role in the relaxation process implied by the strain rate dependence. However, even the damped systems are not totally strain-rate independent. The strain rate dependence of the damped stress-strain curves in turn show that the systems are compliance limited as well when strained at the higher strain rates.

The end result is that the strain rate dependence of the stress-strain curves, or of fracture in general, is the result of two effects. At the highest strain rates, it is the result of the limited compliance of the system. At lower strain rates, it is the result of relaxation processes mediated by thermal vibrations. This is an important result. This suggests that the path of fracture will ultimately be dependent on the thermal vibrations of atoms within a sample as well as elastic wave propagation.

Energetics of fracture

As in the cristobalite case, an examination of the system energetics, shown in figures 4-36 and 4-37, tells us something about the thermodynamics of fracture. Again, energy is added as mechanical strain energy, and is stored in the system as elastic strain energy or is converted to heat. However, unlike the case of cristobalite where almost

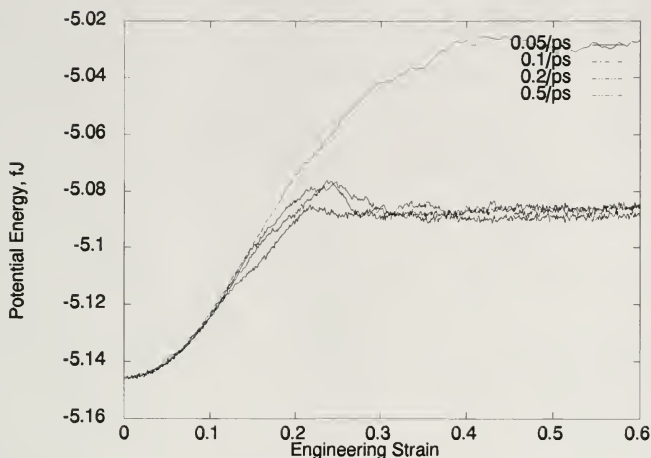


Figure 4-36. Potential energy as a function of strain for vitreous silica as modeled by the Soules potential function under adiabatic strain at various strain rates.

all the added energy is stored as elastic strain energy until the point of failure is reached, part of the potential energy is converted to kinetic energy even during the early stages of strain. This occurs because certain parts of the structure are unstable with respect to strains that would be purely elastic in the low cristobalite structure.

This investigation of the system energies during fracture shows why the point of fracture and the point of failure are not the same in vitreous silica. Fracture begins when the first bond breaks, and ends when no bonds bridge between opposing surfaces. In vitreous silica, this process may occur over an extended period because much of the strain energy added is used in re-ordering the structure and is not stored in the structure

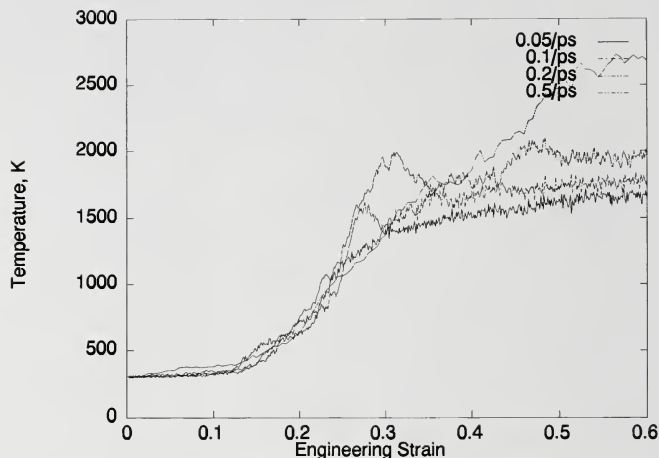


Figure 4-37. System temperature as a function of strain for vitreous silica as modeled by the Soules potential function under adiabatic strain at various strain rates.

as recoverable elastic strain energy that can drive the fracture process to completion. Thus, the small vitreous silica system must be driven to fracture by the continued application of strain. As the sample becomes more compliant from the breakage of bonds within the network, the amount of strain that must be applied to cause fracture increases. The path by which fracture in vitreous silica takes place is complex, and the possibilities will be addressed in the analysis section.

A strain rate dependence on the change in the system configurational potential energy during fracture under isothermal conditions is also observed for vitreous silica

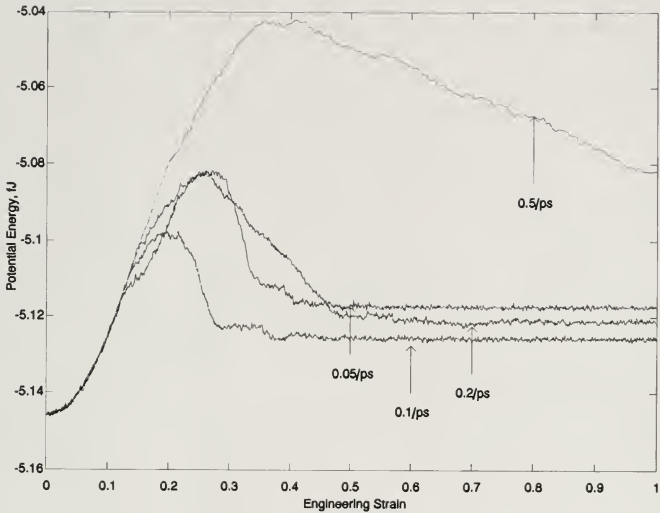


Figure 4-38. Potential energy as a function of strain for vitreous silica as modeled by the Soules potential function under isothermal strain at various strain rates.

samples, as is shown in figure 4-38. In all cases, the change in the configurational potential energy is less for vitreous silica than for cristobalite. This results from the fact that the structure of vitreous silica already lacks order, so a disordered surface does not cost as much as the disordered surface of cristobalite in terms of configurational potential energy.

Structural changes during strain-to-fracture

The structural changes that occur during strain-to-fracture are dependent on the strain rate to which the system is subjected. In comparisons of structural characteristics, we find that the systems strained at the highest strain rates show the effects of strain most definitely in the pair-correlation and bond-angle distribution functions. The structures strained at lower strain rates showed little change in structural distribution functions at 0.2 engineering strain despite the fact that the structure had to somehow conform to the strain. Identifying where the strain altered the structure was a challenge that we sought to undertake.

The O-Si pair correlation functions for the structures at 0.2 strain show that the O-Si bond is elongated under tensile strain. A comparison of the Si-O first peak of the unstrained structure to the structure strained at various strain rate is shown in figure 4-39. We see that there is minimal displacement of the peak in the structures strained at 0.05 ps^{-1} and 0.5 ps^{-1} , but that there is a much larger displacement of the peak in the structure strained at 5.0 ps^{-1} .

In a similar comparison of the Si-Si first peaks shown in figure 4-40, we again find that all peaks undergo a shift to larger distances when the sample is strained. Also, we find that there is minimal displacement of the peaks in samples strained at 0.05 ps^{-1} and 0.5 ps^{-1} , with a larger displacement observed for the sample strained at 5.0 ps^{-1} .

These findings indicate that although the samples are strained to the same total strain, the strain is distributed differently in the structures strained at different rates. Although all the samples are strained to the same degree, it appears that the structures

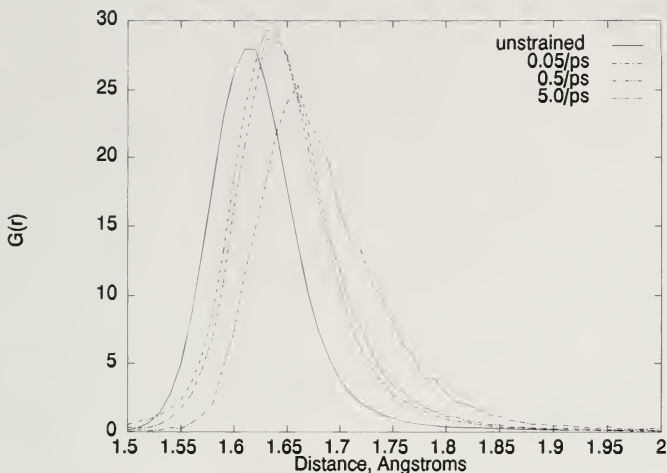


Figure 4-39. Si-O pair correlations in vitreous silica. Comparisons between unstrained and strained to 0.2 at various strain rates are made.

strained at the highest strain rates possess the highest apparent strain. The question then arises, *where does the strain go in the structures when strained at different strain rates?*

A comparison of O-Si-O bond angles in the unstrained structure to bond angles in the strained structure is shown in figure 4-41. We see that the largest deviations in these bond angles result when the structure is strained at the highest strain rate of 5.0 ps^{-1} , while the effects on the bond angles at the lower strain rates of 0.5 ps^{-1} and 0.05 ps^{-1} are smaller and nearly equivalent. This indicates that tetrahedra are distorted at the

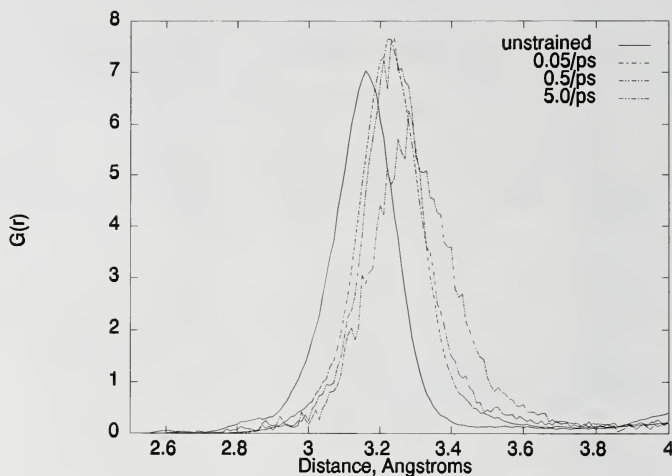


Figure 4-40. Si-Si pair correlations in vitreous silica. Comparisons between unstrained and strained to 0.2 at various strain rates are made.

highest strain rates, but some other mechanism is active in the expansion of the structure at lower strain rates.

A comparison of Si-O-Si bond angles in the unstrained structure to the structure expanded at various strain rates is shown in figure 4-42. In this case, we see a non-monotonic behavior with strain rate. The distribution obtained from the structure strained at a strain rate of 0.05 ps^{-1} shows the smallest change from the unstrained structure. The structure strained at 0.5 ps^{-1} shows a much greater change in this

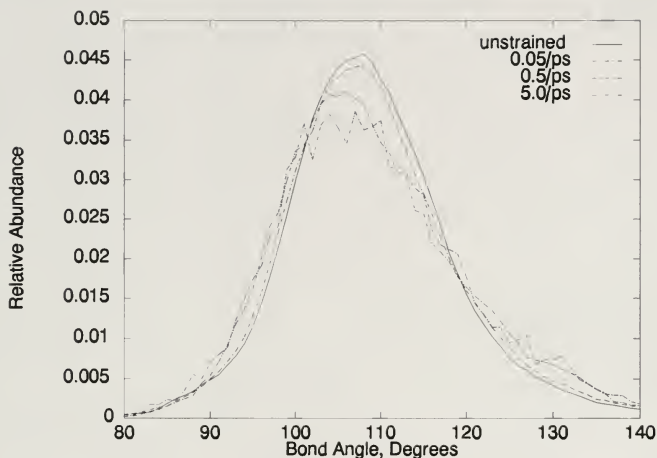


Figure 4-41. O-Si-O bond angle distributions in vitreous silica. Comparisons between unstrained and strained to 0.2 at various strain rates are made.

distribution, with bond angles significantly skewed towards 180° . However, the distribution obtained from the structure strained at 5.0 ps^{-1} shows an intermediate effect.

The bond angle distributions indicate that strain goes into the structure strained at 0.5 ps^{-1} by rotating tetrahedra with respect to each other in order to cause a change in the structure so that strain is accommodated with minimal change in bond lengths, but we still have to find where strain goes in the structure strained at 0.05 ps^{-1} . In order to find out what happens to the structure strained at 0.05 ps^{-1} , we must invoke higher order structural characterizations, specifically, ring size distributions and free volume sphere distributions.

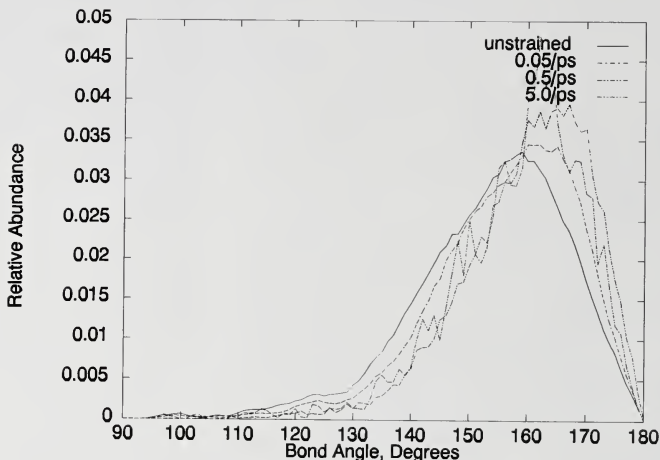


Figure 4-42. Si-O-Si bond angle distributions in vitreous silica. Comparisons between unstrained and strained to 0.2 at various strain rates are made.

Comparisons of ring size distributions are shown in figure 4-43. We see a general increase in the size of rings when the sample is strained to 0.2. The abundance of three- and four-membered rings decreases noticeably, indicating that these small rings are particularly unstable under strain. The decrease in the number of five-membered rings is strain rate dependent, with the smallest decrease occurring for the structure strained at 0.05 ps^{-1} , and the largest decrease occurring for the structure strained at 5.0 ps^{-1} . For six-, seven-, and eight-membered rings, the relative abundance of each is greatest for the structure strained at 5.0 ps^{-1} and the least for the structure strained at

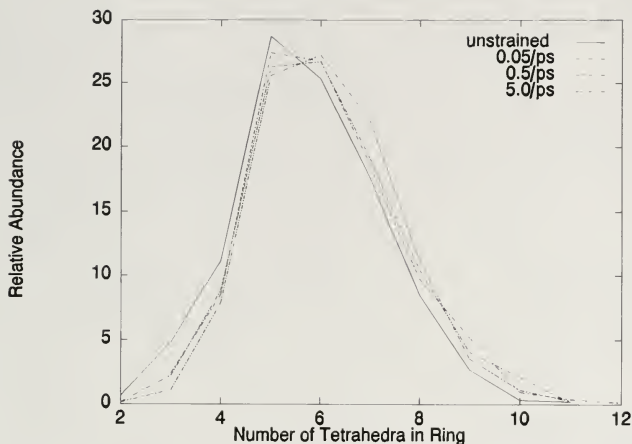


Figure 4-43. Comparison of ring size distributions of vitreous silica strained to 0.2 at different strain rates.

0.05 ps⁻¹. Beyond eight-membered rings, the largest abundances tend to go towards the lower strain rates.

Perhaps the easiest way to see the effects of strain on the ring size distribution is to plot the changes in this distribution when it is placed under strain, as is shown in figure 4-44. We observe that there is a loss in the number of small rings and an increase in the number of large rings. The change in the number of small rings, having less than six tetrahedral members, is most extreme at the highest strain rate, and is the least significant at lowest strain rate. The larger rings can be divided into two groups -- those having less than eight members, and those having eight or more members. It is observed

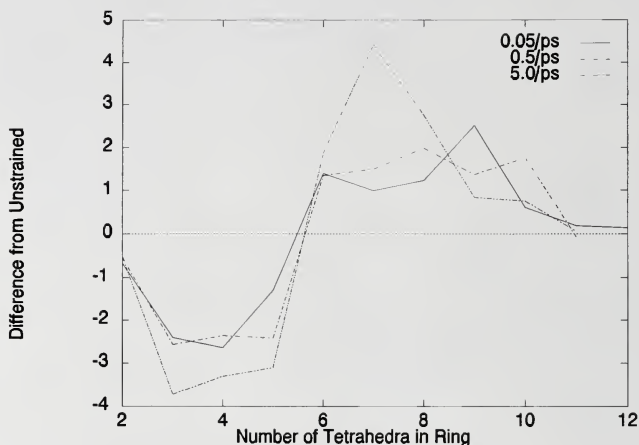


Figure 4-44. Change in the abundances of rings of various sizes during strain to 0.2 in vitreous silica at various strain rates.

that the increase in the number of larger rings is, for the most part, limited to the first group at the highest strain rate, but is spread evenly between the two groups at the lower strain rates, meaning that there are some very large rings being formed at the lower strain rates. Ring size has been used to provide a topological indicator of the density of the structure, by assuming that within each ring there exists a void, implying that structures with larger rings contain larger voids. Thus, this gives us some indicator of where the strain is going when added to a vitreous silica structure at a lower strain rates.

If strain is going into the formation of voids, then the most direct method of observing this is by the use of the free volume sphere analysis. Because of the

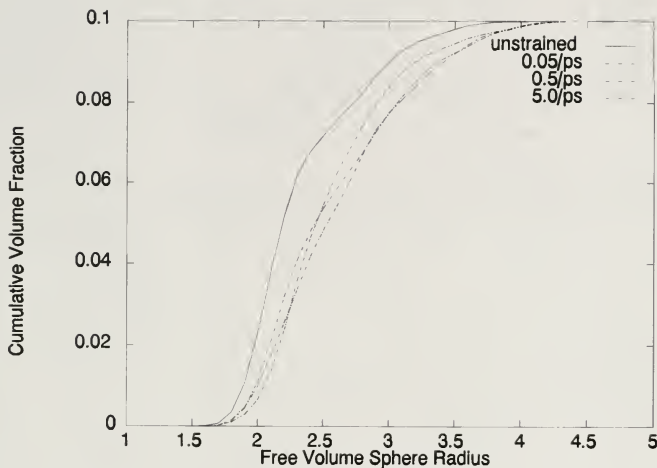


Figure 4-45. Free volume sphere histogram--the integral of the free volume sphere distribution--for vitreous silica strained to 0.2 strain at various strain rates.

uncertainty in this type of calculation, the results of the free volume sphere analysis are seen most clearly by integrating the distribution, to create sort of a histogram, as shown in figure 4-45. This elicits a comparison to the presentation of data in particle size distributions. Such a presentation allows one to see where contributions are made to the distribution in a general sense, which suits our purposes here. We observe that all strained structures are composed of larger free volume spheres than the unstrained structure. We see that about 70% of the volume is contained by spheres of radius less than 2.25 Å in the unstrained structure, whereas only about 40% of the volume of the

strained structures fall in spheres in the same range. We also see that there is a difference in the distribution dependent on the strain rate. Initially, at a free volume sphere radius of about 2 Å, the function increases the most at the lowest strain rates. However, at a free volume sphere radius of about 2.25 Å, the function corresponding to the highest strain rate surpasses the functions for the lower strain rates, indicating that the smaller intrinsic spheres are stretched in this structure. At a free volume sphere radius of about 3 Å, the function corresponding to the highest strain is by far the greatest, with the function corresponding to the lowest strain rate being the smallest. As all curves are normalized, they must all end at unity. Thus, there must be a predominance of the largest free volume spheres at the smallest strain rates. This indeed indicates that strain is distributed into large voids in the vitreous silica structure when strained at the lowest strain rates.

Finally, we consider the structural defects present in the structures during strain-to-failure. Although we see differences in the numbers of defects in the structures strained at different strain rates, there is no easy way to describe the trends observed. We note that both the structures strained at 0.05 ps^{-1} and 0.5 ps^{-1} have a lower percentage of four-coordinated silicon atoms, as would be expected in a strained structure. However, we also note that the structure strained at 5.0 ps^{-1} has an increased number of four-coordinated silicon atoms with respect to the unstrained structure. However, by all previous structural correlations, we find this structure to be the most modified. We also note that the largest structural change in any structure is the decrease in the number of five-coordinated silicon with an increase in the number of three-coordinated silicon

Table 4-2

Coordination of species in simulations of vitreous silica at 0.2 strain and various strain rates as found by the ring statistics program.

| Coordination | Predominance of Configuration | | | |
|--------------------|-------------------------------|-----------------------|----------------------|----------------------|
| | Unstrained | 20% Strain | | |
| | Melt, Cool | 0.05 ps ⁻¹ | 0.5 ps ⁻¹ | 5.0 ps ⁻¹ |
| Silicon by Silicon | | | | |
| 1 | 0.00 | 0.00 | 0.00 | 0.26 |
| 2 | 0.00 | 0.78 | 0.52 | 0.26 |
| 3 | 0.52 | 11.20 | 14.84 | 9.64 |
| 4 | 86.98 | 84.90 | 82.29 | 88.54 |
| 5 | 9.64 | 2.86 | 1.82 | 1.04 |
| 6 | 2.60 | 0.26 | 0.52 | 0.26 |
| 7 | 0.26 | 0.00 | 0.00 | 0.00 |
| Silicon by Oxygen | | | | |
| 1 | 0.39 | 3.13 | 4.04 | 2.60 |
| 2 | 97.53 | 96.48 | 95.57 | 97.27 |
| 3 | 2.08 | 0.39 | 0.39 | 0.13 |

atoms. The decrease in the number of five-coordinated silicons is directly proportional to strain rate, which is not a totally unexpected result, as the over-coordination defects are the least stable in the structure that displays the most tensile strain. However, the change in the number of three-coordinated silicons is more difficult to explain. It appears that the appearance of under-coordinated silicons is indicative of some kind of reconstruction process. At a strain rate of 0.05 ps⁻¹, this reconstruction reaches a steady

state at which about 12% of the silicon atoms are under-coordinated. At a strain rate of 0.5 ps^{-1} , the steady state of this reconstruction results in about 15% of the silicon being under-coordinated, as reconstruction is forced to occur at a higher rate. However, at the strain rate of 5.0 ps^{-1} , this reconstruction process does not appear to be active, thus there is a decreased number of under-coordinated silicon atoms at this strain rate, only about 10%, even though the number of over-coordinated silicon atoms is the smallest at this strain rate.

From structural characteristics ranging from displacement of pair correlation functions to differences in the coordination of silicon atoms, we see that the vitreous silica structure responds to strain in different ways depending on the strain rate. We see that the structure attempts to accommodate strain by some local structural rearrangements at low strains, and that the structure merely expands at the highest strain rates simulated with no rearrangement. This indicates that the rate of strain may play an important role in fracture.

Viscous Flow

A 288 atom system modeled by the Soules potential function was put under shear strain. The appropriate shear stress tensor for systems at various shear strain rates and temperatures are shown in figures 4-46 and 4-47. Because the variations in shear stress as a function of time for each sample are greater than the differences between the curves, curves corresponding to the average over an interval from the start of the experiment to the point are plotted. Although the shear stress undergoes large fluctuations during shear

Table 4-3

Viscosities of vitreous silica as modeled by the Soules potential at various temperatures and strain rates, in units of 10^{21} Pa·s.

| Temperature, K | Strain Rate, ps ⁻¹ | | | |
|----------------|-------------------------------|------|-----|-----|
| | 0.1 | 0.4 | 2.0 | 8.0 |
| 1200 | | 30.0 | | |
| 2000 | | 27.5 | | |
| 4000 | | 22.7 | | |
| 5000 | 60.0 | 18.7 | 6.5 | 2.6 |

strain, the average shear stress shows a straightforward dependence on temperature or strain rate. The viscosities of the systems under different strain rates and temperatures are shown in Table 4-3.

Figure 4-46 shows the shear stress developed during the application of shear strain at various temperatures. As expected, the shear stress at constant strain rate decreases with increasing temperature, corresponding to decreasing viscosity. However, the viscosity function of temperature is not as expected from an Arrhenian-type activation process. When we fit the data to an exponential function, we get the relationship --

$$\eta = \left(-36.81 \times \exp\left(\frac{-6205}{T}\right) + 29.87 \right) \times 10^{21} \text{ Pa} \cdot \text{s} .$$

By an Arrhenian-type analysis for shear flow, the factor in the exponent would imply, a negative activation energy, the pre-exponential factor would imply a negative number of activation sites, and the added scalar would imply that the process is not a fully activated process. Thus, we conclude that the viscosity of these systems is not

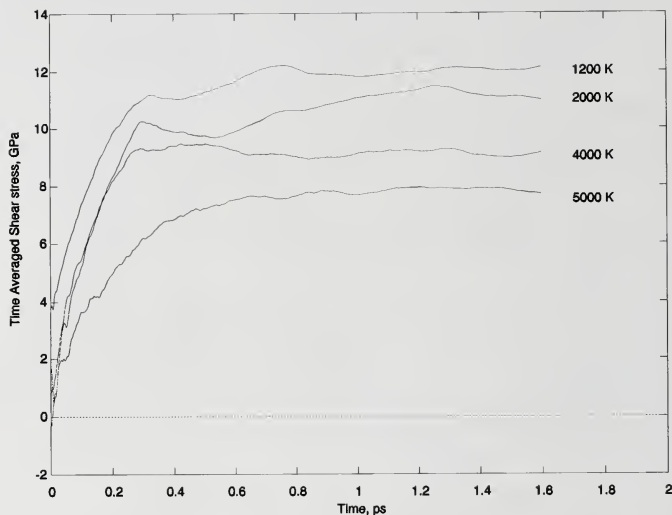


Figure 4-46. Shear stress as a function of time for a vitreous silica sample as modeled by the Soules potential function at various temperatures.

Arrhenian. A complementary description of the system may be more valid. Assume that shear flow is *blocked* by bonds that may break when thermally activated. Because we apply shear strain, we break any blocks to shear flow that exist in the sample, no matter what stress is required to do so. At low temperatures, the shear stress that results is nearly the maximum that the sample can support assuming no thermal activation of blocking bonds. As the temperature is increased, the blocking bonds are thermally broken, and the shear stress decreases accordingly. Such a mechanism would lead to a

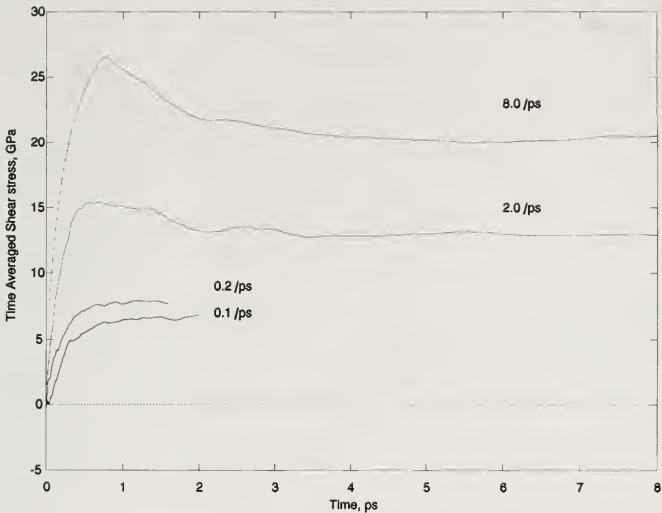


Figure 4-47. Shear stress as a function of time for a vitreous silica sample as modeled by the Soules potential function at various strain rates.

zero, not finite positive, viscosity at infinite temperature where no blocking bonds could exist. An analysis of the viscosity function reveals that the viscosity of the sample goes slightly negative at an infinite temperature, not physically realistic, but not bad considering that only four data points were used to find the viscosity function of temperature. This process is contrasted to the mechanism assumed to be active in viscous flow using the Nernst-Einstein equation because in that model, viscous flow is related to diffusion, and occurs by a process similar to dislocation motion, whereas in

this model, shear flow is limited by any intact bonds. A major difference between the two models is the strain rate at which each is active. Shear flow as described by the Nernst-Einstein equation is a low shear rate process--correlation of dislocations is not necessary. At high strain rates, correlation of dislocations becomes important, as diffusive motion alone is not sufficient to propagate the structural rearrangements required for shear at high rates. Thus, the Nernst-Einstein equation loses applicability at high strain rates.

We also find in figure 4-47 that shear stress increases with shear rate. However, shear stress does not increase linearly with shear rate as in an ideal Newtonian fluid, but undergoes shear thinning, where the apparent viscosity is decreased with increasing shear rate. Shear thinning has been shown to exist in Lennard-Jones systems modeled using molecular dynamics, and a layering mechanism is proposed to explain this behavior, where slip planes are formed such that the majority of shear can take place with a minimum disruption of structure. Although we observed no layering in this system, it was evident that at high strain rates, most of the tetrahedral units in the system were in a state of transition such that continued rearrangement of bonding could be accomplished with minimal further activation. It is possible that a larger system may have displayed evidences of layering, but the small size of the simulated system prevented the formation of distinct layers.

Determinism in Fracture

We have investigated the underlying structure of a systems to be fractured. We have observed the stress-strain curves of the systems during fracture, and have studied the structural changes that occur during the fracture process. In all, we have painted a clear picture of the processes occurring during the fracture process. If one is capable of predicting the path of fracture through a material sample, we should have a good handle how this prediction should be made. However, as much as we are able to describe the fracture process with words, plots, and equations, we still observe complex behaviors during fracture that cannot be described in terms that are any simpler than the simulation program, the simulation parameters, and the exact starting conditions used to perform the simulation. We are unable to predict the fracture path in a simulated sample using any lesser description. Since such a description invokes a system of non-linear equations, we cannot even predict the resulting change that a small change in initial conditions makes. In order to demonstrate this sensitivity on initial conditions, we performed a series of simulations in which small changes in initial conditions were made, and the varying results were noted.

Reproducibility and Accuracy of Computer Simulations

The reproducibility of the simulations was investigated by performing simulations of fracture using the same set of initial conditions, the same executable code, and the same integration algorithm, on the same computer system. It was found that identical

results were obtained. This provides verification of the reproducibility of the simulations.

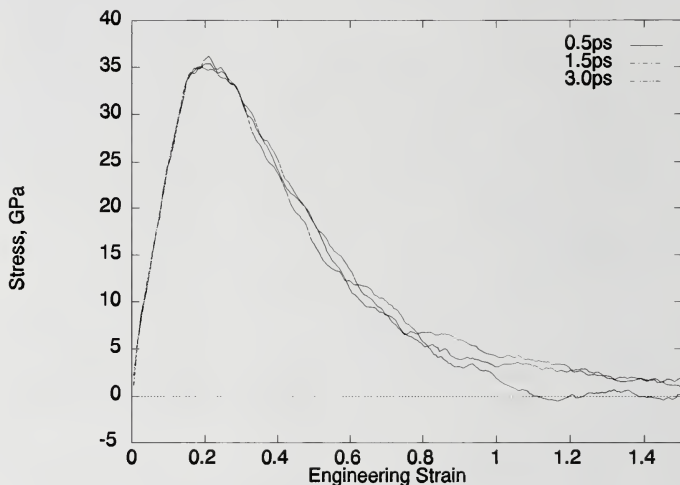


Figure 4-48. Stress-strain curves for nearly identical systems after various anneal times.

Variation in Anneal Times

After the formation process by which a high temperature structure was cooled to 300 K, samples were annealed for either a 0.5 ps, a 1.5 ps, or a 3.0 ps interval prior to straining. With the exception of statistical fluctuations, system total energies and pressures remained constant. This indicates that the systems are in quasi-thermal

equilibrium at 300 K. The samples were then strained at a rate of 0.5 ps^{-1} for 3 ps. The stress-strain curves from the strain experiments are shown in figure 4-48. The stress-strain behavior, as reported previously, was found to consist of an elastic regime in which the stress increased monotonically and nearly linearly with strain, a yield or stress relaxation region in which the stress peaked and became independent of strain and a fracture region in which the stress decreased rapidly with strain.

Clearly, in each case, the strain was applied to a slightly different microscopic structure, as modified by thermal vibrations, yet the stress-strain behavior during the elastic straining period is essentially the same for all three samples. This result supports the expectation that during elastic straining, the behavior of the material is independent of the perturbations in individual particle positions and insensitive to their individual response. However, as the yield region is entered, and the sample begins to fail, each sample follows a distinctly different path. This region is characterized by the breaking of internal bonds and irreversible structural changes. Here, the behavior of the ensemble becomes sensitive to the initial structure at the time of strain application. Small differences in the microscopic structure can have profound effects on the selection of a fracture path.

We previously found that the fracture process, at the atomic scale, and under a uniform strain, proceeds by a coalescence of voids that have grown disproportionately under the applied strain. It appears, here, that this void growth is sensitive to the local structure and that this sensitivity is observable in the macroscopic stress-strain response of the material.

No correlation is observed between the length of the anneal time and either yield response or fracture stress.

Round-off Errors

Stopping and re-starting a simulation results in a loss of precision as binary values stored in memory with 15 (equivalent decimal) significant figures are converted to a decimal representation and written to a file with 6 decimal significant figures, then subsequently reconverted to a binary representation of 15 (equivalent decimal) significant figures when the simulation is re-started. Such an operation results in an uncertainty of about $O(10^{-5})$ in positions relative to the length of an Si-O bond and of $O(10^{-2})$ in velocities relative to the average velocity. Thus, stopping and re-starting simulations provides us with the opportunity to study the effects of round-off error on the outcome of a simulation.

Three simulations consisting of a 2 ps anneal followed by a 3 ps strain at a 0.5 ps^{-1} strain rate were performed. In the first simulation, the system was annealed and strained without stopping. In the second, the simulation was stopped and re-started midway through the anneal period. In the third, the simulation was stopped and re-started between the anneal and the strain periods. The results are shown in figure 4-49.

Approximate reproducibility was again observed during the elastic portion of the strain, while significant deviations occurred in the regions of yield and failure. This shows that while a discrete round-off error does not greatly influence the behavior of the

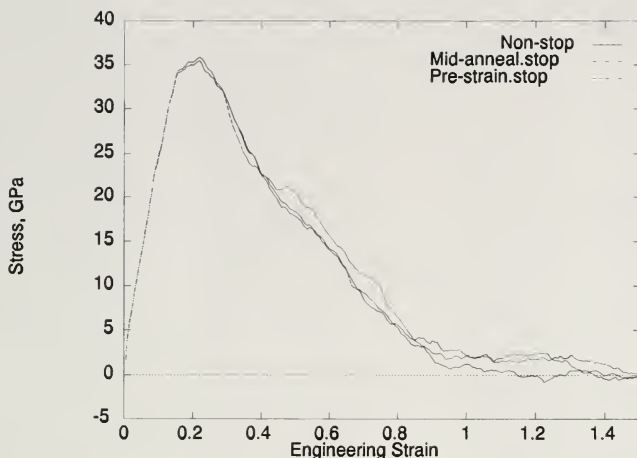


Figure 4-49. Stress-strain curves for nearly identical systems differing by a loss of precision resulting from truncation of system conditions at various times.

system under annealing or linear elastic conditions, neither is the effect of this error diminished under these conditions.

"Butterfly Effect"

In two simulations, a single oxygen atom was slightly displaced along the direction of strain. The amount of displacement was 0.0085 angstroms, which is 0.5% of a Si-O bond length, or about 8.5% of the span of an atomic thermal vibration. In the first simulation, the displacement was made directly before straining. In the second, the displacement was made prior to a 3 ps anneal, and then the system was strained. In both

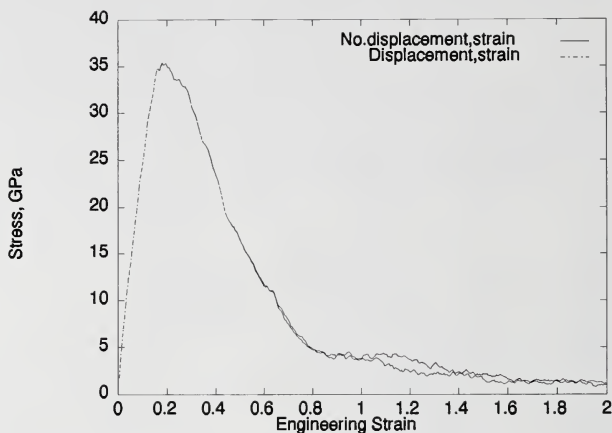


Figure 4-50. Deviations from stress-strain curves resulting from a displacement of one atom immediately before straining.

simulations, the effect of the small displacement of the oxygen atom is at first far less significant than the effect of either changing the annealing time or introducing a discrete round-off error. A comparison of the results of the two simulations, shown in figures 4-50 and 4-51, respectively, reveal that significant deviations in the stress-strain curves occur sooner when the sample was annealed after the displacement before applying strain, indicating that although the effects of the change in the behavior of the system are small during annealing, propagation of the change occurs with time nonetheless. This indicates that the consequence of a seemingly insignificant displacement of a single atom of the ensemble is a change in the behavior that grows with time.

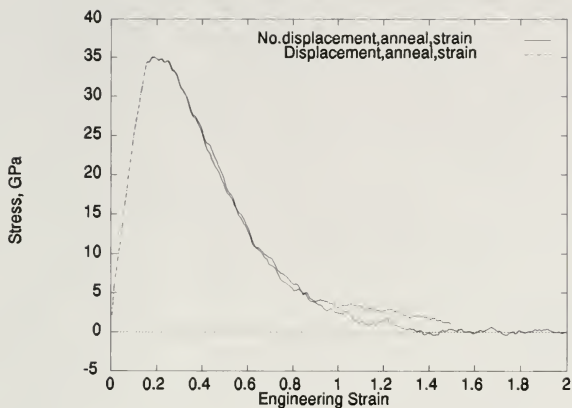


Figure 4-51. Deviations from stress-strain curves resulting from a displacement of one atom before an anneal period prior to straining.

Sensitivity on Simulation Artifacts

The accuracy of the simulations was investigated by performing the simulations using two different integration algorithms. It was found that the different algorithms resulted in simulations giving similar, but not identical, results. This is to be expected in a chaotic system, and indicates that simulations using either algorithm are reasonably accurate.

The results were insensitive to the use of either the Verlet or Gear algorithms, to the application of strain at a lower strain rate of 0.1 ps^{-1} , and to the origin of the 12000

K melt used in sample formation. This indicates that our results are general and are not the result of specific aspects of our simulations.

CHAPTER 5 ANALYSIS

Models of Silica

The analysis of a simulation always goes back to the question *how do we know that your simulation shows what really happens?* It is not possible to measure accurately transient atomic-scale processes in a material that are both too small and too fast to see. However, we can make comparisons of what we see and what we know to satisfy ourselves that we either see plausible behavior or we do not.

We have used structural comparisons of our models to what is experimentally known about the structure of silica to show that our models are plausible. We admit that our model does not fit with all features known for vitreous silica. A major discrepancy of the vitreous silica models using both the Soules two-body and the Feuston-Garofalini three-body potentials is that the mean Si-O-Si bond angle is too large. This is evidenced for both potential functions in bond angle distributions that peak at about 158° as compared to the peak of 144° deduced by Mozzi and Warren, and by Si-Si first peaks in the PCF's at about 3.15 \AA as compared to about 3.05 \AA as found by neutron scattering. The result of this discrepancy on the properties of these models is that the mechanical properties that are dependent on the opening of the Si-O-Si bond angle are skewed. As we have seen that neither potential provides the correct non-linear elastic

response observed in real vitreous silica irregardless of differences in the ring-size distributions, the incorrect Si-O-Si bond angle distributions for both models may be the cause.

We have observed that although the Soules potential creates a structural model that better fits the experimental neutron diffraction model than does the F-G potential, the F-G potential creates a structure that has fewer defects. Thus, the F-G potential gives better short-range structure, but the Soules potential gives better medium-range structure. This appears to be a result of different emphases in the repulsive and attractive Coulombic potentials resulting from the use of different force truncation functions.

Because it creates a structure with fewer topological defects, the F-G potential creates a structure that has a better ring-size distribution. Three- and four- membered rings have been termed "defects" in the silica structure, and two-membered rings are too reactive to be seen at all in experiment, although they may exist transiently during the fracture of silica where there are no reactive species to break the strained bonds. The structure created by the F-G potential has fewer of all these than does the structure created by the Soules potential. The F-G potential also creates a structure that has a narrower free-volume-sphere distribution that peaks at a larger size than does the Soules potential.

The densities of the models given by the two potential functions are not the same. The Soules potential creates models that have nearly the correct density for both the cristobalite and the vitreous phases. Although both models contain Si-O-Si bond angles

that are too far open, the F-G potential also creates a model with bond lengths that are too long, while the Soules potential creates a model in which the larger bond angles may be compensated by smaller rings.

In models of low cristobalite, the Soules potential creates a structure that has a highly nonlinear elastic modulus, indicating that the Si-O-Si bond angles are too floppy when modeled by this potential. The F-G potential creates a structure that is stable during the application of strain until fracture commences, whereas the structure created by the Soules potential undergoes a symmetry-breaking transformation. However, the density of the cristobalite structure as modeled by the F-G potential is not correct, although the stress at experimentally determined lattice parameters is isotropic, whereas the overall pressure of the structure as modeled by the Soules potential is nearly zero at experimental lattice constants, but the pressure is not isotropic.

Despite all the structural differences between the two models, there are no significant differences in the fracture behavior for the two models. The major difference in fracture behavior is seen in the fracture of the cristobalite samples, and is the result of the symmetry-breaking transformation that initiates fracture in the structure modeled by the Soules potential. In the structure modeled by the F-G potential, no such transformation is observed, and fracture is initiated by a more stochastic process.

Because we are capable of critical analysis of our models, we are capable of assessing the applicability of our results. Thus, our analysis should focus on the aspects of fracture that are not the result of the discrepancies that we have noted. This leaves us much space to make some general comments about fracture.

Stress and Strain

Stress and strain are two sides of the same quantity, related by the elastic modulus. Fracture mechanics has generally used a stress description of fracture while we have used a strain approach. Because we apply strain instead of stress, this is certainly a more natural description for us.

The strain approach also provides a more fundamental quantity when describing a dynamic system. Because strain distributions cause density variations that may travel through a structure and these travelling density variations have an associated momentum, it is clear using a strain based argument that the dynamic motion of local strains and their dependence on strain rate is important. Discussions that rely on stress intensity to explain fracture surface formation do not provide the same intuition as discussions based on strain. Thus, stress intensity works fine for describing static processes such as crack initiation, but strain arguments better describe dynamic processes such as crack propagation.

Structural Changes During Strain-to-Failure

The application of strain to a material forces a change in the structure of the material--we are forcing the material to adopt a structure with a lower density or a different shape. The material may accommodate this strain by different methods.

The material first displays an elastic response where atomic bonds or atomic bond angles are strained without a change in the connectivity of the structure. Later, a displacive transformation may occur in which the symmetry of the material is changed

by the application of strain. General reconstructive transformations are not likely to occur because the simultaneous de-bonding and re-bonding of atoms in the structure under strain would cause mechanical failure between the de-bonding and re-bonding stages. However, some specific kinds of transformations that may be classified as reconstructive do occur.

Creep failure is a slowly occurring reconstructive transformation that ultimately results in fracture. Because it is reconstructive, the system tries to stay in equilibrium at all stages, resulting in the formation of nearly spherical voids within the material that cause the volume of the material to increase while minimizing the surface area between the material and the internal voids. Interestingly, creep failure in solids appears to be somewhat similar to cavitation in liquids, because both produce spherical voids within the phase under strain. In both cases, this results from the slow formation of voids with respect to the diffusive deformation of the surrounding phase, making that phase appear fluid with respect to void formation. The major difference between cavitation and creep failure is the time scale involved, and the correlation of the location of voids. In creep failure, voids are often located in the same plane perpendicular to the direction of strain because one void causes the rest of the material in its plane to undergo an increase in stress, whereas in liquids that cannot support a shear stress this is not the case as all bonds with exception of those close to the surface of voids support the same isostatic stress.

Additionally, in ductile materials, the coordination of line and screw defects results in reconstruction of the material with only a transient de-bonding and re-bonding

of atoms along a dislocation to form slip planes. Where it can occur, deformation by slip planes provides a deformation mechanism that is both easily initiated and efficient in its motion. This mechanism is responsible for the ability of ductile materials to undergo significant deformation rather than fracture under the application of strain.

Finally, when all avenues for structural deformation have been exhausted, further strain cannot be accommodated by the contiguous material, and the material fractures.

An important aspect in the structural changes that occur during strain-to-fracture is that they are strain rate dependent. We have observed in our simulations of vitreous silica that the way that the system accommodates elastic strain is dependent on the applied strain rate. At the lower strain rates, some reconstruction is possible along with the elastic strain, while at high strain rates, little reconstruction is possible so that bonds that would be reordered to avoid over-straining at the lower strain rate would be fully stretched or broken at the higher strain rates. Because the bonds are on average more stretched at the higher strain rates, they support a higher stress as well. Thus we explain the result observed in our stress-strain curves that the material seems to be stronger at the higher strain rates, while a reconstruction process is active that results in the expansion of large pre-existing voids at the lowest strain rates, as observed from our free-volume-sphere size distributions.

The concept of the strain rate dependence on the structural changes that occur in the material is common to a wide range of materials. Both metals and polymers undergo ductile-brittle transitions based on strain rate. It is based on the principle that a system will follow a path that will minimize the energy required to conform to constraints

applied to it given the time to do so. Low strain rate deformation should occur by a lower energy process than high strain rate deformation. Although the lowest energy route by which a system may conform to applied constraints may ultimately be brittle fracture, materials that can undergo ductile deformation generally lack the high strain energy required for activation of brittle fracture. Thus, the ductile-brittle transition results from the system being unable to conform to an applied strain by a slip process, increasing the elastic energy stored in the system until fracture can be initiated. Thus, although the stress is greater, the total energy required for the system to conform to the applied constraints may be less by brittle fracture than by ductile deformation.

Shear Flow

The structural changes required for shear flow in viscous materials are fundamentally different than the changes required for uniaxial strain in elastic materials. In viscous flow, strain rate refers to the steady-state rate of flow for the material, whereas in elastic materials, shear rate corresponds to a transient strain to a state of strain. Shear flow results from the cooperative reorientation of bonds to form a material with an ever changing shape. Shear flow generally results in systems where atoms are highly diffusive and an applied shear stress acts to drive the normally random motion of atoms into a correlation motion. This leads to dependencies on temperature and strain rate. Normally, these systems are highly thermally activated, so an increase in the temperature frees more atoms to be available for coordinated motions, decreasing the shear stress required to drive the system at a given shear rate. Also, at low shear rates,

the coordinated motion of individual clusters of atoms that collectively result in shear of the material is transient, so the shear stress is proportional to the shear rate, and the viscosity is constant. However, at high shear rates, these collective motions become more permanent and may effect more shear in the lifetime of the coordinated motion, so the resulting viscosity appears to decrease. This behavior is called shear thinning and is common in polymer solutions, and has been observed in silicate glasses.⁹⁵

We have observed both a temperature dependence on viscosity and shear thinning in our simulations. However, the temperature dependence that we observed is not Arrhenian, as is normally observed in fluids. In fitting our viscosity data to an exponential function, we find a negative activation energy and a negative number of activation sites. The reason for this may be that we have forced the system into a regime where we are no longer causing the correlation of random atomic motions by the application of shear, but are forcing bonds to be broken that are not thermally activated. Thus by increasing temperature, instead of providing more free clusters through which shear may occur, we are weakening the barriers to shear. A complementary way of describing this behavior is that at the same fixed shear rate, one can sample different non-Newtonian regimes at different temperatures and the viscosity measured will not exhibit the expected activated jump behavior.

Initiation of Fracture

Brittle fracture is initiated after a material experiences significant strain, causing an instability or instabilities that eventually leads to rupture of the material. In most real

materials, the instability is located at the largest flaw, causing the material to fracture at strains and stresses significantly less than the ultimate strain or stress than the material can support. However, in our simulations where there are no surfaces present for the likely initiation of fracture, fracture does occur near the ultimate strength of the material. Thus, we see the behavior in our samples that occurs only near the flaw or at an advancing crack tip in real materials. We see, for example the structural changes that occur in a material under high strain, and the initiation of fracture in a sample relatively free of flaws.

Because of the small size of the system that we simulate, the stress-strain curves that we derive are much different than those derived for macroscopic samples. We can see almost every bond that breaks as the material is strained-to-fracture instead of a stress-strain curve that is the result of an average over 10^{20} bonds. An important result of our small sample size is readily apparent from a knowledge of the concept of Weibull statistics--the probability of finding the type of flaw that would lead to the failure of a real material is very small in such a small sample. Because of the absence of large flaws, we may strain the material to large strains before fracture occurs. In a real material with a flaw, only a small volume of material near the flaw undergoes significant strain before failure, while much of the bulk is relatively unstrained. Thus, brittle fracture appears to occur without much deformation in real bulk materials, although the volume of the material through which fracture progresses may actually undergo significant strain.

The initiation of fracture is strongly dependent on strain rate in samples without initiating flaws. This is observed in our fracture experiments performed at various strain rates. At low strain rates, fracture is initiated at the largest void, weakness, or discontinuity in the sample. At high strain rates, the proximity of the void, weakness, or discontinuity to the strain to be relieved becomes important. For example, although a chain may be only as strong as its weakest link, in this case *strong* meaning the largest stress that the chain can sustain, only a massless chain will always break at its weakest link. During dynamic loading, a massive chain will tend to break at the points that strain is applied because the links near the points of applied strain must support not only the elastic stress of the chain, they must transfer the strain to the rest of the chain by accelerating neighboring links. The force required to accelerate neighboring links adds to the elastic stress within the link, and may cause fracture before the weakest link experiences its breaking stress. By a similar mechanism, a long massive chain of almost uniform strength that is strained uniformly by some means will tend to break at relatively uniform intervals along its length to minimize the transfer of strain along its length. At increasing strain rates, the chain would break at decreasing intervals as the acceleration required for the transfer of strain is increased. A solid under uniaxial strain is just a three dimensional chain of atoms, so it behaves in a similar manner.

As we apply strain uniformly throughout our samples, we find that fracture becomes increasingly de-localized at increasing strain rates, consistent with the chain example above. We can strain at seemingly unrealistic strain rates in order to produce this behavior, but as we will see, this behavior plays an important role in the propagation

of cracks during a fracture event. The result is that within the regime of brittle fracture, we can vary the extent by which fracture affects the structure by varying the strain rate. We can strain at an unrealistically high strain rate where we smoothly transform the solid into a gas by simultaneously breaking every bond in the material while lowering its density, or we can strain at a low strain rate to allow the added strain to move through the sample to the weakest point, resulting in fracture occurring roughly along a single plane.

A weak point in the structure of a material may be a permanent structural defect or a transient "defect." A transient defect in the structure of a material may be as slight as a thermal vibration. A thermal vibration would not normally cause a material to fracture, but in the case of a perfect crystal that is completely symmetrical in all other respects, a thermal vibration may be sufficient to cause the break in symmetry needed to initiate fracture. In glasses, it may be assumed that structural defects predominate over transient defects. The effects of structural defects in glasses and transient defects in perfect crystals are similar, as was evidenced by fracture simulations of glasses and of cristobalite modeled by the F-G potential. Both of these types of fracture showed a strain rate dependence on the stress and strain at which fracture was initiated, which was the hallmark of a continuous distribution of weak points throughout the structure. In the case of cristobalite modeled by the Soules potential, the break in symmetry resulting from a transition in the structure dominated the initiation of fracture, and resulted in the fracture behavior of this material having little dependence on strain rate.

Crack Propagation

Since the sizes of our simulations were limited to tens of angstroms, we were unable to do direct studies of crack propagation. However, by simulating a range of strain rates and observing the material's response, and making some assumptions about the strain state in a material during crack propagation, we can predict the material's behavior during crack propagation.

Most interesting cases of crack propagation occur in cases where a material fails under constant force, that is, a load is applied to a sample and the sample breaks. However, as the sample fractures, the stress and strain distributions in front of the crack tip change. When a load is applied to a sample with an initiating flaw, it is usually applied relatively slowly so that the strain distribution in the sample stays close to equilibrium. Because the sample has an initiating flaw in it, a disproportionately large amount of strain will be distributed near that flaw. At some critical stress or strain, the material near the flaw becomes unstable and a crack starts to propagate. However, the crack grows into regions in which strain is not already disproportionately distributed. The strain distributed throughout the sample must now become redistributed to these regions. As the crack progresses rapidly into the material the strain must be redistributed rapidly to the crack tip. This causes the material at the crack tip to be subjected to a high local strain rate. In contrast to the concentrated distribution of strain at or near the initiating flaw, the strain distribution at the crack tip becomes more diffuse as the crack propagates. In this more diffuse strain environment, fracture becomes less localized as it follows weak points distributed throughout the volume of high strain, yet the crack

must still connect the fracture points. As a result, the path of the crack becomes more tortuous as the crack propagates. Additionally, the location of the crack tip at each instant and weak points in the structure influence the later distribution of strain so that the fracture path tends to remain contiguous and larger weak spots tend to influence fracture to progress through smaller weak spots in their vicinity. This provides the feedback mechanism by which self-similar surfaces may form. Finally, as fracture continues, the strain distribution becomes so diffuse that the crack can no longer remain contiguous and crack branching occurs.

Simulation of Stochastic Crack Growth

In order to illustrate the result of the proposed fracture process, we performed a crude simulation of this stochastic crack growth. We made an assumption that there was one initiating flaw in a square lattice, and that there was a variance in local strengths through the rest of the lattice. Each point in the square lattice was given a normally distributed random flaw "strength" that would tend to suppress the effect of other flaws in its vicinity. The effect of a flaw was the amount of deviation along the z-axis that the flaw could produce. Normally distributed random deviations were assigned to all points, and the weighted sum of these suppressed deviations were plotted.

Basically, the pseudo-surface routine works as follows. It is assumed that fracture occurs in a material having a variation of local cohesive strength as a result of "defects." The path of a crack will be influenced by the defects in a material. The more dominant the "defect", the more the location of the crack will be influenced by the defect, and the

less it will be influenced by other defects in the vicinity. The initiating flaw is the most dominant. Defects in the vicinity will have only a small effect, making the crack in this region appear to be smooth. As the crack advances away from the initiating defect, the initial defect becomes less dominant, and the smaller variations, which are normally distributed in dominance, drive the path of fracture. Crack deviations are given as the sum of two dimensional normal distributions centered at lattice points with uniform widths and heights given as the ratio of a gaussian deviate to the sum of two dimensional normal distributions centered at lattice points with uniform widths and heights given as a gaussian deviate representing the dominance of the defect at that point.

Working backwards in symbolic form, the z-coordinate of the surface at x, y is the sum of the deviations of all defects, $z_{xy} = \sum_j \sum_i d_{ij} \times \exp\left(-\frac{(x-i)^2 + (y-j)^2}{D^2}\right)$. The

deviation of the defect at x, y is proportional to a Gaussian deviate multiplied by the effect of the defect at x, y divided by the summed effect of all defect effects in the

vicinity, $d_{xy} = \frac{\text{gdev}(1) \times B \times a_{xy}}{\sum_j \sum_i a_{ij} \times \exp\left(-\frac{(x-i)^2 + (y-j)^2}{C^2}\right)}$. The effect of the defect at point x, y is

given by the absolute value of the Gaussian deviate, $a_{xy} = |\text{gdev}(1)|$. This may be modified over a locus of points to simulate a flaw (not shown).

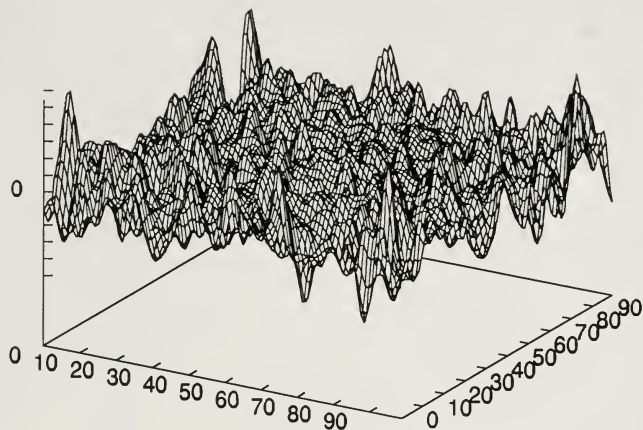


Figure 5-1. Pseudo fracture surface created by simple stochastic crack propagation simulation.

The result is a surface that crudely approximates a fracture surface, smooth near the initiating flaw, and growing increasingly rougher and coarser at points distant from the initiating flaw, as shown in Figure 5-1. It was not possible to see if this surface was self-similar, but it has become clear that simulations of stochastic crack growth may represent a way of modeling fracture that makes use of information obtained by atomistic dynamic simulations to extend beyond the spatial limits of those simulations. This simulation was quick and dirty, and its inefficiency limited the size of the surface that could be simulated, but with some work, one should be capable of developing better algorithms.

The Completion of Fracture

In real materials, brittle fracture appears to go to completion rapidly after it has been initiated. In our simulations, we do not see this behavior as significant strain must be added before the connectivity of the structure is completely broken across the fracture plane. This behavior is evidenced in the stress-strain curves we have obtained as well as in the graphical images of the structure during fracture that we create. This behavior is observed because we are simulating the small volume of material near the crack tip and not a bulk sample. The material at the crack tip in real materials does undergo significant strain during the fracture process before crack propagation can proceed, similar to the behavior that we observe.

Two size dependent aspects affect how fracture goes to completion in real material samples. The first is that strain energy is stored throughout the bulk of the material, but it is only consumed in the small volume of material that becomes transformed into a surface. The second is that a small overall strain applied to the bulk material during the fracture process translates to a large strain in the region of crack propagation. These result in the appearance that there is little added energy or strain in the fracture of real materials.

In our simulations, we observe that there is an energy balance in fracture. Energy is added through the application of strain against the stress developed in the material. As fracture progresses, this energy is converted into excess configurational energy at the fracture surface and heat. Because the surface structures that we obtain are dependent on the strain rate, with surfaces created at higher strain rates being rougher and

possessing more unsatisfied or strained bonds, the energy is required to form the surfaces is also dependent on strain rate. Thus we find a relationship between strain rate, surface roughness, and the energy required for fracture.

The energy required for fracture is related to the toughness of the material. While the strength of a material is generally related to the stress required to cause the initiation of fracture, the toughness is related to the energy required to drive fracture to completion once it is initiated. We observe that this energy is not just the energy required to form surfaces on which all bonds are not satisfied, but also energy required to cause structural rearrangements in the near surface region, as evidenced by the significant strain that occurs in this region, and energy that is lost to heat by the fracture process.

The Structure of the Fracture Surface

Fracture surfaces form by the collective breaking of bonds resulting in a disrupted structure. Thus, the surface is the product of broken bonds. To understand the structure of a fracture surface in silica, we first need to understand the process by which bonds are broken in this material.

When is a Bond Broken

Oppositely charged species in an ionically bonded system attain a close proximity to each other by Coulombic attraction. One could draw an imaginary plane through a material that cuts all bond entities but does not cut atoms. Such a plane would break

covalent bonds by de-pairing bonding electrons, but it would have no effect on ionic bonds. Similarly, one could displace material on one side of the plane normal to the plane and still have some ionic attraction between the two sides. If the material on both sides were static, one could separate the sides by a considerable distance and still have some long-range coulombic attraction between the faces. Hence although bond strengths would be greatly attenuated, bonds could still be considered to exist. A bond is not considered broken if there is a monotonically downhill path leading to a configuration of near minimum configurational energy.

Surface Reconstruction

How is fracture stabilized in such a system? If the individual bonds were not broken, then the material as a whole could not be considered broken because the surface would be unstable with respect to putting the pieces back together and re-forming a bulk. Let us create a definition of a stable surface similar to one of the broken bond. A surface is stable if there is no system configurational energy path that is monotonically downhill leading to the disintegration of the surface.

If surfaces were static, there would be a dangling silicon atom on one surface corresponding to every dangling oxygen atom on the other surface. However, simulations show that there is always a predominance of oxygen atoms on fracture surfaces so that silicon atoms do not extend into the void at a material surface. Apparently, the dangling atoms collapse back into the neighboring structure to attempt to satisfy their desired coordination. Since silicon atoms attempt to be more highly

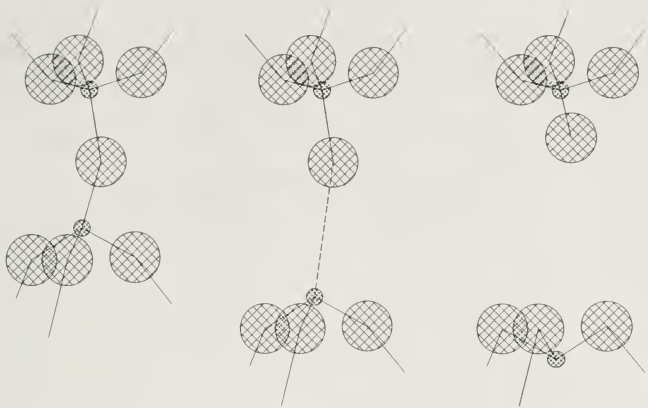


Figure 5-2. Schematic showing the fracture of a bond in vitreous silica. Series shows unstrained bond, strained bond, and broken bond.

coordinated as a result of their higher ionic charge, they are pulled back into the structure where they can be coordinated by oxygen atoms that pay a lesser penalty for being on the surface. A schematic of such a process is shown in figure 5-2.

When the pair of fracture surfaces become reconstructed, they no longer feel an attraction towards each other. When the faces are brought back together, the system experiences a repulsion that must be overcome in order to re-bond them. If the faces do

become re-bonded, they may not be bonded in the same way. It is this reorientation process occurring on the surfaces that makes fracture complete and stable.

Another potentially important aspect in the formation of fracture surfaces is the effect of the non-linear elastic modulus. Proctor²⁷ postulated that the mechanisms of fracture may be influenced by the positive non-linear elastic modulus of silica. Kulawansa et al.²⁸ found differences between the fracture surface structure of alkali silicate and silica glasses in an AFM study. The silica glass structures had more rounded features whereas the soda-lime glass exhibited more angular features. They reasoned that the crack would propagate in such a way as to diffuse strain because incremental additions of strain to already strained regions would result in a higher energy than the addition of strain to unstrained regions. This competes with the desire for materials to condense strain in one location to cause fracture and minimize the overall strain energy. However, this is not unique to a non-linear elastic modulus. For any positive elastic modulus defined as $E = \frac{d\sigma}{d\epsilon}$, strain will always tend to be spread uniformly throughout the structure. Although silica has a positive non-linear elastic modulus through part of its elastic extension, failure will always commence when the addition of strain to the material drives the material or at least some local part of it into a regime of negative elastic modulus. When this occurs, the uniform distribution of strain becomes unstable, causing strain to collect at the advancing crack tip. Thus, wherever fracture is occurring, the positive non-linear elastic modulus of silica is no longer in effect, and should not play a major role in shaping the fracture surface.

Determinism in Fracture

Computer simulations offer the best means of studying mechanically induced chaos due to the strict deterministic nature of computer calculations. This approach allows total control over all boundary and initial conditions as is shown in the strict reproducibility of results from identical runs.

Except for variations in fluctuations of system properties, the effects of the bounded chaotic motion of the constituent atoms of a non-crystalline solid were barely observable in the behavior of ensemble averages when the system was undergoing annealing or strain in the elastic region. In a true macroscopic system, even the statistical fluctuations in system properties observed in our simulations would be invisible by virtue of the much larger system size. In such a case, the stress-strain behavior of the non-crystalline solid would appear to be fully predictable, independent of initial conditions, round off errors, or anneal times, once equilibrium was established.

However, the inelastic and failure responses of the solid exhibited all characteristics of chaotic behavior. They showed sensitivity to anneal times, initial structure, round-off error and a small displacement of a single atom. This result is not totally surprising. The fracture process is expected to be chaotic because of its sensitivity to individual bond structures, and because it is the response to a set of coupled non-linear interactions.

Fracture has never been completely predictable and has always required statistical analysis, however, this has been assumed to result from the statistical nature of the size and shape of surface cracks and flaws in the material. Griffith's successful concepts of

brittle fracture were tied to crack size and stress amplification. Our results suggest that there is another source of unpredictability in the fracture process, arising from the chaotic growth of voids in an ideal material with no surface flaws and under a totally uniform strain. It is clear that this process controls crack propagation since the crack surface is never geometrically smooth and exhibits a fractal dimension.

CHAPTER 6 CONCLUSIONS AND FUTURE WORK

The use of molecular dynamics in the study of the brittle fracture of silica has given us the ability to view the fracture process from different perspectives. We have related the standard stress-strain curves to the structural and thermodynamic changes that occur during strain-to-fracture. MD offers us an encompassing view of fracture that allows us to better understand long-observed fracture behaviors. We find that our general results are insensitive to details of the simulation model used.

We find that an appreciation of the dynamics aspects of fracture is crucial to understanding the mechanical response of a material during fracture and to predicting the mechanism by which a crack will propagate through a brittle material. The elastic response of silica and the strain distribution throughout a material during fracture is time dependent. It is the dynamics involved in the distribution of strain during fracture that causes the well known surface features as mirror, mist, hackle, and crack-branching.

The fracture surface of silica is stabilized by the reorientation of oxygen and silicon atoms at the fracture surface. Oxygen atoms move to the surface and provide a repulsive barrier between opposing fracture surfaces.

We find that brittle fracture is extremely sensitive to initial conditions, including the vibrational phase of the material with respect to the application of strain. This makes

it impossible to predict the exact path of fracture for any real material that fractures during a rapid brittle fracture process.

We have identified a crack-growth mechanism that may result in the formation of self-similar fracture surfaces of the type observed in real fracture experiments. Further work with stochastic crack propagation simulations may further elucidate the link between materials properties, fracture mechanisms, and fracture surface structures.

REFERENCE LIST

1. A.A. Griffith, "The phenomena of rupture and flow in solids," *Philos. Trans. R. Soc.* A221 163-198 (1921).
2. E. Orowan, "Fracture and strength of solids," *Repts. Prog. Phys.* 12 185-232 (1948).
3. T.A. Michalske, S.W. Freiman, "A molecular mechanism for stress corrosion in vitreous silica," *J. Am. Ceram. Soc.* 66 284 (1983).
4. A. Rahman, "Correlations in motion of atoms in liquid Ar," *Phys. Rev. A* 136 A410 (1964).
5. J.T. Dickinson, S.C. Langford, L.C. Jensen, G.L. McVay, J.F. Kelso, C.G. Pantano, "Fractoemission from fused silica and sodium silicate glasses," *J. Vac. Sci. Technol. A* 6 [3] 1084-1089 (1988).
6. J.J. Gilman, "The Strength of Ceramic Crystals," in *The Physics and Chemistry of Ceramics*, Ed. C. Klingsberg, Gordon and Branch, New York, 270 (1963).
7. S.M. Wiederhorn, "Fracture of Ceramics," in *Mechanical and Thermal Properties of Ceramics*, National Bureau of Standards Special Publication 303, 217 (1969).
8. B.A. Proctor, I. Whitney, J.W. Johnson, "The strength of fused silica," *Proc. R. Soc. London Ser. A* 297 534-557 (1967).
9. D.G. Holloway, *The Physical Properties of Glass*, Wykeham Publications Ltd., London, 170 (1973).
10. S.M. Wiederhorn, "Influence of water vapor on crack propagation in soda-lime glass," *Journal of the American Ceramic Society*, 50 [8] 407-414 (1967).
11. T.A. Michalske, "Fractography of slow fracture in glass," in *Fractography of Ceramic and Metal Failures* ASTM STP 827, Eds. J.J. Mecholsky, Jr. and S.R. Powell, Jr., American Society for Testing and Materials, Philadelphia, 121-136 (1984).
12. J.E. Gordon, D.M. Marsh, M.E.M.L. Parratt, "On the strength and structure of glass," *Proc. R. Soc. London Ser. A* 249 59-72 (1959).

13. J.J. Mecholsky, S.W. Freiman, R.W. Rice, "Fractographic Analysis of Ceramics," in ASTM STP 645, American Society for Testing and Materials, Philadelphia, 363-379 (1978).
14. D.G. Holloway, The Physical Properties of Glass, Wykeham Publications Ltd., London, 12 (1973).
15. W.D. Kingery, H.K. Bowen, D.R. Uhlmann, Introduction to Ceramics, Second Edition, John Wiley & Sons, New York, 87 (1976).
16. CRC Handbook of Chemistry and Physics, 61st Edition, Eds. Robert C. Weast, Melvin J. Astle, CRC Press Inc., Boca Raton, B-143 (1980).
17. T.D. Coyle, "Silica" in Kirk-Othmer Encyclopedia of Chemical Technology, Third Ed., John Wiley & Sons, New York, Vol. 20, 748-766 (1982).
18. R.W.G Wyckoff, Crystal Structures, Second Edition, Wiley, New York, Vol. 1, Chapter IV, 27-28 (1963).
19. F.L. Galeener, "Planar rings in vitreous silica," J. Non Cryst. Sol. 49 53-62 (1982).
20. Carol S. Mariani, Linn W. Hobbs, "The phase structure of aperiodic SiO₂ as a function of network topology," Journal of Non-Crystalline Solids 106 309-312 (1988).
21. Carol S. Mariani, Linn W. Hobbs, "Characterization of SiO₂ surfaces as a function of network connectivity," Journal of Non-Crystalline Solids 106 317-320 (1988).
22. Carol S. Mariani, Jeremy K. Burdett, "Geometric constraints: a refined model for the structure of silica glass," Journal of Non-Crystalline Solids 124 1-21 (1990).
23. C.J. Brinker, B.C. Bunker, D.R. Tallant, K.J. Ward, "Chemical reactivity and the structure of gels," Journal de Chemie Physique 83 [11/12] 851-858 (1986).
24. P.N. Sen, M.F. Thorpe, "Phonons in AX₂ glasses: From molecular to band-like modes," Phys. Rev. B15 4030 (1977).
25. F.P. Mallinder, B.A. Proctor, "Elastic constants of fused silica as a function of large tensile strain," Physics and Chemistry of Glasses 5 [4] 91-103 (1964).
26. W.B. Thomas and S.D. Brown, "Nonlinear elasticity of fused silica at room temperature," Physics and Chemistry of Glasses 13 [3] 94 (1972).

27. B.A. Proctor, "Strength, nonlinear stress-strain behaviour, and structural flaws in glass," *Physics and Chemistry of Glasses* 31 [2] 78-80 (1990).
28. D.M. Kulawansa, L.C. Jensen, S.C. Langford, J.T. Dickinson, Yoshihisa Watanabe, "Scanning tunneling microscope observations of the mirror region of silicate glass fracture surfaces," *Journal of Materials Research* 9 [2] 476-485 (1994).
29. C.R. Kurkjian, U.C. Paek, "Single-valued strength of 'perfect' silica fibers," *Appl. Phys. Lett.* 42 [3] 251-253 (1983).
30. T.A. Michalske, B.C. Bunker, "Slow fracture model based on strained silicate structures," *J. Appl. Phys.* 56 [10] 2686-2693 (1984).
31. J.K. West, L.L. Hench, "Silica fracture, Part I: A ring contraction model," submitted to the *Journal of Materials Science* (1994).
32. J.K. West, L.L. Hench, "Silica fracture, part II: A ring opening model via hydrolysis," submitted to the *Journal of Materials Science* (1994).
33. William G. Hoover, "Computer simulation of many-body dynamics," *Physics Today* 37 [1] 44-50 (1984).
34. D.M. Heyes, Michael Barber, Julian H.R. Clarke, "Molecular dynamics computer simulation of thin films of LiCl, NaCl, KCl, and RbCl Possessing (100) crystal-vacuum surfaces," *J. Chem. Soc., Faraday Trans. 2* 75 1469 (1979).
35. D.M. Heyes, M. Barber, J.H.R. Clarke, "Molecular dynamics computer simulation of surface properties of crystalline potassium chloride," *J. Chem. Soc., Faraday Trans. 2* 73 1485-1496 (1977).
36. D.M. Heyes, "Molecular dynamics simulations of ionic crystal films," *Journal of Chemical Physics* 79 4010 (1983).
37. Jeremy Q. Broughton, George H. Gilmer, "Molecular dynamics investigation of the crystal-fluid interface. I. Bulk properties," *Journal of Chemical Physics* 79 5095 (1983).
38. Jeremy Q. Broughton, George H. Gilmer, "Molecular dynamics investigation of the crystal-fluid interface. II. Structure of the fcc (111), (100), and (110) crystal-vapor systems," *Journal of Chemical Physics* 79 5105 (1983).
39. Jeremy Q. Broughton, George H. Gilmer, "Molecular dynamics investigation of the crystal-fluid interface. III. Dynamical properties of fcc crystal-vapor systems," *Journal of Chemical Physics* 79 5119 (1983).

40. G.H. Gilmer, M.H. Grabow, A.F. Bakker, "Modeling of epitaxial growth," *Materials Science and Engineering* **B6** 101-112 (1990).
41. Axel T. Brünger, John Kuriyan, Martin Karplus, "Crystallographic *R* factor refinement by molecular dynamics," *Science* **235** 458-460 (1987).
42. Uzi Landman, W.D. Luedtke, "Interfacial junctions and cavitation," *Materials Research Society Bulletin* **XVII** [5] 36-44 (1993).
43. Judith A. Harrison, Carter T. White, Richard J. Colton, Donald W. Brenner, "Atomistic simulations of friction at sliding diamond interfaces," *Materials Research Society Bulletin* **XVIII** [5] 50-53 (1993).
44. James Belak, David B. Boercker, Irving F. Stowers, "Simulation of nanometer-scale deformation of metallic and ceramic surfaces," *Materials Research Society Bulletin* **XVII** [5] 55-60 (1993).
45. A.F. Bakker, G.H. Gilmer, M.H. Grabow, K. Thompson, "A special purpose computer for molecular dynamics calculations," *Journal of Computational Physics* **90** 313-335 (1990).
46. Neil W. Ashcroft, N. David Mermin, *Solid State Physics*, Saunders College, Philadelphia, 398 (1976).
47. Murray S. Daw, M.I. Baskes, "Semiempirical, quantum mechanical calculation of hydrogen embrittlement in metals," *Physical Review Letters* **50** [17] 1285-1287 (1983).
48. Alan F. Wright, Murray S. Daw, C.Y. Fong, "Structures and energetics of Pt, Pd, and Ni adatom clusters on the Pt(001) surface: Embedded-atom-method calculations," *Physical Review B* **42** [15] 9409-9419 (1990).
49. Frank H. Stillinger, Thomas A. Weber, "Computer simulation of local order in condensed phases of silicon," *Physical Review B* **31** 5262 (1985).
50. William R. Busing, "Interpretation of the crystal structure of Li_2BeF_4 in terms of the Born-Mayer-Huggins model," *J. Chem. Phys.*, **57** 3008-3010 (1972).
51. L.V. Woodcock, C.A. Angell, P. Cheeseman, "Molecular dynamics studies of the vitreous state: Simple ionic systems and silica," *The Journal of Chemical Physics* **65** [4] 1565-1577 (1976).
52. P. Vashishta, Rajiv K. Kalia, José P. Rino, Ingvar Ebbsjö, "Interaction potential for SiO_2 : A molecular-dynamics study of structural correlations," *Physical Review B* **41** [17] 12197-12209 (1990).

53. B. Vessal, M. Amini, D. Fincham, C.R.A. Catlow, "Water-like melting behaviour of SiO₂ investigated by the molecular dynamics simulation technique," *Philosophical Magazine B* 60 [6] 753-775 (1989).
54. Adrian C. Wright, "The comparison of molecular dynamics simulations with diffraction experiments," *Journal of Non-Crystalline Solids* 159 264-268 (1993).
55. P. Ewald, "Die berechnung optischer und elektrostastischer gitterpotentiale," *Annln. Phys.* 64 253 (1921).
56. Ali Alavi, Luis J. Alvarez, Stephen R. Elliott, Ian R. McDonald, "Charge-transfer molecular dynamics," *Philosophical Magazine B* 65 [3] 489-500 (1992).
57. Y.L. Tsai, T.P. Swiler, J.H. Simmons, J.J. Mecholsky, Jr., "Fractal fracture of single crystal silicon using molecular dynamics," Submitted to the *Journal of Applied Physics* (1994).
58. S.K. Mitra, M. Amini, D. Fincham, R.W. Hockney, "Molecular dynamics simulation of silicon dioxide glass," *Philosophical Magazine B* 43 365-372 (1981).
59. T.F. Soules, "A molecular dynamic calculation of the structure of sodium silicate glasses," *J. Chem. Phys.* 71 [11] 4570-4578 (1979).
60. Thomas F. Soules, Robert F. Busbey, "Sodium diffusion in alkali silicate glass by molecular dynamics," *J. Chem. Phys.* 75 [2] 969-975 (1981).
61. S.H. Garofalini, S.M. Levine, "Differences in surface behavior of alkali ions in Li₂O·3SiO₂ and Na₂O·3SiO₂ glasses," *Journal of the American Ceramic Society* 68 376 (1985).
62. B.P. Feuston, S.H. Garofalini, "Topological bonding defects in vitreous silica surfaces," *Journal of Chemical Physics* 91 564 (1989).
63. S.H. Garofalini, "Molecular dynamics computer simulations of silica surface structure and adsorption of water molecules," *Journal of Non-Crystalline Solids* 120 1-12 (1990).
64. Adrian C. Wright, "How much do we really *know* about the structure of amorphous solids," *Journal of Non-Crystalline Solids* 75 15-28 (1985).
65. B. Vessal, M. Amini, C.R.A. Catlow, "Computer simulation of the structure of silica glass," *Journal of Non-Crystalline Solids* 159 184-186 (1993).
66. A. Paskin, A. Gohar, G.J. Dienes, "Computer simulation of crack propagation," *Phys. Rev. Lett.* 44 940 (1980).

67. A. Paskin, B. Massoumzadeh, K. Shukla, K. Sieradzki, G.J. Dienes, "Effect of atomic crack tip geometry on local stresses," *Acta Metall.* 33 [11] 1987-1996 (1985).
68. G.J. Dienes, A. Paskin, "Molecular dynamic simulations of crack propagation," *J. Phys. Chem. Solids* 48 1015-1033 (1987).
69. K. Sieradzke, G.J. Dienes, A. Paskin, B. Massoumzadeh, "Atomistics of crack propagation," *Acta Metall.* 36 [3] 651-663 (1988).
70. T.F. Soules, R.F. Busbey, "The rheological properties and fracture of a molecular dynamic simulation of sodium silicate glass," *J. Chem. Phys.* 78 [10] 6307-6316 (1983).
71. Thomas F. Soules, "Models of glass strength and relaxation phenomena suggested by molecular dynamic simulations," *Journal of Non-Crystalline Solids* 73 315-330 (1985).
72. John Kieffer, C. Austen Angell, "Generation of fractal structures by negative pressure rupturing of SiO₂ glass," *Journal of Non-Crystalline Solids* 106 336-342 (1988).
73. Romulo Ochoa, Joseph H. Simmons, "High strain rate effects on the structure of a simulated silica glass," *Journal of Non-Crystalline Solids* 75 413-418 (1985).
74. Romulo Ochoa, Thomas P. Swiler, Joseph H. Simmons, "Molecular dynamics studies of brittle fracture in silica: effect of thermal vibrations," *Journal of Non-Crystalline Solids* 128 57-68 (1991).
75. Joseph H. Simmons, Thomas P. Swiler, Romulo Ochoa, "Molecular dynamics studies of brittle fracture in silica: Bond fracture," *Journal of Non-Crystalline Solids* 134 179-182 (1991).
76. E. Lorenz, "Deterministic nonperiodic flow," *Journal of the Atmospheric Sciences* 20 130-141 (1963).
77. James Gleick, Chaos: Making A New Science, Penguin Books, New York, 11-31 (1987).
78. S.C. Langford, Ma Zhenyi, J.T. Dickinson, "Photon emission as a probe of chaotic processes accompanying fracture," *J. Mater. Res.*, 4 [5] 1272-1279 (1989).
79. Kenneth Falconer, Fractal Geometry John Wiley and Sons, West Sussex, England, 38 (1990).

80. J.J. Mecholsky, D.E. Passoja, K.S. Feinberg-Ringel, "Quantitative analysis of brittle fracture surfaces using fractal geometry," *J. Am. Ceram. Soc.* 72 [1] 60-65 (1989).
81. Y.L. Tsai, J.J. Mecholsky, Jr., "Fractal fracture of single crystal silicon," *J. Mater. Res.* 6 [6] 1248-1263 (1991).
82. J.J. Mecholsky, T.J. Mackin, and D.E. Passoja, "Self similar crack propagation in brittle materials," in Advances in Ceramics 22: Fractography of Glasses and Ceramics, The American Ceramic Society, Columbus, Ohio, 127-134 (1988).
83. T.F. Soules, "Computer-simulation of glass structures," *J. Non-Cryst. Solids* 123 48-70 (1990).
84. B.P. Feuston and S.H. Garofalini, "Empirical three body potential for vitreous silica," *J. Chem. Phys.* 89 [9] 5818-5824 (1988).
85. Loup Verlet, "Computer 'experiments' on classical fluids. I. Thermodynamical properties of Lennard-Jones molecules," *Phys. Rev.* 159 98-103 (1967).
86. J.M. Haile, Molecular Dynamics Simulation: Elementary Methods, Wiley, New York, (1992).
87. Romulo Ochoa, "Molecular dynamics study of crack behavior in an amorphous material," Ph.D. Dissertation, Catholic University of America, Washington, D.C. (1985).
88. Thomas F. Soules, "Molecular dynamic calculations of glass structure and diffusion in glass," *J. Non. Cryst. Sol.* 49 29 (1982).
89. K. Goetzke, H.-J. Klein, "Properties and efficient algorithmic determination of different classes of rings in finite and infinite polyhedral networks," *J. Non-Cryst. Solids* 127 (1991) 215-230.
90. William H. Press, Saul A. Teukolsky, William T. Vetterling, Brian P. Flannery, Numerical Recipes in C, Second Edition, Cambridge University Press, New York, 15 (1992).
91. Greg O'Rear, "Molecular dynamics simulation of glass structure," M.S. Thesis, University of Florida, (1988).
92. R.L. Mozzi, B.E. Warren, "The structure of vitreous silica" *J. Appl. Cryst.* 2 164-172 (1969).
93. R.F. Pettifer, R. Dupree, I. Farnam, and U. Sternberg, "NMR determinations of Si-O-Si bond angle distributions in silica," *J. Non-Cryst. Sol* 106 408-412 (1988).

94. F.L. Galeener, A.C. Wright, "The J.C. Phillips model for vitreous SiO₂: A critical appraisal," *Solid St. Comm.* 57 677 (1986).
95. J.H. Simmons, T.P. Swiler, C.J. Simmons, "Studies of Non-Linear Viscous Flow in Silicate Glasses," in Ceramic Transactions: Advances in Fusion and Processing of Glass, Eds. A.K. Varshneya, Dennis F. Bickford, Peter P. Bihuniak, The American Ceramic Society, Westerville, Ohio, (1993).

BIOGRAPHICAL SKETCH

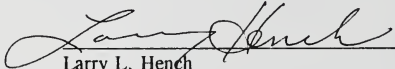
Thomas Paine Swiler was born on July 9, 1963, in Ridgewood, New Jersey. He attended third through twelfth grades at Jasper Central School in Jasper, New York, graduating as class valedictorian in 1981. He attended Alfred University in Alfred, New York, from 1981 to 1986 and participated in a cooperative education program with the Carborundum Company in Niagara Falls, New York, in 1983 and 1984. He received a B.S. in ceramic science and a B.A. in physics from Alfred University in 1986. He was briefly employed at Sandia National Laboratories in Albuquerque, New Mexico, during the summer of 1986 before entering the graduate program in Materials Science and Engineering at the University of Florida in Gainesville, Florida. He has been studying glass science under the advisement of Dr. Joseph H. Simmons at the University of Florida since that time. He received his M.S. in materials science and engineering in 1988 with a thesis on earlier studies of brittle fracture of silica by molecular dynamics. Since that time he has been involved in various activities ranging from being president of the University of Florida Student Branch of the American Ceramic Society in 1988-1989 to finishing in the top 500 at the Boston Marathon in 1992. Upon the completion of his doctoral studies, he hopes to find a job that will utilize his expertise in materials science and computer programming.

I certify that I have read this study and that in my opinion it conforms to acceptable standards of scholarly presentation and is fully adequate, in scope and quality, as a dissertation for the degree of Doctor of Philosophy.



Joseph H. Simmons, Chairman
Professor of Materials Science and
Engineering

I certify that I have read this study and that in my opinion it conforms to acceptable standards of scholarly presentation and is fully adequate, in scope and quality, as a dissertation for the degree of Doctor of Philosophy.



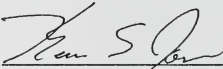
Larry L. Hench
Graduate Research Professor of Materials
Science and Engineering

I certify that I have read this study and that in my opinion it conforms to acceptable standards of scholarly presentation and is fully adequate, in scope and quality, as a dissertation for the degree of Doctor of Philosophy.



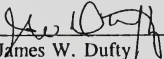
Paul H. Holloway
Professor of Materials Science and
Engineering

I certify that I have read this study and that in my opinion it conforms to acceptable standards of scholarly presentation and is fully adequate, in scope and quality, as a dissertation for the degree of Doctor of Philosophy.



Kevin S. Jones
Associate Professor of Materials Science
and Engineering

I certify that I have read this study and that in my opinion it conforms to acceptable standards of scholarly presentation and is fully adequate, in scope and quality, as a dissertation for the degree of Doctor of Philosophy.


James W. Dufty
Professor of Physics

This dissertation was submitted to the Graduate Faculty of the College of Engineering and to the Graduate School and was accepted as partial fulfillment of the requirements for the degree of Doctor of Philosophy.

April 1994


fn Winfred M. Phillips
Dean, College of Engineering

Karen A. Holbrook
Dean, Graduate School
